Shear Flow Instabilities in Viscoelastic Fluids

Helen Jane Wilson

Clare College

September 2, 1998

A dissertation submitted to the University of Cambridge

for the degree of Doctor of Philosophy

Preface

The work described in this dissertation was carried out between October 1995 and September 1998, while the author was a research student in the Department of Applied Mathematics and Theoretical Physics, University of Cambridge. The dissertation is the result of my own work and includes nothing which is the outcome of work in collaboration. Except where explicit reference is made to the work of others, the contents of this dissertation are believed to be original. No part of this dissertation has been or is being submitted for a degree, diploma or other qualification at any other University.

It is a pleasure to record my thanks to my supervisor, Dr. John Rallison, for all his help. No-one could wish for a better supervisor. I would also like to thank Professor John Hinch for useful discussions, and Jeremy Bradley for proofreading.

This work was funded by a research studentship from the Engineering and Physical Sciences Research Council.

To my parents

Contents

Chapter 1

Introduction

1.1 Outline

Viscoelastic liquids (for example, polymeric melts and solutions) have flow properties that are in part viscous and in part elastic. The presence of elastic stresses can generate instabilities, even in inertialess flow, that do not arise in Newtonian liquids. These are often described as 'purely elastic' instabilities. The principal aim of this dissertation is to examine the class of such instabilities that arise in shear flows, and the mechanism responsible for them.

We start with a review of the principal non-Newtonian features of fluids of interest (section 1.2), then consider how these may be captured in a constitutive model (section 1.3). We then turn to a review of the experimental literature on purely elastic instabilities (section 1.4) and the current theoretical understanding of these phenomena (section 1.5). An outline of the new instabilities discussed in this thesis is given in section 1.6.

Fuller descriptions of non-Newtonian phenomena are given by Bird *et al* [17, 18], and of constitutive models by Larson [112] and Bird & Wiest [19]. We select here the items of greatest concern for the understanding of shear instabilities.

1.2 Shear rheology of non-Newtonian fluids

In steady simple shear, having a velocity vector $\boldsymbol{u} = (\dot{\gamma}y, 0, 0)$, it may be shown that any incompressible simple fluid will have a stress tensor $\boldsymbol{\sigma}$ with, in general, four nonzero components:

$$\begin{pmatrix} \sigma_{22}+N_1 & \sigma_{12} & 0 \\ \sigma_{12} & \sigma_{22} & 0 \\ 0 & 0 & \sigma_{22}-N_2 \end{pmatrix}. \tag{1.1}$$

As a result of the incompressibility, the stress is undetermined to within addition of an isotropic pressure term. For a Newtonian fluid, $N_1 = N_2 = 0$ and $\sigma_{12}/\dot{\gamma} = \mu$. In a viscoelastic fluid, however, these three quantities may vary with $\dot{\gamma}$. In considering the different categories of experimentally relevant fluid below, we define $\eta = \sigma_{12}/\dot{\gamma}$, $\Psi_1 = N_1/\dot{\gamma}^2$ and $\Psi_2 = N_2/\dot{\gamma}^2$.

We note, in passing, that because of the nonzero N_2, the stress tensor for a planar flow is not entirely two-dimensional. This may affect the stability of the flow to perturbations in the third dimension. For Newtonian fluids, Squire's theorem states that the most unstable disturbance is always two-dimensional, and hence stability calculations may be restricted to the two-dimensional domain. For a general non-Newtonian fluid, this may not be true.

1.2.1 Dilute polymer solution, Boger fluid

For a dilute polymer solution, the first normal stress difference N_1 is found to be positive, and may be large compared with σ_{12}. Both η and Ψ_1 show very little shear-thinning at moderate shear-rates (*i.e.* they are more or less constant). However, at higher shear-rates there is some thinning (often with $\Psi_1 \sim \dot{\gamma}^{-1}$). The second normal stress difference, N_2, is almost zero [131]. Figure 1.1 sketches the shear behaviour of typical dilute polymeric fluids.

A basic way to start characterising viscoelastic fluids is by their zero-shear-rate shear viscosity, η_0, and their (longest) relaxation time, which we

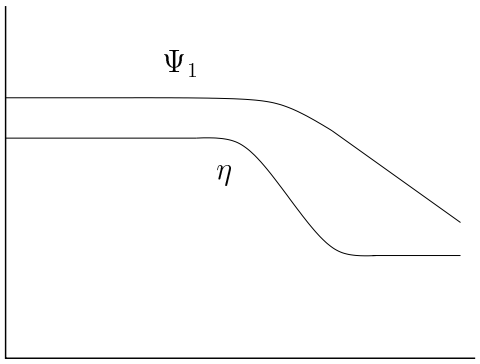

Figure 1.1: Generic behaviour of both the viscometric functions η and Ψ_1 against shear-rate for dilute solutions. Both axes use a logarithmic scale. There is a low-shear-rate plateau followed by a region of weak shear-thinning. For a Boger fluid, the plateau would extend across a very large range of shear-rates.

shall call λ. This time can be made large by using high molecular weight polymers or a very viscous solvent. Dilute solutions in which both of these methods are used to create a very long relaxation time are called Boger fluids [21]. They use as solvent a very low molecular weight melt of the same polymer as the solute. These fluids have a very long plateau of constant η and Ψ_1.

Even here the picture is complicated: using a Boger fluid made of two polystyrenes, MacDonald and Muller [128] have found a long-time relaxation of the normal stresses, which seems to be an inherent property of the fluid (rather than an effect of degradation, instability, etc.). They conclude that the definition of a single timescale is uncertain. Indeed, dynamic linear viscoelastic data indicate that these fluids actually possess a spectrum of relaxation times (for example, Ferry [64]).

1.2.2 Entangled polymer melt

As for a dilute solution, N_1 is large enough to play an important rôle in the dynamics of these fluids. However, both the viscosity, η, and the first normal stress coefficient, Ψ_1, can decrease by several orders of magnitude as $\dot{\gamma}$ is increased (Laun [116]). Figure 1.2 shows schematically the behaviour of both these quantities.

The second normal stress coefficient, Ψ_2, is often significant and negative, as shown by several papers, for example Keentok *et al* [99].

Experimentally, for monodisperse entangled polystyrene solutions, Magda & Baek [129] have shown that shear-thinning also affects the second normal stress coefficient.

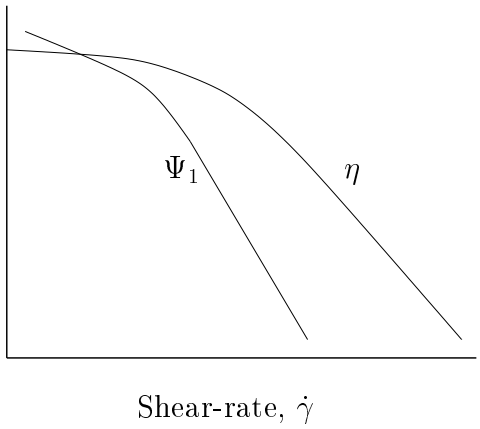

Figure 1.2: Sketch of the generic behaviour of both the viscometric functions, η and Ψ_1, against shear-rate, $\dot{\gamma}$, for entangled polymeric melts. Both axes use a logarithmic scale. Both quantities shear-thin strongly, but η still exhibits a low-shear-rate plateau, as it does for a dilute solution.

1.3 Constitutive equations: some theoretical models

1.3.1 Governing equations

For an incompressible fluid with velocity $\boldsymbol{u}$, any flow must satisfy the mass conservation equation:

$$\boldsymbol{\nabla}.\boldsymbol{u} = 0 \tag{1.2}$$

and any continuum obeys the momentum equation:

$$\rho\frac{D\boldsymbol{u}}{Dt} = \boldsymbol{\nabla}.\boldsymbol{\sigma} + \mathcal{F} \tag{1.3}$$

where $\boldsymbol{\sigma}$ is the stress tensor, ρ is the density and $\mathcal{F}$ represents any body forces acting on the fluid. $D/Dt \equiv \partial/\partial t + \boldsymbol{u}.\boldsymbol{\nabla}$ is the material derivative.

The inertial term on the left hand side of this equation is often small for viscoelastic flows, because of the high viscosities involved. In that case:

$$\boldsymbol{\nabla}.\boldsymbol{\sigma} = -\mathcal{F}. \tag{1.4}$$

The stress then needs to be defined in terms of the flow history by means of a constitutive equation.

1.3.2 Newtonian fluid

For a Newtonian fluid:

$$\boldsymbol{\sigma} = -p\boldsymbol{I} + 2\eta_s\boldsymbol{E} \tag{1.5}$$

where p is the pressure, η_s the viscosity of the fluid, $\boldsymbol{I}$ the identity matrix, and $\boldsymbol{E}$ is the symmetric part of the velocity gradient[1]:

$$\boldsymbol{E} = \frac{1}{2}\{\boldsymbol{\nabla u} + (\boldsymbol{\nabla u})^\top\}. \tag{1.6}$$

Its derivation is based on the assumptions that the fluid is isotropic, and that it responds instantaneously and linearly to the velocity gradient applied to it.

Equation (1.4) becomes the Stokes equation:

$$-\boldsymbol{\nabla} p + \eta_s \nabla^2 \boldsymbol{u} = -\mathcal{F}. \tag{1.7}$$

Since p only appears in the form $\boldsymbol{\nabla} p$, it is determined, for prescribed velocity (rather than stress) on the boundaries, only up to addition of an arbitrary constant.

For a polymer solution in a Newtonian solvent, the obvious extension is to set:

$$\boldsymbol{\sigma} = -p\boldsymbol{I} + 2\eta_s \boldsymbol{E} + \boldsymbol{\sigma}^p \tag{1.8}$$

where $\boldsymbol{\sigma}^p$ is the elastic or polymeric contribution to the stress tensor.

1.3.3 Oldroyd-B model

The Oldroyd-B model [149] may be derived by considering a suspension of Hookean dumbbells (see figure 1.3); that is, dumbbells in which the spring force $\boldsymbol{F}$ is directly proportional to the extension of the spring:

$$\boldsymbol{F} = G\boldsymbol{R}. \tag{1.9}$$

[1] We shall use the convention $(\boldsymbol{\nabla u})_{ij} = \boldsymbol{\nabla}_i \boldsymbol{u}_j$. There is no consistent convention in the literature for the ordering of the subscripts i and j.

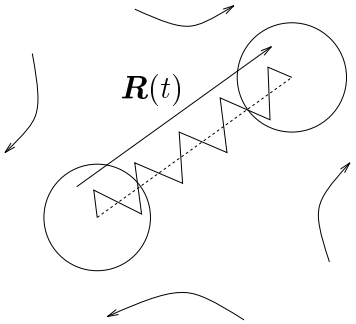

Figure 1.3: A dumbbell

The beads, which define the dumbbell ends, move under the action of: a Stokes drag from the solvent, Brownian motion and the spring force. Because of the stochastic nature of Brownian motion, the macroscopic properties of the fluid are derived from ensemble averages (denoted by <...>). The polymeric stress is given by:

$$\boldsymbol{\sigma}^p = <\boldsymbol{RF}> = G<\boldsymbol{RR}> \equiv G\boldsymbol{A}. \tag{1.10}$$

Its evolution may be expressed as:

$$\boldsymbol{A} + \lambda \overset{\nabla}{\boldsymbol{A}} = \boldsymbol{I} \tag{1.11}$$

with $\boldsymbol{I}$ being the unit tensor, and λ a relaxation time defined as $\lambda = \zeta/G$, where ζ is the drag coefficient ($6\pi\eta_s a$) acting on an isolated bead. The cases $\lambda = 0$ ($\boldsymbol{A} = \boldsymbol{I}$) and $G = 0$ ($\boldsymbol{\sigma}^p = 0$) correspond to a Newtonian fluid, and the case $\eta_s = 0$ ($\lambda \neq 0$) is the Upper-Convected Maxwell model (section 1.3.4).

The time derivative in equation (1.11) is the upper-convected derivative,

defined as:

$$\overset{\nabla}{\boldsymbol{A}} \equiv \frac{\partial}{\partial t}\boldsymbol{A} + \boldsymbol{u}.\boldsymbol{\nabla}\boldsymbol{A} - (\boldsymbol{\nabla}\boldsymbol{u})^{\top}.\boldsymbol{A} - \boldsymbol{A}.\boldsymbol{\nabla}\boldsymbol{u}.^{2} \tag{1.12}$$

This derivative is co-deformational with the line elements $\boldsymbol{dl}$ in the flow, so that:

$$(\overset{\nabla}{\boldsymbol{dl}}\,\boldsymbol{dl}) = \boldsymbol{0}. \tag{1.13}$$

It is the failure of the molecules to deform with fluid elements that generates elastic stress in the fluid.

The Oldroyd-B model is, in shear flows, a quantitatively good model for Boger fluids; nevertheless, its simplicity means that in general it cannot capture the full nature of a polymeric fluid. For example, it has only one relaxation time (whereas real fluids have a relaxation spectrum), does not shear-thin, and has a zero value of N_2. More seriously, in extensional flows it can produce an unbounded extensional viscosity because of the linear spring behaviour of the dumbbells. In a real fluid, the molecules become fully extended and the viscosity saturates.

1.3.4 Upper-Convected Maxwell model

The Upper-Convected Maxwell fluid (UCM) is the high-concentration limit of an Oldroyd-B fluid (section 1.3.3 above). As such, it is used as a model for polymer melts.

It is given by:

$$\boldsymbol{\sigma} = -p\boldsymbol{I} + \boldsymbol{\sigma}^{p} \tag{1.14}$$

[2] In particular, we note that $\overset{\nabla}{\boldsymbol{I}} = -2\boldsymbol{E}$.

$$\boldsymbol{\sigma}^p + \lambda \overset{\nabla}{\boldsymbol{\sigma}}^p = \boldsymbol{I}. \tag{1.15}$$

It has all the disadvantages of the Oldroyd-B fluid: unbounded extensional viscosity, single relaxation time, zero N_2 and constant shear viscosity. However, because it has one less parameter, it is mathematically even more simple than the Oldroyd-B fluid. In some of the flows discussed in this dissertation, we will see that the equations of motion are analytically tractable for a Maxwell fluid, where they are not for Oldroyd-B.

1.3.5 Nonlinear dumbbell models

The problem of infinite extensional viscosity for finite extension rate in the Oldroyd-B fluid is caused by unbounded extension of the dumbbells. Thus, a sensible modification of the model is to use a nonlinear force law and limit the maximum extension of the springs:

$$\boldsymbol{F} = G\boldsymbol{R}f(R);\ \ f(R) = \frac{1}{1 - R^2/L^2} \tag{1.16}$$

where $R^2 = \boldsymbol{R}.\boldsymbol{R}$. This leads to the set of *Finitely Extensible Nonlinear Elastic (FENE)* models. Because of the nonlinearity in $\boldsymbol{F}$, a closed evolution equation for $<\boldsymbol{RR}>$ (and hence for the stresses) is not available; a closure approximation is needed.

FENE-P

If the average length of all dumbbells is taken to define R, the force law $f(R)$ is replaced by $f(<R>)$, giving a *pre-averaging* approximation:

$$\boldsymbol{F} = G\boldsymbol{R}f(<R>) \tag{1.17}$$

which leads (Peterlin [157]) to the FENE-P model:

$$\boldsymbol{\sigma}^p = <\boldsymbol{RF}> = G<\boldsymbol{RR}>f(<R>) \tag{1.18}$$

and therefore:

$$\boldsymbol{\sigma} = -p\boldsymbol{I} + 2\eta_s\boldsymbol{E} + Gf(R)\boldsymbol{A} \tag{1.19}$$

$$\boldsymbol{A} + \frac{\lambda}{f(R)}\overset{\nabla}{\boldsymbol{A}} = \frac{\lambda}{f(R)}\boldsymbol{I} \tag{1.20}$$

where, in this case:

$$R^2 = tr(\boldsymbol{A}). \tag{1.21}$$

FENE-P improves the behaviour of the model in extension, and gives a shear-thinning viscosity. It is therefore less good at describing shear flows of Boger fluids.

FENE-CR

In this model, the extension behaviour remains of FENE type, but the evolution of the quantity $\boldsymbol{A}$ is altered from the FENE-P equation (1.20) to give a *constant* shear viscosity. It becomes (Chilcott & Rallison [39]):

$$\boldsymbol{A} + \frac{\lambda}{f(R)}\overset{\nabla}{\boldsymbol{A}} = \boldsymbol{I}. \tag{1.22}$$

1.3.6 Other rate equations

Several other *ad hoc* modifications of the Oldroyd-B model have been proposed. We add an extra term to equation (1.11) to produce any or all of:

shear-thinning, nonzero N_2 or a bounded extensional viscosity. The Oldroyd-B model may be expressed as:

$$\boldsymbol{\sigma}^p + \lambda \overset{\nabla}{\boldsymbol{\sigma}}^p = 2\boldsymbol{E}. \tag{1.23}$$

Without violating any of the simple fluid assumptions we may add an extra term:

$$\boldsymbol{\sigma}^p + \lambda \overset{\nabla}{\boldsymbol{\sigma}}^p + \boldsymbol{f}(\boldsymbol{\sigma}^p, \boldsymbol{E}) = 2\boldsymbol{E}. \tag{1.24}$$

Some of the popular choices for $\boldsymbol{f}$ are:

Johnson-Segalman [89]

$$\boldsymbol{f}(\boldsymbol{\sigma}^p, \boldsymbol{E}) = \alpha\lambda(\boldsymbol{E}.\boldsymbol{\sigma}^p + \boldsymbol{\sigma}^p.\boldsymbol{E}) \tag{1.25}$$

Phan-Thien Tanner (PTT) [160]

$$\boldsymbol{f}(\boldsymbol{\sigma}^p, \boldsymbol{E}) = \alpha\lambda\{\boldsymbol{E}.\boldsymbol{\sigma}^p + \boldsymbol{\sigma}^p.\boldsymbol{E}\} + [Y(tr(\boldsymbol{\sigma}^p)) - 1]\boldsymbol{\sigma}^p \tag{1.26}$$

where:

$$Y(x) = e^{-\epsilon\lambda x}. \tag{1.27}$$

Giesekus [68]

This is a generalisation of the UCM fluid (using an anisotropic drag force), so we set $\eta_s = 0$ and use:

$$\boldsymbol{f}(\boldsymbol{\sigma}^p, \boldsymbol{E}) = \alpha\lambda\boldsymbol{\sigma}^p.\boldsymbol{\sigma}^p \tag{1.28}$$

where $0 \leq \alpha \leq 1$.

The detailed expressions for η, N_1 and N_2 are given in [112].

1.3.7 Retarded motion expansions (nth order fluid)

If the motion is weak and slow enough (or, correspondingly, the longest relaxation time is relatively short), any simple fluid may be expanded as a perturbation to the Newtonian limit (Rivlin & Ericksen [178]). The small quantity used in the expansion is either the *Weissenberg number*, W (often Wi), or the *Deborah number*, De:

$$\begin{aligned} W &= \lambda U/L \\ De &= \lambda/T. \end{aligned} \tag{1.29}$$

These are both nondimensionalisations of the relaxation time λ. W uses a typical velocity gradient or shear-rate, while De, for unsteady flows, uses a typical timescale of the flow. If these are both small, then the retarded motion expansion will be valid, and the form of the result is independent of the specific constitutive equation used.

These equations are known as nth-order fluids according to how many powers of the small quantity are retained. In particular, the second-order fluid is given (Coleman & Noll [45]) by[3]:

$$\boldsymbol{\sigma} = -p\boldsymbol{I} + 2\eta\boldsymbol{E} + 4\Psi_2\boldsymbol{E}.\boldsymbol{E} - \Psi_1\overset{\nabla}{\boldsymbol{E}} \tag{1.30}$$

where η, Ψ_1 and Ψ_2 are constants.

These equations are useful where a phenomenon arises from the effect of very weak elasticity.

[3] In [113], Larson incorrectly gives this as:

$$\boldsymbol{\sigma} = -p\boldsymbol{I} + 2\eta\boldsymbol{E} + 4\Psi_2\boldsymbol{E}.\boldsymbol{E} - 2\Psi_1\overset{\nabla}{\boldsymbol{E}}$$

which leads to $N_1 = 2\Psi_1\dot{\gamma}^2$ in simple shear.

1.3.8 Doi-Edwards model

The Doi-Edwards model (Doi & Edwards [51, 52, 53, 54]) is a specific example of a K-BKZ fluid (Kaye [97], Bernstein, Kearsley & Zapas [16]), for which:

$$\boldsymbol{\sigma} = 2\int_{-\infty}^{t}\left[\frac{\partial}{\partial I_1}X(I_1,I_2,t-t')\boldsymbol{C}^{-1}(t,t') - \frac{\partial}{\partial I_2}X(I_1,I_2,t-t')\boldsymbol{C}(t,t')\right]dt'. \tag{1.31}$$

$\boldsymbol{C}(t,t')$ is the strain tensor accumulated between past time t' and current time t, and I_1 and I_2 are its two invariants: $I_1 \equiv tr(\boldsymbol{C})$ and $I_2 \equiv tr(\boldsymbol{C}^{-1})$. X is a general damping function, which defines a specific model within the class.

The Doi-Edwards model describes melts in which individual molecules move by reptating along their length. This is given by:

$$X(I_1,I_2,s) = \chi(I_1,I_2)m(s) \tag{1.32}$$

with:

$$m(s) = G\sum_{p\ \text{odd}}^{\infty}\frac{8}{\pi^2}\frac{1}{p^2}\frac{1}{\lambda_p}\exp(-s/\lambda_p); \quad \lambda_p = \lambda_1/p^2 \tag{1.33}$$

and an approximate form for χ (Currie [47]) by:

$$\chi = \tfrac{5}{2}\ln(J-1) - 4.87; \quad J = I_1 + 2\left(I_2 + \tfrac{13}{4}\right)^{1/2}. \tag{1.34}$$

This model predicts a very high level of shear-thinning, even higher than that observed in real polymer melts.

1.3.9 Models with viscometric functions of $\dot{\gamma}$

An *ad hoc* method of extending many models to melt-like behaviour (to include substantial shear-thinning, for example) is to let some of the material

parameters become functions of $\dot{\gamma} = |\sqrt{2\boldsymbol{E} : \boldsymbol{E}}|$. These functions may then be determined by simple-shear viscometry, or assigned simple mathematical forms.

Convenient mathematical forms which go some way to approximating real material quantities include the power-law function:

$$\eta(\dot{\gamma}) = \eta_0 \dot{\gamma}^{(n-1)} \tag{1.35}$$

and the Carreau model [28]:

$$\eta(\dot{\gamma}) = \eta_\infty + (\eta_0 - \eta_\infty)(1 + (a\dot{\gamma})^2)^{(n-1)/2}. \tag{1.36}$$

Generalised Newtonian fluid

The Newtonian fluid is given by equation (1.5). To form the *generalised Newtonian fluid*, the viscosity η_s is allowed to depend on $\dot{\gamma}$. The fluid exhibits no normal stress effects, and is therefore not very useful for instability calculations.

CEF fluid

The second-order fluid is given by:

$$\boldsymbol{\sigma} = -p\boldsymbol{I} + 2\eta\boldsymbol{E} + 4\Psi_2\boldsymbol{E}.\boldsymbol{E} - \Psi_1\overset{\nabla}{\boldsymbol{E}}. \tag{1.37}$$

If all three material properties η, Ψ_1 and Ψ_2 are allowed to be functions of $\dot{\gamma}$, this becomes the *CEF equation* (Criminale, Ericksen & Filbey [46]). This is the simplest model to allow exact correspondence with all the observed viscometric functions.

The Reiner-Rivlin equation (Reiner [170], Rivlin [177]) is a specific example of a CEF fluid:

$$\boldsymbol{\sigma} = -p\boldsymbol{I} + 2\eta(\dot{\gamma})\boldsymbol{E} + 4\Psi_2(\dot{\gamma})\boldsymbol{E}.\boldsymbol{E}. \tag{1.38}$$

White-Metzner fluid

If we permit the time constant λ in the Upper-Convected Maxwell fluid (section 1.3.4) to be a function of $\dot{\gamma}$, we obtain the *White-Metzner* model (White & Metzner [214]):

$$\boldsymbol{\sigma}^p + \lambda(\dot{\gamma})\overset{\nabla}{\boldsymbol{\sigma}^p} = \boldsymbol{I}. \tag{1.39}$$

This model can show normal stress effects and shear-thinning, while retaining the physical structure of a dumbbell model.

1.3.10 Summary

The brief description above indicates that a wide class of constitutive equations is available, and 'better' descriptions generally necessitate more dimensionless groups. The simplest equations that correctly describe shear flows of solutions and melts are the Oldroyd-B and White-Metzner models, and we shall focus on these, employing more sophisticated versions only when necessary.

1.4 Observations of instabilities in flows of non-Newtonian fluids

We offer here a brief and incomplete review of the range of instabilities seen in the processing of non-Newtonian fluids. Fuller coverage of these phenomena is given by Shaqfeh [182], Larson [113], and earlier by Tanner [197] and Petrie & Denn [158].

We begin with interfacial instabilities (section 1.4.1), one of which is also studied in chapter 3. We then consider inertialess instabilities in flows with curved streamlines (section 1.4.2), instabilities in extensional flows (section 1.4.3), and then more complex flows (section 1.4.4). Finally (in section 1.4.5), we discuss some instabilities observed in extrusion processes, where there is neither an interface nor curvature of the streamlines.

The channel flows studied in the bulk of this dissertation are relevant to extrusion problems, in that the flow inside an extrusion die has an effect on the flow downstream of the die exit, and on the quality of the extruded product; in addition, since shear is a feature of almost all flows in confined geometries, any instability of a shear flow has implications for polymer processing in general.

1.4.1 Interfacial instabilities in channel and pipe flows

Many practical processes (coextrusion, multi-layer coating, lubricated pipelining) involve multi-layer flows of viscoelastic liquids, because of the desirable properties of many multi-layer polymeric solids. A multi-layer material may have enhanced strength, or a combination of the properties of its com-

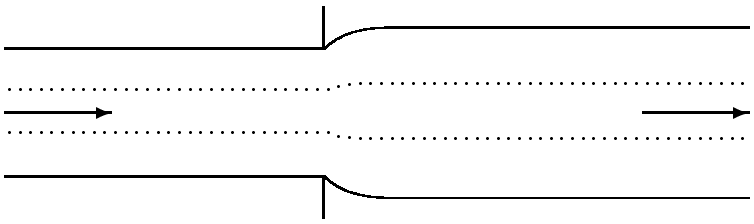

Figure 1.4: Schematic of three-layer coextrusion, with flow from left to right

ponents (for example, in food wraps the coating may provide adhesion and the core a moisture barrier). Figure 1.4 shows a schematic of three-layer extrusion, in which the product would be cooled at the far right of the picture to obtain a solid film. Usually a uniform interface is desired in the end product, so instabilities are to be avoided if possible.

The detrimental effect of interfacial instability is illustrated in figure 1.5. This shows how the optical quality of the final product is impaired by an instability during processing.

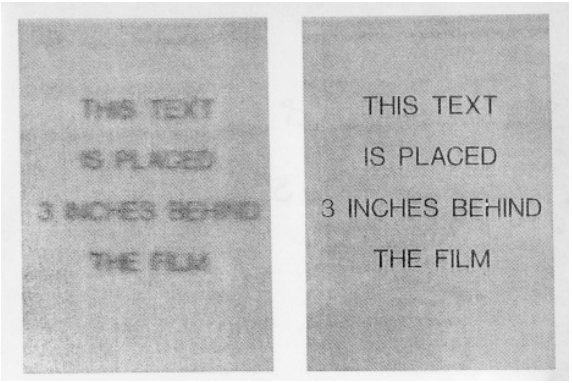

Figure 1.5: A photograph of the effect of interfacial instability on the optical quality of a three-layer coextruded film. The film on the left is the product of a flow with an unstable interface, while that on the right was produced by a stable flow. Mavridis & Shroff [134].

Many experiments on the stability of multi-layer flows in straight pipes and channels have been carried out by Yu & Sparrow [223], Lee & White [119] and Khomami & coworkers [215, 216, 217, 103].

1.4.2 Viscometric flows having curved streamlines

In 1996, Shaqfeh published a review of purely elastic instabilities [182]. Many of the bulk instabilities (*i.e.* not surface instabilities) in this section are covered by the review article, and have a common mechanism: the coupling of a first normal stress difference N_1 with curvature of the base-flow streamlines. The mechanism therefore differs from the coextrusion instability in section 1.4.1.

Taylor-Couette

Inertial effects at high Reynolds numbers cause the Taylor-Couette instability (Taylor [199]). The fluid forms toroidal roll cells with a regular spacing up the column of fluid (shown in figure 1.6). The mechanism for this instability is centrifugal.

First observed experimentally by Giesekus [69], the purely elastic Taylor-Couette instability also appears in the form of a cellular secondary flow. It is visually the same as the inertial instability, but can occur at zero Reynolds number. The instability is driven by N_1 (which forms a hoop stress when the streamlines are closed), which has a destabilising effect, comparable to, but opposite in sign to, the centrifugal force in the inertial case. It was predicted theoretically for an Oldroyd-B fluid by Larson *et al* [115], confirming earlier Boger-fluid experiments by the same group in Muller *et al* [145]. It is

interesting to note that Oldroyd-B shows good quantitative agreement with experiments on polymer solutions, for this shear dominated instability.

Different modes of elastic instability were observed by Beris & Avgousti [15], and the range of transitions was investigated by Baumert & Muller [11], using Boger fluids. Further theoretical work on the different parameters affecting the basic instability has been carried out by Shaqfeh *et al* [184], and by Larson *et al* [114]. In the fully nonlinear experimental range, a new phenomenon called the Solitary Vortex Pair (a pair of asymmetric rolls isolated from any others) was found, and a possible mechanism explained, by Groisman & Steinberg in [72].

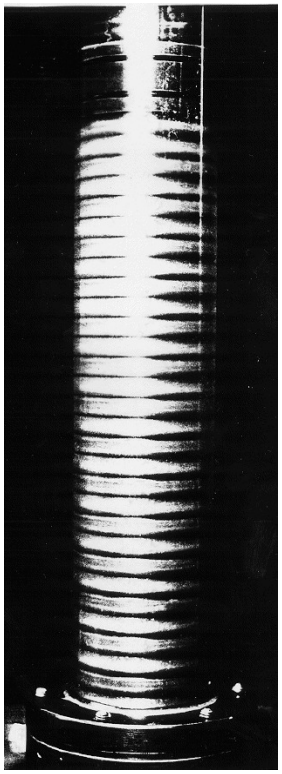

Figure 1.6: Inertial Taylor rolls in a Couette device.

If the cylinders are not quite concentric, the instability is somewhat modified, as explained experimentally and theoretically by Dris & Shaqfeh [56], and numerically, using a UCM fluid, by Chawda & Avgousti [30].

In Dean or Taylor-Dean flow, there is another, different elastic instability, first reported by Joo & Shaqfeh [92]. The same authors also studied the effect of inertia in [91], and carried out a survey of experimental observations coupled with calculations for an Oldroyd-B fluid in [93].

Cone-and-plate/Plate-and-plate

Both of these geometries consist of a rotating upper surface (cone or plate) and a fixed lower surface (plate), between which the fluid is sheared.

Surface modes

One elastically driven instability is distortion of the meniscus. It takes one of two forms: either an axisymmetric smooth distortion which indents the middle of the meniscus (known as 'edge fracture'), or an irregular distortion whose effect looks like surface vortices (referred to by Larson simply as 'fracture').

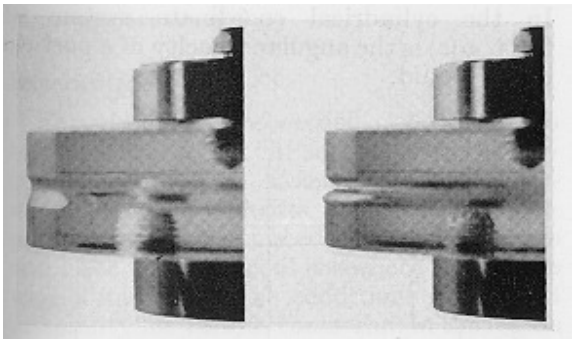

Figure 1.7: The smooth distortion known as 'edge fracture' in a cone-and-plate geometry. Photograph taken from Hutton [85].

The edge fracture effect was observed first by Hutton [85]. Tanner & Keentok [198] analysed it in cone-and-plate flow, and showed that it is critically dependent on the second normal stress difference N_2. This was confirmed experimentally by Lee *et al* [120].

The fracture effect, first observed by Kulicke *et al* [107, 108], occurs for entangled solutions and melts. It is not known how deep into the fluid the

surface disturbance acts. An experimental indicator here seems to be the behaviour of measured values of N_1/σ_{12}; when plotted against σ_{12}, there is a sudden change in slope at the onset of fracture. This is in common with 'gross melt fracture', an extrusion instability discussed in section 1.4.5.

Bulk mode

Using a Boger fluid in a cone-and-plate device, Jackson *et al* [87] observed a dramatic rise in both σ_{12} and N_1, well after the beginning of the motion. Following further experiments with Boger fluids in both cone-and-plate and plate-and-plate geometries, a secondary flow was found by Magda & Larson in 1988 [130], indicating that Jackson's observations were caused by the appearance of an instability in the flow. This deduction was not immediately accepted: as recently as 1991, anomalous shear-thickening effects were being reported from measurements made only in the cone-and-plate device (pointed out by Tam *et al* [196]).

Experiments by McKinley *et al* [136] thoroughly summarise the behaviour

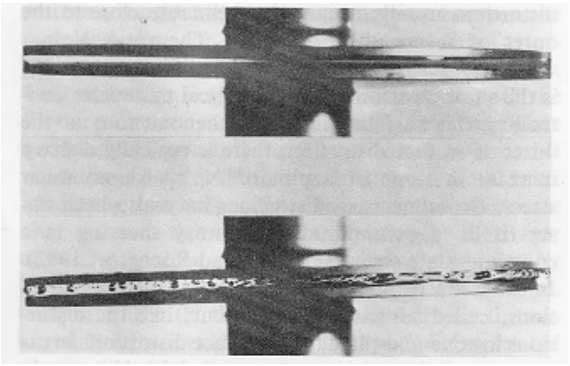

Figure 1.8: The irregular distortion known as 'fracture' in a cone-and-plate geometry. Observations from Kulicke *et al* [107].

of a polyisobutylene/polybutene solution in both these geometries, finding the conditions for onset of instability in terms of a critical Deborah number.

A more recent experimental discovery (Byars *et al*, 1994 [23]) is a second critical radius (which corresponds to a higher critical Deborah number) in the parallel-plate geometry, outside which the flow of polyisobutylene restabilises.

The earliest theoretical prediction of an elastic instability in this geometry was by Phan-Thien [159], who predicted a spiral form for the secondary flow. However, the experimentally observed secondary flow is not of this form, but consists rather of ring vortices at irregular radial spacings.

The form of the instability is predicted theoretically by Öztekin *et al*: in the parallel-plate geometry using the Oldroyd-B fluid [152], and in the cone-and-plate using a multi-mode Giesekus model [153]. They compare these predictions with experiments with polyisobutylene, polybutene and tetradecane fluids. The same group then extends this analysis to a systematic study of the effect of various parameters [137]. The cone-and-plate flow of an Oldroyd-B fluid is analysed by Olagunju [148].

1.4.3 Instabilities in extensional flows

The purest 'steady extensional flow' in general use is that imposed in a filament stretching rheometer (Tirtaatmadja & Sridhar [200]). In this device, two plates with fluid between them are moved rapidly apart; both the evolution of the radius of the resulting filament at its midpoint, and the force exerted on the endplates can be measured. However, in industrial processing, several other extensional flows are commonly used, and it is here that the first instabilities were observed.

Instabilities in melt spinning

In a melt spinning or fibre-spinning process, a fluid (the melt) is extruded relatively slowly and then, some distance down the processing line, taken up rapidly onto a wheel. Because the velocity at the wheel is much larger than that at the exit of the extrusion die, the fibre undergoes extensional flow and becomes much thinner during processing. A schematic representation of the flow is given in figure 1.9; the aspect ratio of draw length to fibre diameter is many times larger in a real process.

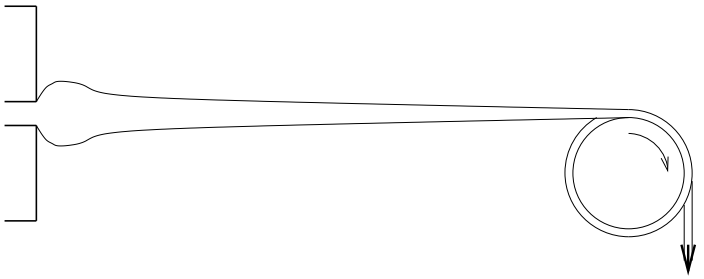

Figure 1.9: Schematic of a spin-line flow

Draw resonance

Draw resonance is a periodic variation in fibre diameter. It occurs only for constant take-up speed at the spool, and not for constant force (Pearson & Matovitch [155]). It is the result of a variation in cross-sectional area of the fibre at the take-up spool, causing a change in the spinline tension, which in turn enhances the upstream disturbance.

For a Newtonian fluid, the instability was first described by Christensen [41] and Miller [141]. The first classical one-dimensional analysis, using an

isothermal Newtonian fluid and no gravity, inertia, surface tension or air drag, was performed independently by Kase *et al* in 1966 [96] and Matovitch & Pearson in 1969 [133]. They both proved fibre spinning to be unstable for draw ratios greater than 20.21.

Using melts with constant shear-viscosity, the onset of draw resonance occurs, as for the Newtonian case, at a draw ratio of just over 20, independent of whether they thicken or thin under strain (first observed in 1975 by Donnely & Weinberger [55], Cruz-Saenz *et al* [213], and Ishihara & Kase [86]). This last paper (along with Lamb [111]) also demonstrated an upper draw ratio above which, at least for short fibres, the flow restabilises.

In general, shear-thinning enhances the instability, lowering the critical draw ratio by up to an order of magnitude (Zeichner [224]). A linear stability analysis was carried out by Fisher & Denn [65] for a shear-thinning generalisation of the UCM fluid, and it is in qualitative agreement with isothermal experiments.

In recent years, the field of fibre-spinning has extended to include multilayer film casting, in which layers are first extruded and then stretched, in a broadly two-dimensional geometry. The application of linear stability analysis to the corresponding core-annular flow has been performed for different fluid combinations: UCM skin with Newtonian core (Lee [122]), and PTT skin with Newtonian core (Ji *et al* [88]). For both of these, the viscoelastic skin acts to stabilise the flow, and delays the onset of draw resonance. Lee & Park [123] have performed one set of experiments in this field, using linear low density polyethylene in the core and low density polyethylene for the skin. Their results are in qualitative agreement with isothermal linear

stability calculations.

Necking

Even for a constant-force take-up of the spun fibre, when draw resonance does not occur, small indentations in the fibre surface can grow as they are convected down the fibre. This necking instability occurs for Newtonian fluids, but is usually inhibited in viscoelastic fluids because of strain-hardening. However, if a melt is extension-thinning (as, for example, predicted by the Doi-Edwards model), then samples in extension will neck and fail before extensional viscosity measurements can be made. This makes verification of models for such fluids very difficult. The neck mechanism for failure of spinnability has been observed by Chen *et al* [31] and Takaki & Bogue [195].

Cohesive failure

In melt spinning, a fibre may break with a mechanism quite distinct from necking. When the stresses in the fluid exceed the cohesive strength of the material, it will fracture. This mechanism was made clear by Ziabicki & Takserman-Krozer [225, 226, 227, 228, 229, 230, 231, 232], using oils of different molecular weights.

The critical stresses observed for this phenomenon (Vinogradov [207]) are comparable to those observed at the onset of gross melt fracture in extrusion (section 1.4.5).

Instabilities in film blowing

The film blowing process consists of extrusion of an annulus of polymeric

fluid, followed by its inflation (an extensional flow) by air injected along the axis of the extrusion die. The film is then cooled and taken up onto a roll in a manner similar to fibre spinning.

If insufficient air is injected, the film will not inflate and this process becomes little more than annular fibre spinning. As such, it is of course prone to draw resonance in exactly the same way as a normal fibre.

With sufficient injected air to form a film 'bubble', three main types of instability are observed, all shown by Minoshima & White [142]. The first, called 'bubble instability' by Larson, is a periodic axisymmetric variation in the bubble radius. This was first reported by Han & Park [74]. There is also a helical instability, and finally a solidification instability in which, without changing the bubble shape, the solidification front moves back and forth on the bubble surface. All three of these phenomena are stabilised by extension-thickening.

The first linear stability analysis of this flow for a viscoelastic fluid (UCM) was by Cain & Denn [27], who found instability to both blow-up and collapse of the bubble. More recently, Andrianarahinjaka & Micheau [3] have performed a numerical linear stability analysis, and found a strong dependence on the rheology of the fluid and on the cooling process.

1.4.4 More complex flows

Most flow geometries involve both shear and extension. As a consequence, a combination of mechanisms may arise to generate instabilities.

Instabilities in stagnation point flows

The archetypal stagnation point flow is a simple steady uniaxial straining flow $\boldsymbol{u} = \dot{\epsilon}(x, -\frac{1}{2}y, -\frac{1}{2}z)$. Experimentally, this is approximated using an opposed-jets device, and its two-dimensional equivalent using a cross-slot device (illustrated in figure 1.10).

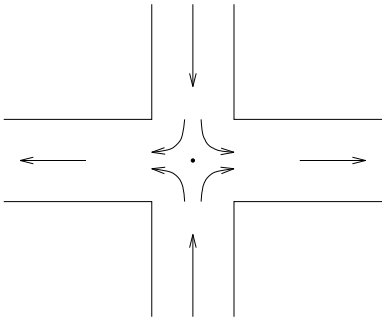

Figure 1.10: The cross-slot device for a stagnation point flow

In experiments using concentrated solutions and melts, a birefringent strand of highly extended material forms along the extension axis. At higher flow rates, this is replaced by a cylinder or 'pipe', as observed by Odell *et al* [147].

Both the birefringent line and the pipe have also been predicted theoretically (for a FENE model) by Harlen *et al* [75].

At still higher flow rates, a phenomenon called 'flare' is observed in the experiments, in which the birefringent region is disturbed and is spread throughout the geometry. Odell *et al* have suggested a mechanism involving a molecular entanglement structure. However, Harris *et al* [76], using a linear-locked dumbbell model, find a hydrodynamic instability to sinuous waves on the birefringent strand. A third possible explanation is given by the

presence of curved streamlines, which can lead to the elastic shear instability described in section 1.4.2.

Axisymmetric contraction flows

For both Newtonian and non-Newtonian fluids, the basic stable steady flow through a contraction (where it exists) consists of an extensional region near the centre of the flow, with a toroidal secondary vortex flow in the salient corner (Moffatt [143]), as shown in figure 1.11.

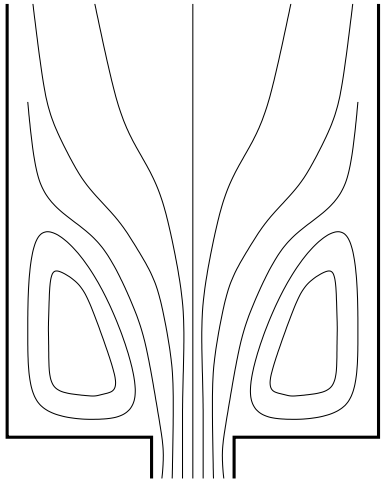

Figure 1.11: Schematic of contraction flow with recirculating vortex

The flow is subject to several different modes of instability, first observed by Cable & Boger [24, 25, 26] and summarised by McKinley *et al* [139] and Koelling & Prud'homme [104]. The choice of mode is sensitive to contraction ratio and fluid rheology. The centre region of the fluid may swirl (Bagley & Birks [6], den Otter [49], Ballenger & White [10], Oyanagi [150]) or pulse; and a lip vortex may form and become quasiperiodic.

Numerically, studies have been made using the Giesekus model (Hulsen & van der Zanden [83]) and the Oldroyd-B model (Yoo & Na [222]), with moderate success at predicting the experimental observations of instability. This flow has curved streamlines as well as extension, and so the mechanisms of section 1.4.2 may be partly responsible for the observed instabilities.

Planar contractions

In a planar geometry, there are two corner vortices; experimentally, it is observed that they may grow for a shear-thinning solution (Evans & Walter [62, 63]), but not for Boger fluids. At high flow rates, these vortices show instability to three-dimensional motions, and the resultant flow is usually time-dependent (Giesekus [70]).

Wakes

The wake behind a falling sphere in a shear-thinning fluid may exhibit time-oscillatory flow (Bisgaard [20]) in the region just behind the sphere, where high extensional stresses occur (Chilcott & Rallison [39] and others). However, for constant-viscosity fluids (Boger, UCM, Chilcott-Rallison, PTT) there is no experimental or theoretical evidence of this instability (Arigo *et al* [4]).

McKinley *et al* [135] have observed an instability, which cannot be an effect of shear-thinning, in the wake of a circular cylinder confined in channel flow of a viscoelastic, constant-viscosity fluid.

More recently, both Chmielewski & Jayamaran [40] and Khomami & Moreno [102] have observed similar instabilities at Deborah numbers of order

1, in experiments with periodic arrays of cylinders.

1.4.5 Extrudate distortions and fracture

One of the most striking examples of flow instability is provided by evidence of distortion of extrudates. Many competing mechanisms are available; many complementary descriptions have been provided.

In [105], Kolnaar & Keller divide extrusion instabilities into three broad classes: surface distortions (sharkskin); periodic distortions with wavelengths comparable with the extrudate diameter (wavy instability); and gross shape distortions (gross melt fracture), and show that each effect has a different stress criticality.

The division into these three régimes, and particularly the separation of wavy distortions from gross melt fracture, has only taken place relatively recently in the literature, with these last two being grouped together (with misleading terminology) as 'fracture'.

There are other unstable régimes possible: Vinogradov *et al* [209] and many more recent experimenters have found a global stick-slip flow in which the extrudate alternates between smooth and distorted states while the upstream pressure fluctuates with the same frequency. Compressibility of the melt is a crucial ingredient here.

It should be noted also that all viscoelastic fluids exhibit the stable distortion of die-swell in extrusion, in which the elastic recovery of the fluid after the straining and shearing flows inside the die causes the radius to swell just after exit from the die. This is not a true instability and will not be discussed further.

Sharkskin

The mildest instability that occurs in the extrusion of polymer melts is a surface distortion. At its weakest, it is little more than loss of gloss (Ramamurthy [169]), and in its stronger form, known as sharkskin, it appears as a series of scratches across the extrudate, mainly perpendicular to the flow direction. Piau *et al* [163] show clear photographs of the phenomenon (an example is shown in figure 1.12), that distinguish it from other extrudate distortions.

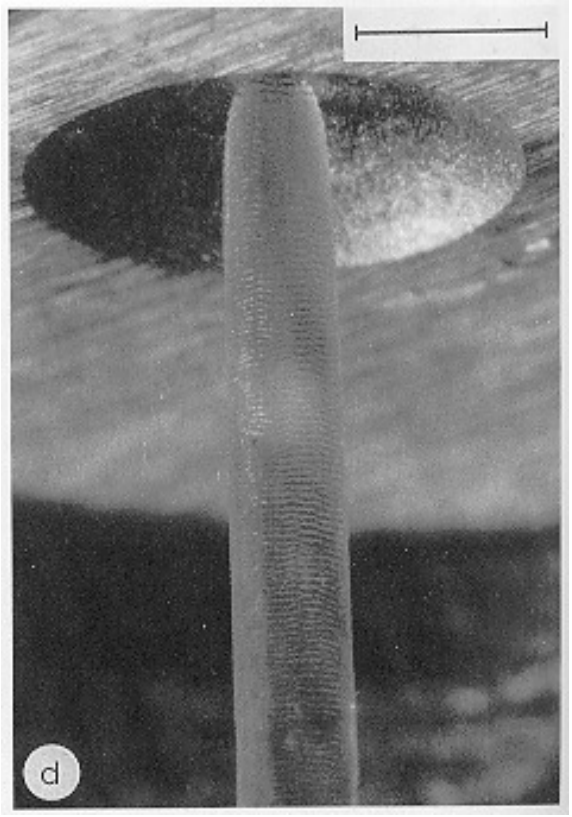

Figure 1.12: Experimental observation of the sharkskin instability, reprinted from Piau *et al* [163] with permission from Elsevier Science. The scale shown is 1mm long.

It was first reported by Clegg in 1958 [42], and was shown by Benbow & Lamb [13], and later by Moynihan *et al* [144] to be initiated at the exit of the die. This was confirmed more recently by Kolnaar & Keller [105]. Vinogradov *et al* [209] demonstrated that sharkskin is associated with high local stresses at the die exit, and more recently (Ramamurthy [169], Moynihan *et al* [144], Hatzikiriakos & Dealy [78], Piau *et al* [162]) it has been shown that in general the die surface material, or the presence of lubricants on the die wall, has a strong effect on the appearance of sharkskin.

Pomar *et al* [166] considered solutions of linear low density polyethylene and octadecane; they found that the onset of sharkskin was at constant ratio of wall shear stress to plateau modulus. However, for general low density polyethylenes, Venet & Vergnes [206] showed that wall shear stress is not the unique determinant of sharkskin effects and that chain branching and strain hardening may inhibit the effect.

The current consensus is that sharkskin is caused by some kind of adhesive fracture and/or phase separation at the die exit, due to the high local stresses there, rather than any effect occurring over the whole die length. The current literature proposes several different mechanisms.

Phase separation

Busse [22] suggests that the polymer will segregate under stress into low- and high-molecular weight components close to the die exit. Chen & Joseph [36] further showed how this could cause a short-wave instability, which could propagate out of the die and onto the extrudate surface. This possibility is discussed further in chapter 5. Joseph [94] predicted the wave shape of sharkskin using theory from the lubrication

of heavy oils by water in pipelining.

Wall-slip

Hatzikiriakos [77] simulates extrusion flow using 'slip conditions' and matches his own experimental data. In the same vein, Shore *et al* [186, 185] use a Maxwell model with a first-order stick-slip boundary condition to investigate stability. On studying their system numerically they find that it too can predict sharkskin. Experimentally, Tzoganakis *et al* [204], who quantify sharkskin by means of the fractal dimension of the extrudate surface, show that slip first appears in the die before the appearance of sharkskin.

For slippery dies, Piau *et al* [161] find that there are two separate slip regimes, at low and high stresses, with a transition zone in between. In both of these, the extrudate shows a crack-free surface. This quantifies the parameter régimes where slip is expected for polybutadiene, and may be an indication that a lack of slip is needed for sharkskin.

Molecular dynamics

Sharkskin is a small-scale instability, so it is possible that either of the above mechanisms will have its origin at the molecular scale. However, there are some papers whose approach is purely molecular, and whose predictions cannot simply be expressed in macroscopic terms.

Stewart & coworkers [190, 191] have proposed a molecular based model for wall-slip, which correctly predicts the wall behaviour at wall shear-rates below that critical for gross melt fracture.

Wang *et al* [210] consider sharkskin formation in linear low density

polyethylene, and, using a model for molecular interactions with the wall and with each other, can predict sharkskin. Their mechanism is a combination of interfacial slip and cohesive failure due to chain disentanglement.

Cracking

Tremblay [203] finds numerical evidence for a 'cracking' mechanism for sharkskin. For linear low density polyethylene, El Kissi & Piau [59] show that the experiments do not give conclusive evidence of a slip mechanism, but rather indicate a mechanism of cracking under high tensile stresses. In subsequent confirmation (El Kissi *et al* [60]), they watch the appearance of these cracks by using a polymer with a long relaxation time.

Some degree of dependence on die length has been found by Moynihan *et al* [144], but this can be explained by the assumption (Kurtz [109]) that the growth of the instability depends, to some extent, on the state of stress of the material arriving at the die exit.

Wavy distortions

The first report of any extrusion instability was by Nason in 1945 [146], who reported a helical form of extrudate at Reynolds numbers around 800–1000. It has since been observed at much lower Reynolds numbers, of order 10^{-15} (Tordella [202]), so inertia does not seem to be a critical ingredient. An example is shown in figure 1.13.

Helical extrudates can only form in cylindrical dies; their slit-die counterpart is regular large-amplitude ribbing (Atwood [5]).

This instability has been largely neglected in the literature, and either dismissed as 'practically Newtonian' or classed along with gross melt fracture (see below) which often follows it. However, Kolnaar & Keller [105] have shown that wavy motions originate in the interior of the die, which indicates a completely different mechanism from that for melt fracture. Pomar *et al* [166], using solutions of linear low density polyethylene and octadecane,

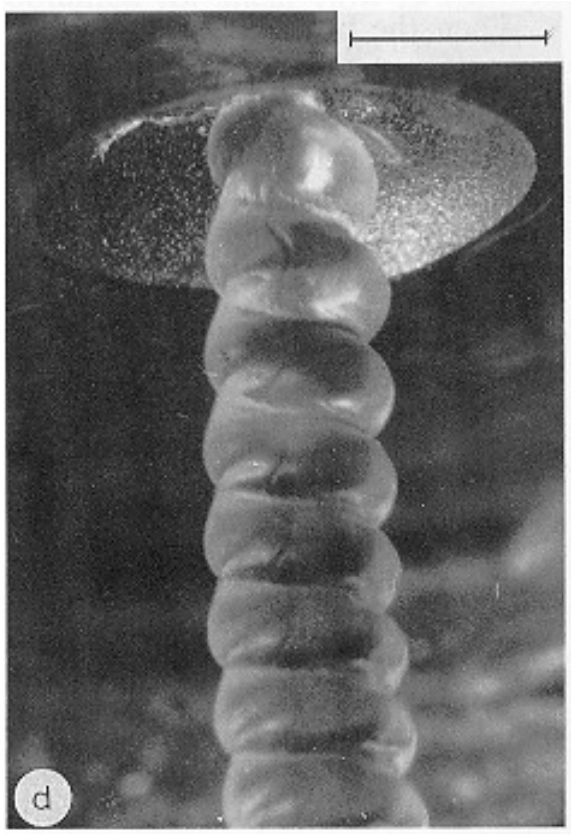

Figure 1.13: Helical instability observed by Piau *et al* [163], reprinted with permission from Elsevier Science. The scale shown is 1mm long.

found that the onset of a wavy instability, where it existed at all, was at constant wall shear stress. This supports the conclusion that the instability takes place entirely inside the die.

Sombatsompop & Wood [187], using natural rubber, observed evidence of steady slip at the walls, and a helical disturbance within the capillary.

Georgiou & Crochet [66] suggest that viscoelasticity is not vital for this instability. Simulating a compressible Newtonian fluid with an arbitrary nonlinear slip model for the wall boundary condition, they find self-excited oscillations in the velocity field, and a wavy interface.

However, an alternative explanation is an elastically-driven hydrodynamic instability of the steady flow through the die. This possibility is investigated in depth in this dissertation.

Gross melt fracture

Gross melt fracture, which is a chaotic disturbance of the extrudate, with diameter variations of 10% or more, was first observed and noted as such by Benbow & Lamb in 1963 [13]. However, evidence of gross melt fracture is available as early as 1958 (Tordella [202]), where it occurred after the onset of the wavy instability (above) and was called 'spurt' (figure 1.14).

Benbow & Lamb also showed that there is unsteady flow inside the die during the process. In fact (Vinogradov *et al* [209]) the time-dependent flow extends even into the inlet region of the die. Becker *et al*, in 1991 [12], report high levels of noise in the pressure in the upstream reservoir during processing.

Gross melt fracture cannot have an inertial mechanism, because it has

been observed for extremely low Reynolds numbers (Tordella [202]). Shear thinning is also not a critical factor, even if it plays a part, as illustrated by Cogswell *et al* [43]: they observed melt fracture in a fluid with constant shear viscosity. Similarly, thermal heating is not critical: Lupton & Regester [127] showed that in experimental conditions, shear heating will have an effect of at most 3 degrees. In addition, Clegg had earlier failed to find such an instability for a Newtonian fluid with viscosity very sensitive to temperature [42].

There is a strong difference between the behaviour of (broadly) linear and branched polymers, of which one manifestation is the frequency at onset of the instability. The linear polymers show roughly the same frequency throughout the flow development, whereas the branched melts show a low-

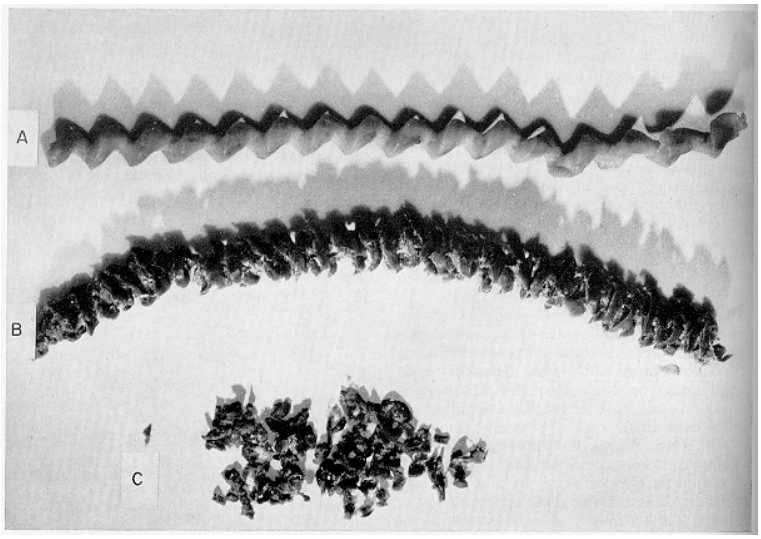

Figure 1.14: Extrudates produced by Tordella [202] at increasingly high flow rates: the first shows a wavy instability, the second gross melt fracture, and the third is completely fragmented.

frequency oscillation at onset, which increases as the amplitude of the distortion grows (den Otter [49]). For branched polymers, most evidence is consistent with a disturbance nucleated at the die entrance, and gradually decaying within the die (Bagley *et al* [7] give some early evidence).

For linear polymers, on the other hand, early evidence showed that the distortion increased (or at least did not decay) with increasing die length, and thus the distortion could have been nucleated inside the die (den Otter [50], Ballenger *et al* [9]). However, Kolnaar & Keller [105] show definitively that melt fracture originates at the entry of the die for the flow of linear polyethylene.

The mechanism assumed to cause fracture from the die entry (Benbow & Lamb [13]) is as follows: an upstream oscillatory flow near the die entrance could permit incorporation of material with a different flow history, thus causing large scale extrudate defects because of different elastic recovery. Such an upstream flow may occur as a result of the contraction flow instabilities of section 1.4.4. This fits with observations (for example, Cogswell & Lamb [44]) that streamlining the die entrance can reduce the instability. For linear polymers, if this is the case, the stability inside the die must still be marginal, since the distortion does not decrease with increasing die length.

Marginally stable flow inside the die may occur for two distinct reasons: wall-slip or constitutive instability.

Wall-slip seems to be very dependent on choice of fluid. For low density polyethylene, it is generally agreed that slip does not occur (den Otter [49, 50]), whereas for high density polyethylene the same papers report some observation of slip, and stick-slip is a possibility. Particular evidence in

favour of slip (Vinogradov & Ivanova [208]) is given by the dependence of the apparent wall shear rate on die radius.

Wall-slip is often modelled by replacing the traditional 'no-slip' condition at the wall with a slip-law, permitting a slip velocity which is some functional of strain history at the wall (see, for example, Pearson & Petrie [156]). Shore *et al* [186, 185] use a Maxwell model with a first-order stick-slip boundary condition, and find (with a numerical study) that they can predict melt fracture-like structures. Adewale *et al* [2] makle a theoretical study of the effect of a stick-slip mixed boundary condition, and find a resulting shear stress singularity. They claim that this singularity is the cause of melt fracture.

The existence of slip is supported by experimental observations (Benbow & Lamb [13], Atwood [5], Schowalter [181], El Kissi & Piau [58]) that, during gross melt fracture, the flow inside the die looks like plug flow (which may be intermittent). On the other hand, there is a general observation (Ramamurthy [169], Piau *et al* [163], El Kissi & Piau [58]) that the material used for the die does not have a strong effect on gross melt fracture. This suggests that in fact the plug flow is caused, not by slip at the wall, but by effective slip within the material itself, with the formation of a very thin region of high shear next to the wall. This could be caused by a *constitutive instability* (described in section 1.4.6).

Koopmans & Molenaar [106] raise the possibility of hydrodynamic instability where a nonlinear constitutive equation is used, with a proposal to use the energy balance equation to choose between different possible solutions of the governing equations. This method compromises between the alternative

mechanisms of slip at the wall and constitutive instability.

1.4.6 Constitutive instability

If there is a non-monotonicity in the stress/shear-rate curve for the fluid being extruded, then a shear stress could be attained that is a non-unique function of shear-rate, and the flow would undergo a sudden increase in flow rate. In practice, this is very difficult to distinguish from slip. This idea seems to have been put forward first by Huseby [84].

There are some fluids which, under simple shear, show a non-monotone shear stress/shear-rate curve. Examples include micellar solutions in which surfactant molecules have aggregated to form 'wormlike' structures (Spenley *et al* [188]). These materials can undergo a shear-banding motion, in which two different shear-rates are present at the same shear stress in a simple shearing flow. This was first observed experimentally in 1995, and is demonstrated in Decruppe *et al* [48] and Makhloufi *et al* [132].

Constitutive equations that show this non-monotonicity include the extended Doi-Edwards model (section 1.3.8), which shear-thins very rapidly at high shear-rates, the Johnson-Segalman model and the Giesekus model with a solvent viscosity. All have the generic form of stress curve, in which the shear stress passes through a maximum and a minimum as the shear-rate increases (figure 1.15). This behaviour can also be derived from an extended Doi-Edwards model, in which, once the shear-rate is larger than the slowest Rouse relaxation rate, the fluid acts as if it is unentangled.

McLeish & Ball [140] used this extended Doi-Edwards model to predict some critical features of spurt in polybutadiene and polyisoprene (Vinogradov

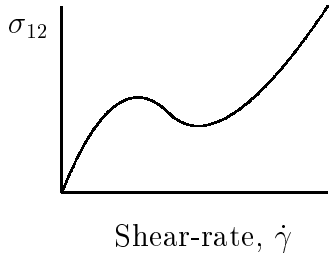

Figure 1.15: Typical plot of shear stress against shear-rate for a non-monotonic constitutive equation.

et al [209]).

In simple shear experiments with shear-banding fluids, two regions, each of one well-defined shear-rate, are typically observed, with a steady interface between them. Español *et al* [61] have performed numerical simulations of Couette flow of a Johnson-Segalman fluid, and found the fluid can model the experiments, including transient motion after start-up, with accuracy; showing a stable interface between the two regions.

However, Renardy [175] uses the Johnson-Segalman model and finds that in Couette flow of a fluid in which two regions use different shear-rates at the same stress level, there is a short-wave linear instability based around the interface between the regions.

1.5 Theoretical analyses of instability

1.5.1 Instabilities in inertialess parallel shear flows

There is a wealth of literature available on elastic perturbations to highly inertial flows. Elasticity is here a small effect, and for the purposes of this

review we focus on flows having small inertia.

For all such shear flows, Preziosi & Rionero [168] claim to prove stability by energy methods, but there is a fundamental error in the paper restricting its class of perturbations to a set which do not satisfy the momentum equation; the parent paper by Dunwoody & Joseph, [57], is correct but not applicable in the limit of low Reynolds number.

Squire's theorem [189] states that, in a two-dimensional flow of a Newtonian fluid, the most unstable disturbance is always two-dimensional, and so three-dimensional perturbations need not be considered (section 1.2). It also holds for the Upper-Convected Maxwell fluid [201], and for the second-order fluid if $\Psi_2 = 0$ [126].

Plane Poiseuille flow

The effect of elasticity on the known inertial instability in plane Poiseuille flow is destabilising. However, Ho & Denn [80] showed that Poiseuille flow of an Upper-Convected Maxwell fluid with no inertia is linearly stable to sinuous (or snakelike) modes. They also explained the numerical accuracy problems in previous papers, which had led to claims that the flow was unstable. The corresponding calculation for varicose (sausage-like) modes was performed by Lee & Finlayson [121], and this study also found stability. Finally, Ghisellini [67] used an energy argument to prove the stability analytically.

Similar results were found for the shear-thinning Giesekus fluid by Lim & Schowalter [125].

However, there is some hint of instability: for a Giesekus fluid, Schleiniger & Weinacht [180] studied Poiseuille flow, and found multiple solutions, along

with some possible selection criteria. These are proposed as a mechanism for spurt phenomena in extrusion. Using the K-BKZ model, Aarts & van de Ven [1] find similar results, with three steady states, two of which are stable. It is debatable whether these two papers (in each of which the base state is not obvious from the start) are showing flow or constitutive instabilities.

Couette flow

Gorodtsov & Leonov [71] found all the eigenvalues of the stability equation for inertialess Couette flow of the UCM fluid, and hence showed its stability. Renardy & Renardy [171] extended this numerically to low Reynolds numbers, and maintained stability.

1.5.2 Interfacial instabilities

The simplest multi-layer shear flow, and the first to be thoroughly analysed, is two-layer stratified Couette flow. It has been shown (Yih [221]) that viscosity stratification of Newtonian liquids can cause a long-wave inertial instability, for any nonzero Reynolds number. However, if the less viscous layer is thin, instability occurs at a finite Reynolds number (Hooper [81], Renardy [173]). In fact, this instability (if there is no surface tension) may exist for all wavenumbers (Renardy [172]).

In lubricated pipelining, a viscous core fluid (typically oil) is lubricated by a thin annulus of less viscous fluid (water) (Preziosi *et al* [167]). Stratification of viscosity can cause Yih's inertial instability, and density stratification also leads to long-wave instabilities. The flow has been investigated in detail by Chen & coworkers [36, 34, 8].

Moving away from Newtonian fluids, the effects of shear-thinning have been considered in different geometries by Waters & Keely [211, 212], Khomami [100, 101], and Wong & Jeng [219]. Yield fluids have been studied by Pinarbasi & Liakopoulos [165, 164].

Viscoelastic fluids can show a purely elastic instability at their interface, even in the limit of zero Reynolds number with matched viscosities. The linear stability of Oldroyd-B and UCM fluids has been investigated by Li [124], Waters & Keeley [212], Renardy [174], Chen & coworkers [33, 37, 38, 35] and (contained in chapter 3 of this thesis) Wilson & Rallison [218]; weakly nonlinear analysis has been undertaken by Renardy [176]. Li and Waters & Keeley used an incorrect stress boundary condition at the interface (Chen [32]), and hence did not find this instability.

The elastic instability is driven by a jump in N_1 at the interface, and exists in both the long- and short-wave limits. In the long-wave limit, stability depends on the volume fraction occupied by the more elastic component, but the short-wave limit depends only on the two materials, and the shear-rate at the interface. The mechanism of the long-wave instability has been explained by Hinch *et al* [79], and is summarised in chapter 3.

Using more than two different fluids, but with the same physical mechanisms causing the observed effects, theory has been carried out by Su & Khomami for power-law [192, 193] and Oldroyd fluids [194], and Le Meur [118] for PTT fluids.

Vertical flow, in which the driving force is gravity rather than an applied pressure gradient, and will therefore differ from one fluid to another where there is a density difference, has been investigated for viscoelastic fluids by

Sang [179] and Kazachenko [98].

Free surface flows

As in the case of viscosity-stratified multi-layer flows, free surface flows are susceptible to an inertial instability at any positive Reynolds number, however small (Benjamin [14], Yih [220], Hsieh [82]). Because of the stabilising influence of surface tension, long waves are the most unstable.

Asymptotic long-wave stability analysis has been carried out on this flow for the second-order fluid (Gupta [73]) and the Oldroyd-B fluid (linear analysis: Lai [110]; weakly nonlinear: Kang & Chen [95]). The linear analysis for these two fluids yields precisely the same result, and shows that with any nonzero elasticity the flow is unstable, even at zero Reynolds number. There is, therefore, a purely elastic mechanism for instability (Gupta [73]).

Using waves which are not asymptotically long (or, equivalently, a film which is not thin), Shaqfeh *et al* [183] have investigated the Oldroyd-B problem numerically, and showed that the growth rates are very small. Because this is a convective instability (moving downstream with the fluid), it can be convected out of the flow before it is big enough to be observed; and indeed it has never been seen in experiment. They also showed that elasticity has a stabilising influence on shorter waves.

1.5.3 Flows with curved streamlines

A new dimensionless group, to describe the curved-streamline instabilities of section 1.4.2, was introduced by Pakdel & McKinley [154], and explained with more examples by McKinley *et al* [138]. In all cases, the dominant

mechanism is a coupling of the curvature of the velocity field with the first normal stress difference, N_1. Some work specific to the cone-and-plate and parallel-plate geometries has already been discussed with the relevant experimental observations in section 1.4.2.

Flow in a curved channel also has curved streamlines, and an elastic instability was discovered for flow of an Oldroyd-B fluid by Joo & Shaqfeh [90]. The unstable mode is stationary, whereas the Taylor-Couette modes are overstable, so this mechanism is distinct from that which causes instability in the Taylor-Couette flow. Nonetheless, the instability is fundamentally dependent on the coupling of streamline curvature with the normal stress, N_1.

1.5.4 Stagnation point flow

The occurrence of a birefringent pipe in stagnation point flows, and its predicted instability, has already been discussed in section 1.4.4. In a cross-slot flow, Öztekin *et al* [151] predict a purely elastic instability (using the Oldroyd-B model), for which the unstable mode is fully three-dimensional (unlike the pipes and flare we have already seen). The mechanism is due to curved streamlines and normal stresses, in common with many of the instabilities of section 1.4.2.

1.6 Scope of this dissertation

As the brief account above indicates, the literature on instabilities in elastic liquids flows is extensive and rapidly developing. We have chosen to focus on

experimentally observed instabilities in interfacial flows, flows with curved streamlines, and extrusion, in which inertial forces are small.

In this dissertation, we first investigate theoretically an interfacial instability which occurs in coextrusion (chapter 3). We then consider whether the same mechanism can generate instability in straight-streamline flows of a single fluid whose material properties are advected with the flow (chapters 4 and 5). We shall refer to this as a 'coextrusion' instability even though only one fluid may be present: the fundamental mechanism is the same as that for the coextrusion case. This instability may provide a mechanism for the helical distortions of extrudates as discussed in section 1.4.5.

In chapter 6, we consider the channel flow of a shear-thinning fluid, and find evidence for another instability where the degree of thinning in the shear viscosity is high. The mechanism in this case is fundamentally different and we refer to it as the thinning instability.

By considering different constitutive models with similar physical properties, we determine a mathematical criterion for the 'coextrusion' instability depending on properties of the model itself, not just on the velocity and stress profiles of the base flow. In chapter 7, we give an example of two flows with identical flow profiles and stresses, but whose stability properties are different, as a result of differences in formulation of the fluid models. The fluids in question are generalisations of the two types of fluid already used: a fluid with advected properties like that of chapters 4 and 5, and a fluid whose viscometric properties are functions of the shear-rate, like that of chapter 6.

The principal conclusions from the dissertation, and suggestions for future work that result from it, are given in chapter 8.

Chapter 2

Stability of Channel Flows: General Formulation

2.1 Introduction

In the course of this dissertation we will use several different constitutive equations, all of rate type, and all suitable for shear-based flows.

To avoid duplication, a 'general' constitutive equation is proposed here which contains all the subsequent equations as special cases. The stability problem is posed in general terms: when each individual fluid is studied later, the specific parameter values will be substituted into the perturbation equations of section 2.6 or section 2.7.

2.2 Geometry

The basic geometry is a planar channel flow, sketched in figure 2.1. It is convenient to scale lengths by the half-width of the channel, L; velocities by that on the centreline of the channel, U_0; and stresses by $U_0\mu_*/L$, where μ_* is a typical viscosity.

2.3 Constitutive equations

We consider the following nondimensional constitutive equation:

$$\boldsymbol{\nabla}.\boldsymbol{u} = 0 \tag{2.1}$$

$$\boldsymbol{\nabla}.\boldsymbol{\sigma} = \mathbf{0} \tag{2.2}$$

$$\boldsymbol{\sigma} = -p\boldsymbol{I} + 2\mu\boldsymbol{E} + \frac{C}{W}\boldsymbol{A} \tag{2.3}$$

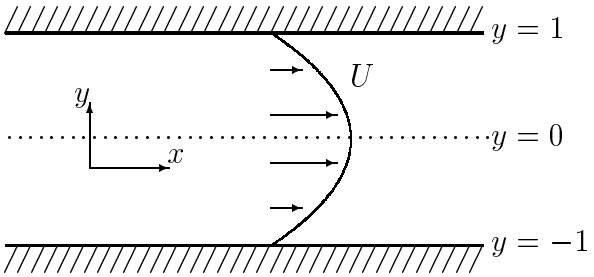

Figure 2.1: Flow geometry

$$\overset{\nabla}{\boldsymbol{A}} = -\frac{1}{\tau(\dot{\gamma})}(\boldsymbol{A} - \boldsymbol{I}) \tag{2.4}$$

$$\dot{\gamma} = \sqrt{2\boldsymbol{E} : \boldsymbol{E}}. \tag{2.5}$$

$\overset{\nabla}{\boldsymbol{A}}$ here is the upper-convected derivative, as defined in section 1.3.3.

There are four parameters: τ, W, C and μ, representing respectively: a relaxation time *function*, relaxation time, concentration of polymer and the solvent viscosity. We then have several possible choices:

a. The Oldroyd-B equation (section 1.3.3) is given by taking $\mu = 1$, $\tau =$ constant $= W$.

b. The UCM equation is $\mu = 0$, $C = 1$, $\tau =$ constant $= W$.

We may also define multicomponent Oldroyd-B fluids in which either C or W is not a constant but a material function, *i.e.* a function of the Lagrangian variable $\boldsymbol{\eta}(\boldsymbol{x}, t)$ that labels each material point. Because $\boldsymbol{\eta}$ is a material property:

$$\frac{D\boldsymbol{\eta}}{Dt} = 0. \tag{2.6}$$

In this case we will have the additional equation $DC/Dt = 0$ or $DW/Dt = 0$. In investigating the stability of a steady planar channel flow, this description may be simplified by identifying each material point by its position $y = \eta$ in the absence of any perturbation.

For either of these fluids we fix $\tau = W$, independent of $\dot{\gamma}$, and, except for a multicomponent UCM fluid, $\mu = 1$.

c. The White-Metzner fluid (section 1.3.9) is $\mu = 0$, $C = 1$, and $\tau(\dot{\gamma})$ any function. In order to be definite (and to have an analytic base state solution from which to start), we limit ourselves initially to a simple power-law form of shear-thinning: $\tau(\dot{\gamma}) = W\dot{\gamma}^{n-1}$. Note that the limiting case $n = 1$ returns us to the UCM fluid.

2.4 Base solution

By symmetry, we consider only the upper half-channel $0 \leq y \leq 1$, in which we expect $\partial U/\partial y$ to be negative. The nondimensionalisation fixes the driving pressure gradient, P_0. Denoting cross-channel differentiation, that is differentiation with respect to y, by a prime: U', we have the boundary conditions $U(1) = 0$, $U(0) = 1$, and $U'(0) = 0$. The base state quantities become:

$$\boldsymbol{U} = (U(y), 0) \tag{2.7}$$

$$\dot{\gamma}_0 = |U'| = -U' \tag{2.8}$$

$$\tau_0 = \tau(\dot{\gamma}_0) \tag{2.9}$$

$$\boldsymbol{A} = \begin{pmatrix} 1 + 2(\tau_0 U')^2 & \tau_0 U' \\ \tau_0 U' & 1 \end{pmatrix} \tag{2.10}$$

$$P = P_\infty + C/W + P_0 x \tag{2.11}$$

$$\boldsymbol{\Sigma} = \begin{pmatrix} -P_\infty - P_0 x + 2C(\tau_0 U')^2/W & P_0 y \\ P_0 y & -P_\infty - P_0 x \end{pmatrix} \tag{2.12}$$

and finally:

$$(\mu + C\tau_0/W)U' = P_0 y. \tag{2.13}$$

For the given geometry and boundary conditions, we find in particular that if $\tau = W$ then:

$$P_0 = \frac{-1}{\int_0^1 \eta/(\mu + C) d\eta} \tag{2.14}$$

so for the Oldroyd-B fluid:

$$P_0 = -2(\mu + C) \quad \text{and} \quad U = 1 - y^2 \tag{2.15}$$

and for the power-law form of the White-Metzner fluid:

$$P_0 = -\left(\tfrac{n+1}{n}\right)^n \quad \text{and} \quad U = 1 - y^{(n+1)/n}. \tag{2.16}$$

The UCM fluid is the combination of both these limits: $\tau = W$ ($n = 1$), $\mu = 0$ and $C = 1$. We note that the limits commute to give $P_0 = -2$ either from equation (2.15) or equation (2.16).

The typical velocity profile $U = 1 - y^2$ is shown on the diagram in figure 2.1.

2.5 Linear stability

We use the method of normal modes to find the temporal stability of a given flow. There is a (nonlinear) system of equations of motion and boundary conditions, for which one simple solution (the given flow) is known:

$$\mathcal{N}(U) = 0. \tag{2.17}$$

This simple solution has been shown for the slit geometry and a selection of constitutive equations in sections 2.3 and 2.4.

We impose an infinitesimal perturbation having magnitude $\epsilon \ll 1$ on this base solution and linearise about the base state:

$$\mathcal{N}(U + \epsilon\phi) = \mathcal{N}(U) + \epsilon\mathcal{L}_U(\partial_x, \partial_y, \partial_t; x, y, t)\phi + O(\epsilon^2) \tag{2.18}$$

so that at leading order in ϵ:

$$\mathcal{L}_U(\partial_x, \partial_y, \partial_t; x, y, t)\phi = 0 \tag{2.19}$$

where $\mathcal{L}_U$ is a linear operator on ϕ. Because our basic solution $U = U(y)$ depends only on one variable, y, we have:

$$\mathcal{L}_U(\partial_x, \partial_y, \partial_t; x, y, t) = \mathcal{L}_U(\partial_x, \partial_y, \partial_t; y). \tag{2.20}$$

Boundary conditions permitting, Fourier theory allows us to transform all possible solutions ϕ in the x-direction (along the channel) and in time:

$$u(k, y, \omega) = \frac{1}{2\pi}\int_{-\infty}^{\infty}\int_{-\infty}^{\infty}\phi(x, y, t)e^{-ikx+i\omega t}dxdt \tag{2.21}$$

with the inversion:

$$\phi(x, y, t) = \frac{1}{2\pi}\int_{-\infty}^{\infty}\int_{-\infty}^{\infty}u(k, y, \omega)e^{ikx-i\omega t}dkd\omega. \tag{2.22}$$

Now equation (2.19) is equivalent to:

$$\int_{-\infty}^{\infty}\int_{-\infty}^{\infty} \mathcal{L}_U(\partial_x, \partial_y, \partial_t; y)\left[u(k,y,\omega)e^{ikx-i\omega t}\right] dkd\omega = 0 \tag{2.23}$$

in which we have used the linearity of $\mathcal{L}_U$ to change the orders of operations. We deduce that:

$$\mathcal{L}_U(\partial_x, \partial_y, \partial_t; y)\left[u(k,y,\omega)e^{ikx-i\omega t}\right] = 0. \tag{2.24}$$

Now we simplify using:

$$\partial_x\left[u(k,y,\omega)e^{ikx-i\omega t}\right] = iku e^{ikx-i\omega t} \tag{2.25}$$

$$\partial_t\left[u(k,y,\omega)e^{ikx-i\omega t}\right] = -i\omega u e^{ikx-i\omega t} \tag{2.26}$$

and equation (2.24) becomes an ordinary differential equation (ODE) for u as a function of y, with k and ω as parameters:

$$\mathcal{L}_U(ik, d/dy, -i\omega; y)u(y) = 0. \tag{2.27}$$

In the channel geometry, there are two zero boundary conditions on $U+\epsilon\phi$ at each wall: slip velocity and penetration velocity. Now because these are both dependent only on y, they may be expressed as $\phi(1) = 0$ and $\phi(-1) = 0$ for the two velocity components of ϕ. Referring back to equation (2.21) immediately gives $u(1) = u(-1) = 0$ for the velocity components of u. This gives us a total of four zero boundary conditions on u. For a fourth order differential operator $\mathcal{L}_U$, this system will be overdetermined for specified k and ω, and therefore nontrivial solutions only exist for certain pairs (ω, k).

2.5.1 Temporal stability

There are two standard ways to proceed with this eigenvalue problem: temporal and spatial stability.

Spatial stability analysis is the equivalent of imposing a disturbance upstream at a fixed frequency, and watching its evolution as it moves downstream to see whether it grows. This is achieved by fixing a real value of ω, the frequency, and solving for complex k. If $Im(k)$ is negative, then the exponential term of equation (2.24) will grow in space and the flow is unstable. In temporal stability analysis, the flow is given a disturbance of fixed wavenumber (real k) and its growth in time is found from the complex value of ω.

The spatial method depends on a disturbance which continues through time, whereas for temporal stability an instantaneous disturbance is needed, but throughout the whole channel. In reality, the most likely disturbances are localised in both space and time, so the choice of method is somewhat arbitrary.

Here we use temporal analysis, the more common method in the existing literature, which is usually easier, so the eigenvalue system is expressed as $\omega = \omega(k)$. This expression is the *dispersion relation*, and using it we specify real k to form an eigenvalue problem for complex ω. If the imaginary part of ω is positive for any k, then the base flow is unstable.

2.5.2 Weakly nonlinear stability

The next step in the process of calculating stability would be weakly nonlinear

theory, in which the next term is included in the Taylor expansion given at the beginning of section 2.5:

$$\mathcal{N}(U+\epsilon\phi) = \mathcal{N}(U) + \epsilon\mathcal{L}_U\phi + \epsilon^2\mathcal{N}_U\phi + O(\epsilon^3). \tag{2.28}$$

Given a solution to the linear problem, ϕ_0, with eigenvalue ω_0, information about its nonlinear evolution may be deduced:

$$\mathcal{N}(U+\epsilon\phi_0) = \epsilon^2\mathcal{N}_U\phi_0 + O(\epsilon^3) \tag{2.29}$$

where $\mathcal{N}_U$ is a quadratic operator. This can give us an evolution equation for the amplitude of ϕ, and near a bifurcation point (marginally stable) can yield information about stable solutions close to our unstable base state.

However, a weakly nonlinear study is difficult unless the linear problem is soluble analytically. In this dissertation we limit ourselves to the linear stability problem. This will give conditions for instability, but we will not be able to predict the form of disturbance seen in experiments.

2.6 Perturbation equations for channel flow

We denote perturbation quantities by either lower case letters ($A+a$, $\Sigma+\sigma$, $W+\varpi$ etc.) or subscripts 1 ($\tau_0+\tau_1$, $\dot{\gamma}_0+\dot{\gamma}_1$).

Conservation of mass, $\boldsymbol{\nabla}.\boldsymbol{u} = 0$, becomes:

$$iku + v' = 0 \tag{2.30}$$

and we use a streamfunction $\psi(y)$ such that:

$$u = \psi' \quad \text{and} \quad v = -ik\psi \tag{2.31}$$

to satisfy this automatically.

The perturbation momentum equation becomes:

$$ik\sigma_{11} + \sigma'_{12} = 0 \tag{2.32}$$

$$ik\sigma_{12} + \sigma'_{22} = 0. \tag{2.33}$$

The perturbation evolution equations give:

$$\sigma_{11} = -p + 2ik\mu\psi' + \frac{C}{W}a_{11} + \frac{c}{W}A_{11} - \frac{C\varpi}{W^2}A_{11} \tag{2.34}$$

$$\sigma_{12} = \mu(\psi'' + k^2\psi) + \frac{C}{W}a_{12} + \frac{c}{W}A_{12} - \frac{C\varpi}{W^2}A_{12} \tag{2.35}$$

$$\sigma_{22} = -p - 2ik\mu\psi' + \frac{C}{W}a_{22} + \frac{c}{W} - \frac{C\varpi}{W^2} \tag{2.36}$$

$$\left(-i\omega + ikU + \frac{1}{\tau_0}\right) a_{11} = ik\psi A'_{11} + 2A_{12}\psi'' + 2A_{11}ik\psi' + 2U'a_{12} + \frac{\tau_1}{\tau_0^2}(A_{11} - 1) \tag{2.37}$$

$$\left(-i\omega + ikU + \frac{1}{\tau_0}\right) a_{12} = ik\psi A'_{12} + \psi'' + A_{11}k^2\psi + U'a_{22} + \frac{\tau_1}{\tau_0^2}A_{12} \tag{2.38}$$

$$\left(-i\omega + ikU + \frac{1}{\tau_0}\right) a_{22} = -2ik\psi' + 2A_{12}k^2\psi. \tag{2.39}$$

In addition, because C and W are material quantities:

$$D(C + c)/Dt = D(W + \varpi)/Dt = 0. \tag{2.40}$$

It is convenient to define the streamline displacement ζ, so that a streamline moves to:

$$y = \eta + \zeta(\eta) \exp(ikx - i\omega t) \tag{2.41}$$

where η is the Lagrangian coordinate describing the streamline. Because the streamline is a material surface, $D\eta/Dt = 0$, and to linear order:

$$\eta = y - \zeta(y) \exp(ikx - i\omega t) \tag{2.42}$$

which gives:

$$\tau_1 = \dot{\gamma}_1(\partial\tau/\partial\dot{\gamma})|_{W,\dot{\gamma}_0} + \varpi(\partial\tau/\partial W)|_{W,\dot{\gamma}_0} \tag{2.43}$$

$$\dot{\gamma}_1 = -(\psi'' + k^2\psi) \tag{2.44}$$

$$c = -\zeta C' \tag{2.45}$$

$$\varpi = -\zeta W' \tag{2.46}$$

$$(-i\omega + ikU)\zeta = -ik\psi. \tag{2.47}$$

The system (2.32) – (2.47) is a fourth-order differential equation for ψ, and so we need four boundary conditions.

The no-slip, no-penetration boundary condition still holds for the perturbation flow (as it did for the base flow), and gives two boundary conditions at $y = 1$:

$$\psi(1) = \psi'(1) = 0. \tag{2.48}$$

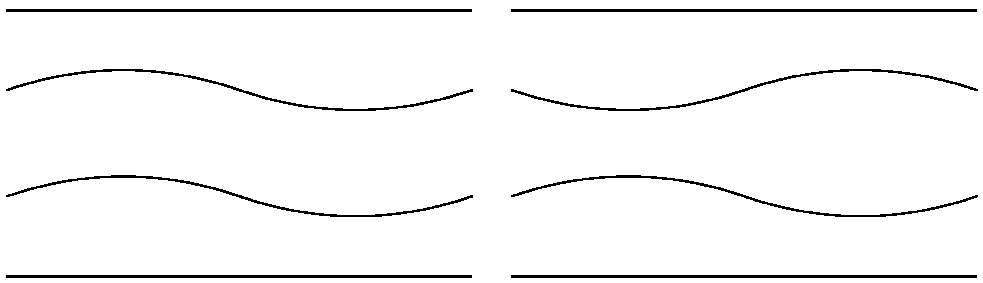

Figure 2.2: Sinuous perturbation (left) and varicose (right)

As we are considering only the upper half-channel, the remaining boundary conditions are to be placed on the centreline $y = 0$. If the perturbation is sinuous, the x-velocity at the centre is unchanged under the transformation $y \to -y$ (and is therefore zero), so ψ must be an even function of y. Alternatively, for a varicose perturbation, there must be no y-velocity on the centreline of the channel, so ψ is odd. Figure 2.2 shows the nature of sinuous and varicose perturbations. We have therefore:

$$\text{Sinuous } \psi'(0) = \psi'''(0) = 0 \tag{2.49s}$$

$$\text{Varicose } \psi(0) = \psi''(0) = 0. \tag{2.49v}$$

Because all these boundary conditions are zero, the condition that we are looking for a nontrivial solution provides the over-determination mentioned in section 2.5. The eigenvalue problem $\omega(k)$ is then defined in general by equations (2.32) – (2.49).

2.7 Alternative form for the equations

A mathematically unfortunate, and, as we shall see later, physically inappropriate feature of the equations in section 2.6 arises in considering cases where

C or W is a material function, so that C' or W' is nonzero. For a natural and important limiting case in which C or W is actually a discontinuous function, the equations above give rise to products of generalised functions, which are awkward to deal with.

Motivated by the physical understanding of the way in which the instability operates (chapter 3) we are led to rewrite the equations.

We divide the stresses, stretches and pressure into two parts: $\sigma = \sigma^{\rm adv} + \sigma^{\rm dyn}$, $a = a^{\rm adv} + a^{\rm dyn}$, $p = p^{\rm adv} + p^{\rm dyn}$, where $x^{\rm adv}$ is the part of quantity X owing to advection of C or W by the streamline displacement alone:

$$x^{\rm adv} = c\,\partial X/\partial C + \varpi\,\partial X/\partial W. \tag{2.50}$$

The advection contributions are then given as:

$$p^{\rm adv} = c/W + \varpi(-C/W^2) \tag{2.51}$$

$$a_{22}^{\rm adv} = 0 \tag{2.52}$$

$$a_{12}^{\rm adv} = c(-WU'/(1+C)) + \varpi U' \tag{2.53}$$

$$a_{11}^{\rm adv} = c(-4W^2(U')^2/(1+C)) + \varpi(4W(U')^2) \tag{2.54}$$

$$\sigma_{22}^{\rm adv} = \sigma_{12}^{\rm adv} = 0 \tag{2.55}$$

$$\sigma_{11}^{\rm adv} = c(2W(U')^2(1-C)/(1+C)) + \varpi(2C(U')^2). \tag{2.56}$$

The remaining dynamic quantities are then driven by these advected perturbations for which the governing equations are known. The momentum equations now become (omitting the superscript $^{\mathrm{dyn}}$):

$$ik\sigma_{11} + \sigma'_{12} = 2ik\zeta P_0^2 y^2 \{CW/(1+C)^2\}' \tag{2.57}$$

$$ik\sigma_{12} + \sigma'_{22} = 0. \tag{2.58}$$

Note the appearance of a 'body force' on the right hand side of equation (2.57) arising from the advection of the base state solutions. The constitutive equations are now:

$$\sigma_{11} = -p + 2ik\psi' + \frac{C}{W}a_{11} \tag{2.59}$$

$$\sigma_{12} = \{\psi'' + \zeta P_0 y((1+C)^{-1})'\} + k^2\psi + \frac{C}{W}a_{12} \tag{2.60}$$

$$\sigma_{22} = -p - 2ik\psi' + \frac{C}{W}a_{22} \tag{2.61}$$

$$\left(-i\omega + ikU + \frac{1}{W}\right) a_{11} = ik\psi\frac{4W^2P_0^2y}{(1+C)^2} + 2A_{12}\{\psi'' + \zeta P_0 y((1+C)^{-1})'\} + 2A_{11}ik\psi' + 2U'a_{12} \tag{2.62}$$

$$\left(-i\omega + ikU + \frac{1}{W}\right) a_{12} = ik\psi\frac{WP_0}{(1+C)} + \{\psi'' + \zeta P_0 y((1+C)^{-1})'\} + A_{11}k^2\psi + U'a_{22} \tag{2.63}$$

$$\left(-i\omega + ikU + \frac{1}{W}\right) a_{22} = -2ik\psi' + 2A_{12}k^2\psi \tag{2.64}$$

and the kinematic condition is:

$$(-i\omega + ikU)\zeta = -ik\psi. \tag{2.65}$$

Equations (2.57) – (2.65) prove to be easier to manipulate than those of section 2.6 because of the limited number of occurrences of derivatives of C and W. Taken together with the unchanged boundary conditions (2.48) – (2.49), they define $\omega(k)$.

We have not made any alteration to the equations in the case in which both C and W are constants but τ is a function of $\dot{\gamma}$. This is because the perturbation to τ:

$$\tau_1 = -(\psi'' + k^2\psi)(\partial\tau/\partial\dot{\gamma})|_{\dot{\gamma}_0} \tag{2.66}$$

does not depend on the streamline displacement, ζ, but rather on the perturbed flow itself. Our simplification was based on the observation that part of the perturbation was due to the advection of base state quantities by the streamline displacement. Where this advection does not occur, there is no such simplification.

2.8 Existence of roots

The linear equations we have defined for the perturbation may be combined to give a single fourth-order differential equation for ψ. Where the equations are regular, a small change in k will cause only a small change in ψ and in ω. Therefore, for most of parameter space, a root which has been found for some real k may be analytically continued to higher and lower values of k.

The exceptions to this principle arise at singularities of the system. When the coefficient of the highest derivative is zero, roots may appear or disappear. For instance, in the Oldroyd-B fluid (as described in section 2.6), the highest derivative is multiplied by the term $-i\omega+ikU+1/W$, so there is a continuous spectrum, a line of stable roots, at $\omega = kU - i/W$, setting this term equal to zero. The eigenmodes corresponding to this spectrum are a set of delta-functions across the channel:

$$\{\omega = kU(y_0) - i/W; \psi = \delta(y - y_0)\}. \tag{2.67}$$

We are not interested here in the continuous spectrum as such, but in its effect on the discrete spectrum. Discrete roots (with eigenfunctions which are regular functions) may disappear (while moving in k-space) by merging into the continuous spectrum.

Other instances of singular equations may occur if $\omega = kU$ or if $n = 0$ for a White-Metzner fluid.

2.9 Numerical method

It is generally necessary to solve these equations numerically. The method used follows Ho & Denn [80].

For each prescribed k, an estimated value of ω is chosen, based on asymptotic limits and parameter continuation. Using this guess, we have a fourth-order differential equation for ψ, with four boundary conditions.

Let us suppose we are looking for a sinuous eigenmode. Then the bound-

ary conditions are:

$$\psi'(0) = \psi'''(0) = 0 \tag{2.68}$$

$$\psi(1) = \psi'(1) = 0. \tag{2.69}$$

Since the system of equations is linear, any solution is specified by the values of ψ and its derivatives at the centre-line:

$$\mathbf{\Psi} = (\psi(0), \psi'(0), \psi''(0), \psi'''(0)). \tag{2.70}$$

Therefore, any solution to condition (2.68) must be a linear combination of the two functions, ψ_1 and ψ_2, whose 'fingerprints' are:

$$\mathbf{\Psi}_1 = (1, 0, 0, 0) \tag{2.71}$$

and:

$$\mathbf{\Psi}_2 = (0, 0, 1, 0). \tag{2.72}$$

If ω is the true value, then there exists some linear combination of ψ_1 and ψ_2 for which the two wall boundary conditions (2.69) are satisfied:

$$\begin{vmatrix} \psi_1(1) & \psi_1'(1) \\ \psi_2(1) & \psi_2'(1) \end{vmatrix} = 0 \tag{2.73}$$

where $|...|$ denotes the determinant.

The numerical method consists of integrating the two basis functions ψ_1 and ψ_2 numerically (by a fourth-order adaptive Runge-Kutta-Merson method, provided by the Numerical Algorithms Group (NAG)) from 0 to 1

across the channel. This finds the determinant above, and then the Newton-Raphson method is used to find a zero of this determinant as a function of ω.

The integration routine also involves renormalisation of the two basis vectors at several stations across the channel. If there is one vector which is growing exponentially as it moves across the channel, and the other decays (or grows more slowly), then small numerical errors will cause both vectors to 'tilt' in their vector space towards the growing mode, and to grow with it. For large values of the exponent (which occur for high k or large W) this parallelisation of the eigenfunctions can cause the appearance of spurious roots. Therefore, periodically the vectors are orthonormalised by a Gram-Schmidt procedure:

$$\begin{aligned} \boldsymbol{a}_{new} &= \boldsymbol{a}/|\boldsymbol{a}| \\ \boldsymbol{b}_{int} &= \boldsymbol{b} - (\boldsymbol{a}_{new}.\boldsymbol{b})\boldsymbol{a}_{new} \\ \boldsymbol{b}_{new} &= \boldsymbol{b}_{int}/|\boldsymbol{b}_{int}| \end{aligned} \tag{2.74}$$

where $\boldsymbol{a}.\boldsymbol{b} = \sum a_i \overline{b}_i$ and $|\boldsymbol{a}| = \sqrt{\boldsymbol{a}.\boldsymbol{a}}$. Even with this procedure in place, there are some regions of parameter space where numerical solution is not an option. For example, very close to the singular limit of the White-Metzner equations, $n = 0$, the problem is extremely stiff and tiny errors grow out of control as the integration progresses. In regions such as this, precautions have to be taken against spurious results caused by numerical errors. It is sensible to change numerical parameters (such as the number of renormalisations, the size of the maximum error allowed from the integration routine, or the small value at which the determinant is deemed to be 'zero') and check that the roots do not change. Roots of the analytic problem should be insensitive to

these numerical parameters, which distinguishes them from solutions to the numerical problem which are not true roots of the original analytic problem.

The code is checked against published results in specific cases (Oldroyd-B and UCM) and against asymptotic limits. To find a single value of ω where the parameters are all of moderate size takes three to four seconds on a machine with Specfp95 5.78. However, if the parameter values are extreme and the problem is nearly singular (for example, if $n \ll 1$ in the system of chapter 6), a single function evaluation can take around five minutes.

Chapter 3

Coextrusion Instability of Fluids having Matched Viscosities but Discontinuous Normal Stresses

3.1 Introduction

We consider in this chapter the coextrusion of two elastic liquids in a channel. Our principal aim is to identify the physical processes which generate and inhibit instability of the interface between the fluids. The bulk of the work in this chapter has been published in the *Journal of Non-Newtonian Fluid Mechanics* [218].

When there is a jump in viscosity, and the Reynolds number is nonzero, an instability is present even for Newtonian liquids (Yih [221]). We therefore isolate the central non-Newtonian aspect by considering a case where viscosity varies continuously across the interface, and only normal stress jumps. This leads us to use the constant-viscosity Oldroyd-B model. Additionally we restrict attention here to the simplest case where inertia is negligible. We also neglect surface tension at the interface between the two fluids (but section 3.6 contains a discussion of the importance of surface tension).

For long wavelength disturbances Hinch *et al* [79] provide a mechanism for, and calculation of, the growth of disturbances resulting from normal stress. This mechanism operates only when the coating is more elastic than the core, and has zero growth rate as the wavelength tends to infinity.

In the short-wave limit, Chen & Joseph [37] found a new instability (for UCM fluids) whose growth rate is finite, in contrast to the long-wave mode.

In order to understand the mechanisms of instability, we extend these analyses to find the influence of solvent viscosity (absent for the UCM fluid) and of wavelength, where this is moderate. In later chapters, we will consider these mechanisms as possible destabilisers of the flow of a single continuously stratified fluid.

We shall find, in the absence of surface tension, that:

- interfaces between different Oldroyd-B fluids are unstable to short-wave disturbances except at high concentration and high elasticity
- the growth rate becomes independent of wavelength in this limit
- the symmetry of the disturbance (whether varicose or sinuous, whether planar or axisymmetric) is irrelevant to the mechanism at work.

The central conclusion from our analysis is therefore that surface tension must be sufficiently large if elastic interface disturbances are to be damped. We examine the importance of surface tension effects in section 3.6.

Related theoretical work on this phenomenon was performed by Su and Khomami in 1992, who studied, analytically and numerically, the stability of two-layer die flow [194, 193], Renardy in 1988, who tackled the short-wave behaviour of two-layer Couette flow [174], and Chen, also in 1992 [37], who found a short-wave instability in core-annular flow. More recently, Laure *et al* [117] have studied two- and three-layer Poiseuille flow of Oldroyd-B fluids with long to moderate wavelength perturbations, incorporating the effects of surface tension, viscosity stratification, density stratification and inertia.

We formulate the problem for arbitrary interface disturbances in section 3.2, which provides a numerical problem against which our asymptotics can later be tested. The asymptotic limit of long waves is explained in section 3.3. Within the short-wave limit, asymptotic limits of dilute and concentrated solutions and high and low relative elasticity are identified in section 3.4. Conclusions are given in section 3.6.

3.2 Statement of the problem

The basic geometry is a planar channel flow, sketched in figure 3.1, with different Oldroyd-B fluids occupying the regions $\kappa < |y| < 1$, $|y| < \kappa$ respectively.

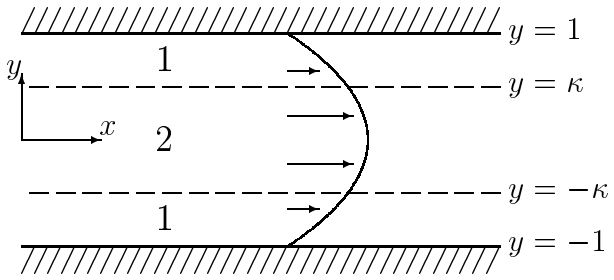

Figure 3.1: Flow geometry

We suppose that both fluids have the same (constant) shear viscosity, but different normal stress coefficients.

Inertia is neglected, as is surface tension at the interface between the two fluids. The nondimensional groups that remain are then:

κ the relative width of the inner fluid

C the ratio of the elastic zero-shear viscosity contribution to the solvent contribution; the concentration of polymer

W the Weissenberg number; the ratio of fluid relaxation time to a typical flow time.

We require that the concentration parameter, C, should be matched in the two fluids, so that each has the same shear viscosity, $1 + C$. The two fluids

may have different Weissenberg numbers. We call these W_1 and W_2. If $W_1 = W_2$ there is effectively only one fluid present.

3.2.1 Base state

We use a standard Oldroyd-B equation within each fluid, which, in the notation of chapter 2, is given by $\tau = W$, $\mu = 1$, $C' = W' = 0$. Thus the base state becomes Poiseuille flow:

$$\boldsymbol{U} = (1 - y^2, 0) \tag{3.1}$$

$$\boldsymbol{A} = \begin{pmatrix} 1 + 8W^2y^2 & -2Wy \\ -2Wy & 1 \end{pmatrix} \tag{3.2}$$

$$P = P_\infty + C/W - 2(1 + C)x \tag{3.3}$$

$$\boldsymbol{\Sigma} = \begin{pmatrix} -P_\infty + 2(1 + C)x + 8CWy^2 & -2(1 + C)y \\ -2(1 + C)y & -P_\infty + 2(1 + C)x \end{pmatrix}. \tag{3.4}$$

Because we are using the same value of C within each fluid, but different values of W, $\boldsymbol{\Sigma}_{11}$ has a discontinuity of magnitude $8cy^2\Delta W$ at each interface, resulting from the quadratic growth in normal stress with shear-rate for Oldroyd-B fluids. This jump is permissible only because the interfaces are parallel to the x-axis.

The fundamental mechanism of the elastic instability (as shown in [79]) is that the tilting of this interface exposes the jump in $\boldsymbol{\Sigma}_{11}$ and this drives a perturbation flow which may in its turn cause the perturbation to grow.

3.2.2 Perturbation equations

The perturbation equations within each fluid are:

$$ik\sigma_{11} + \sigma'_{12} = 0 \tag{3.5}$$

$$ik\sigma_{12} + \sigma'_{22} = 0 \tag{3.6}$$

$$\sigma_{11} = -p + 2ik\psi' + \frac{C}{W}a_{11} \tag{3.7}$$

$$\sigma_{12} = (\psi'' + k^2\psi) + \frac{C}{W}a_{12} \tag{3.8}$$

$$\sigma_{22} = -p - 2ik\psi' + \frac{C}{W}a_{22} \tag{3.9}$$

$$\left(-i\omega + ikU + \frac{1}{W}\right) a_{11} = ik\psi A'_{11} + 2A_{12}\psi'' + 2A_{11}ik\psi' - 4ya_{12} \tag{3.10}$$

$$\left(-i\omega + ikU + \frac{1}{W}\right) a_{12} = ik\psi A'_{12} + \psi'' + A_{11}k^2\psi - 2ya_{22} \tag{3.11}$$

$$\left(-i\omega + ikU + \frac{1}{W}\right) a_{22} = -2ik\psi' + 2A_{12}k^2\psi. \tag{3.12}$$

We have boundary conditions at the wall and centreline of the channel:

$$\psi(1) = \psi'(1) = 0 \tag{3.13}$$

$$\text{Sinuous } \psi'(0) = \psi'''(0) = 0 \tag{3.14s}$$

$$\text{Varicose } \psi(0) = \psi''(0) = 0. \tag{3.14v}$$

At the interface $y = \kappa + \zeta \exp(ikx - i\omega t)$ we require continuity of $\boldsymbol{U} + \boldsymbol{u}$ and of the traction $(\boldsymbol{\Sigma} + \boldsymbol{\sigma}).\boldsymbol{n}$. These conditions become continuity of ψ, ψ', $\sigma_{12} - ik\zeta\Sigma_{11}$ and σ_{22}.

Substituting the base state quantities into the equations of section 3.2.1 and denoting differentiation with respect to y by D, we obtain:

$$(D^2 - k^2)^2\psi + \frac{C}{W}(D^2 + k^2)a_{12} + ik\frac{C}{W}D(a_{11} - a_{22}) = 0 \tag{3.15}$$

$$\left(-i\omega + ik(1 - y^2) + \frac{1}{W}\right) a_{11} = 16ikW^2y\psi + 2ik(1 + 8W^2y^2)D\psi - 4WyD^2\psi - 4ya_{12} \tag{3.16}$$

$$\left(-i\omega + ik(1 - y^2) + \frac{1}{W}\right) a_{12} = -2ikW\psi + k^2(1 + 8W^2y^2)\psi + D^2\psi - 2ya_{22} \tag{3.17}$$

$$\left(-i\omega + ik(1 - y^2) + \frac{1}{W}\right) a_{22} = -4k^2Wy\psi - 2ikD\psi. \tag{3.18}$$

Equation (3.15) here is the vorticity equation, and (3.16) – (3.18) arise from the evolution of $\boldsymbol{A}$.

The boundary conditions are:

$$\text{Sinuous } D\psi(0) = D^3\psi(0) = 0 \tag{3.19s}$$

$$\text{Varicose } \quad \psi(0) = D^2\psi(0) = 0. \tag{3.19v}$$

$$\psi(1) = D\psi(1) = 0 \tag{3.20}$$

$$\left[(D^2 + k^2)\psi + \frac{C}{W}a_{12} - 8ikC\kappa^2W\zeta\right] = 0 \tag{3.21}$$

$$\left[D(D^2 - 3k^2)\psi + \frac{C}{W} D a_{12} + ik\frac{C}{W}(a_{11} - a_{22}) \right] = 0 \qquad (3.22)$$

where the square brackets denote a jump across $y = \kappa$.

We have, finally, a kinematic boundary condition stating that the interface is a material surface:

$$(-i\omega + ik(1 - \kappa^2))\zeta = -ik\psi(\kappa). \qquad (3.23)$$

As it stands, the problem above is not amenable to analytic solution, because of the explicit y-dependence of the coefficients in equations (3.16) to (3.18). So, in order to investigate the behaviour of $\omega(k)$ in the various regions of parameter space, we first look at the extreme values and identify physical mechanisms.

3.3 The long-wave limit, $k \to 0$

The long-wave limit, $k \to 0$, was first studied in this geometry by Chen [33]. Hinch *et al* [79] found the leading-order behaviour for general constant viscosity non-Newtonian fluids. For the Oldroyd-B fluid in particular, the problem can be posed as a regular asymptotic expansion in k. We anticipate that the frequency of the disturbance will have the form:

$$\omega = ku + i\sigma k^2 \qquad (3.24)$$

where $u = 1 - \kappa^2$ is the velocity of the interface, and thus the Deborah number, $\omega\tau$, associated with the perturbation is proportional to k and so is small. In other words, the perturbation elastic stresses respond quasi-statically to

the flow, and give rise to a Newtonian stress having shear viscosity $1 + C$ within each fluid.

Because the disturbance wavelength is much longer that the channel width, the leading order perturbation flow is in the x-direction, the pressure across the channel is uniform, and so the flow profile is linear for a sinuous mode and quadratic if the mode is varicose.

The velocity must be continuous across $y = \kappa$, and the tangential stress balance across the interface gives:

$$[(1 + C)u']_{\kappa_-}^{\kappa+} = [\sigma_{12}] = 8ikC\kappa^2\zeta[W]. \tag{3.25}$$

For a sinuous mode (sketches of sinuous and varicose perturbations are shown in figure 2.2 on page 72), the pressure gradient must be an odd function and is thus zero across the channel. We then obtain:

$$u(y) = \frac{[\sigma_{12}]}{1 + C} \begin{cases} -(1 - \kappa)y & 0 < y < \kappa \\ -\kappa(1 - y) & \kappa < y < 1 \end{cases} \tag{3.26}$$

and mass conservation gives the streamfunction ψ at the interface as:

$$\psi(\kappa) = -\int_\kappa^1 u \; dy = \frac{[\sigma_{12}] f_s(\kappa)}{2(1 + C)} \tag{3.27}$$

where

$$f_s(\kappa) = \kappa(1 - \kappa)^2. \tag{3.28}$$

For a varicose mode the perturbation pressure gradient along the channel must be such as to make the perturbation volume flux along the channel

vanish. After some algebra, we thus obtain:

$$u(y) = \frac{[\sigma_{12}]}{1+C} \begin{cases} -\frac{1}{4}(1-\kappa)(1-3\kappa) - \frac{3}{4}(1-\kappa)(1+\kappa)y^2 & 0 < y < \kappa \\ \frac{1}{2}(3\kappa^2-1)(y-1) - \frac{3}{4}(1-\kappa)(1+\kappa)(y-1)^2 & \kappa < y < 1 \end{cases} \tag{3.29}$$

and:

$$\psi(\kappa) = \frac{[\sigma_{12}] f_v(\kappa)}{2(1+C)} \tag{3.30}$$

where:

$$f_v(\kappa) = \tfrac{1}{2}\kappa(1-\kappa)^2(\kappa^2+2\kappa-1). \tag{3.31}$$

Since our eigenvalue condition is:

$$\omega - k(1-\kappa^2) = k\psi(\kappa)/\zeta \tag{3.32}$$

we deduce:

$$\omega = (1-\kappa^2)k + 4i\tfrac{C}{(1+C)}(W_1 - W_2)\kappa^2 f(\kappa)k^2 + O(k^3). \tag{3.33}$$

The leading-order term is the convection rate at the undisturbed interface, which indicates that the dynamics is based at the interface. The leading-order growth rate of the instability is:

$$\sigma \sim 4\tfrac{C}{(1+C)}(W_1 - W_2)\kappa^2 f(\kappa)k^2. \tag{3.34}$$

Since $f_s(\kappa) > 0$ for all $0 < \kappa < 1$, this gives instability to sinuous modes if and only if $W_1 > W_2$, *i.e.* if the outer fluid is the more elastic (relaxes more slowly). Varicose modes are unstable where $(W_1 - W_2)f_v(\kappa) > 0$, *i.e.* where either $W_1 > W_2$ and $\kappa > \sqrt{2} - 1$ or $W_1 < W_2$ and $\kappa < \sqrt{2} - 1$.

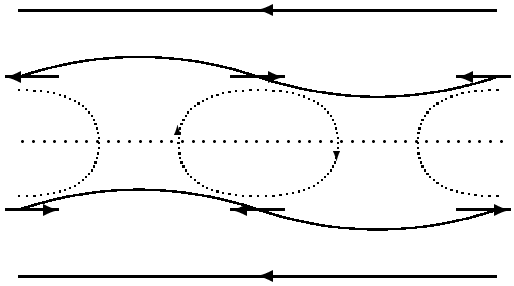

Figure 3.2: Representation of the mechanism of the long-wave sinuous interfacial instability. The diagram is fixed in the frame of reference for which the disturbance is stationary, so the walls are moving from right to left.

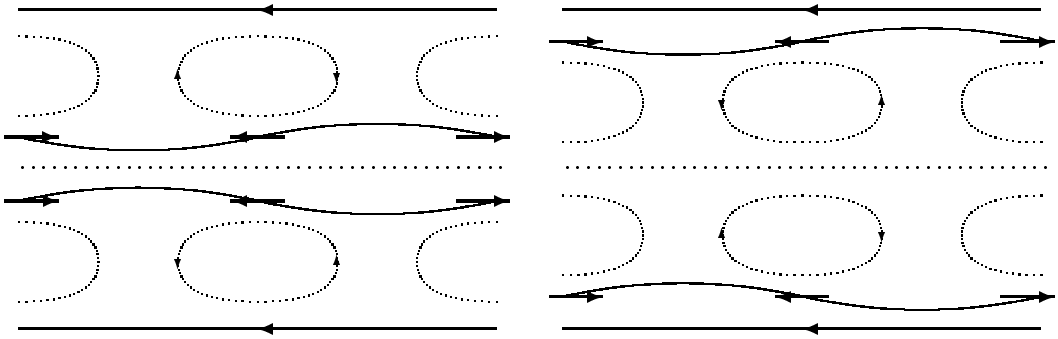

Figure 3.3: Representation of the mechanism of the long-wave varicose interfacial instability. Stable modes are on the left, unstable on the right. The diagram is fixed in the frame of reference for which the disturbance is stationary, so the walls are moving from right to left.

The mechanism of the instability is as follows (illustrated in figures 3.2 and 3.3):

Let us suppose that $W_1 > W_2$ (*i.e.* the more elastic fluid is on the outside). The tilt in the interface, caused by the imposed perturbation, exposes the jump in Σ_{11}. In order to balance this stress jump, the fluid responds by flowing in the directions shown by the arrows.

Incompressibility then requires that the flow conserve mass, which it does by recirculating, as shown in dotted lines. In the sinuous case (figure 3.2) there is one eddy across the whole channel, which enhances the streamline perturbation. In the varicose case (figure 3.3), the symmetry leads to one eddy in each half of the channel. If the inner fluid occupies a large enough fraction of the cross-section ($\kappa > \sqrt{2} - 1$), this eddy will occur within the inner fluid, thus destabilising the interface; otherwise the eddy is close to the wall and the interface is stable.

If $W_1 < W_2$ then all these perturbation flows (and therefore the stability of the base state) are reversed.

Note that the growth rate of the instability tends to zero like k^2, so the very long-wave limit $k = 0$ is neutrally stable for all Weissenberg numbers.

3.4 The short-wave limit, $k \to \infty$

This limit was first considered by Chen & Joseph [37].

The Oldroyd-B fluid has no intrinsic lengthscale. Thus in the short-wave limit the wavelength k^{-1} becomes the only lengthscale defining the flow. At leading order as $k \to \infty$ the perturbation is confined within $O(k^{-1})$ of the interface. So the walls of the channel, the perturbation of the other interface and the variation in base shear-rate with y have no effect. The results therefore apply to any interface (without surface tension): there is no distinction here between sinuous or varicose, planar or axisymmetric disturbances, all of which have the same growth rate.

If we move to a frame of reference travelling with the interface (*i.e.* at

speed $1-\kappa^2$), move the level $y=0$ to the interface, and rescale all lengths with k, we obtain, at leading order, the equations for a perturbation to unbounded simple shear flow of two fluids, having a *constant* shear-rate -2κ (figure 3.4):

$$(D^2-1)^2\psi + \frac{C}{W}(D^2+1)a_{12} + i\frac{C}{W}D(a_{11}-a_{22}) = 0 \tag{3.35}$$

$$\left(-i\omega - 2i\kappa y + \frac{1}{W}\right)a_{11} = 2i(1+8W^2\kappa^2)D\psi - 4W\kappa D^2\psi - 4\kappa a_{12} \tag{3.36}$$

$$\left(-i\omega - 2i\kappa y + \frac{1}{W}\right)a_{12} = (1+8W^2\kappa^2)\psi + D^2\psi - 2\kappa a_{22} \tag{3.37}$$

$$\left(-i\omega - 2i\kappa y + \frac{1}{W}\right)a_{22} = -4W\kappa\psi - 2iD\psi. \tag{3.38}$$

The following functions must be continuous at the interface $y=0$:

$$\psi \quad D\psi \tag{3.39}$$

$$(D^2+1)\psi + \frac{C}{W}a_{12} - 8iC\kappa^2\zeta W \tag{3.40}$$

$$\text{and } D(D^2-3)\psi + \frac{C}{W}Da_{12} + i\frac{C}{W}(a_{11}-a_{22}) \tag{3.41}$$

and the kinematic condition reduces to:

$$\omega\zeta = \psi(0) \tag{3.42}$$

while the perturbation decays away from the interface:

$$\psi(y) \to 0 \text{ as } y \to \pm\infty. \tag{3.43}$$

We note that k has disappeared from the problem and thus this set of equations gives instability at a growth rate that is constant as $k \to \infty$. The symmetry of the unbounded system means that exchanging W_1 and W_2 is equivalent to reversing the direction of shear, which reverses the convective part of ω but does not change the growth rate.

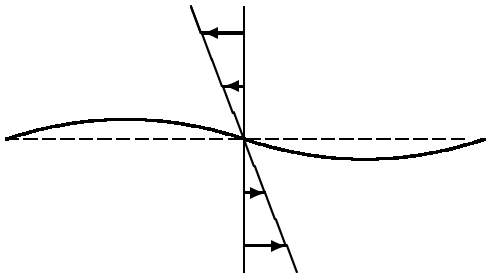

Figure 3.4: Unbounded Couette flow of two fluids

Note that neither ω nor any of the dimensionless fluid parameters C, W_1 and W_2 has been rescaled in this reformulation; ω here is the same as in section 3.2.2 except for the subtraction of a term, $(1-\kappa^2)k$, inherent in the change of frame of reference.

3.4.1 The effect of layer thickness on short waves

Thin inner fluid layer, $\kappa \to 0$

The driving term for the instability derives from the jump in the base state normal stress, *i.e.* the final term in equation (3.21), $8ikC\kappa^2[W]\zeta$, or equivalently $2ikC\dot{\gamma}^2[W]\zeta$ where $\dot{\gamma} = 2\kappa$ is the shear-rate at the interface. For a very narrow inner fluid layer, this shear-rate is very small so any destabilising effect is small also.

We take $k\kappa$ to be an order 1 quantity, *i.e.* we are able to consider waves having length $k^{-1} \leq \kappa$. One consequence of this is that we may not neglect the effect of the presence of the centreline: so we consider a flow in which only the outer fluid is unbounded.

The eigenfunction is then an even function of y within the inner fluid (*i.e.* $\psi \sim \cosh(y),\ y\sinh(y)$), and a decaying exponential in the outer fluid.

The eigenvalue at leading order (convecting with the interface) is:

$$\omega = -4i\kappa^2 \tfrac{C}{1+C}(W_1 - W_2)k\kappa e^{-2k\kappa} + O(\kappa^4). \tag{3.44}$$

The growth rate σ of the instability is given by the imaginary part of the eigenvalue:

$$\sigma \sim -4\kappa^2 \tfrac{C}{1+C}(W_1 - W_2)k\kappa e^{-2k\kappa} \tag{3.45}$$

which is positive, indicating instability, if the inner fluid is more elastic ($W_2 > W_1$). Where σ is negative, the flow is stable to perturbations of this kind in this limit.

In the unstable, case σ has a maximum in $k\kappa$ at $k\kappa \sim \frac{1}{2}$ (figure 3.5). Note that very short waves, $k \to \infty$, do not have the fastest growth rate; rather it is at $k \sim \kappa^{-1}$.

Thin outer fluid, $\kappa \to 1$

In this limit, the shear-rate remains $O(1)$ and so the equations within the thin fluid are no simpler than those in the bulk of the flow. The leading-order system of equations still cannot be solved analytically.

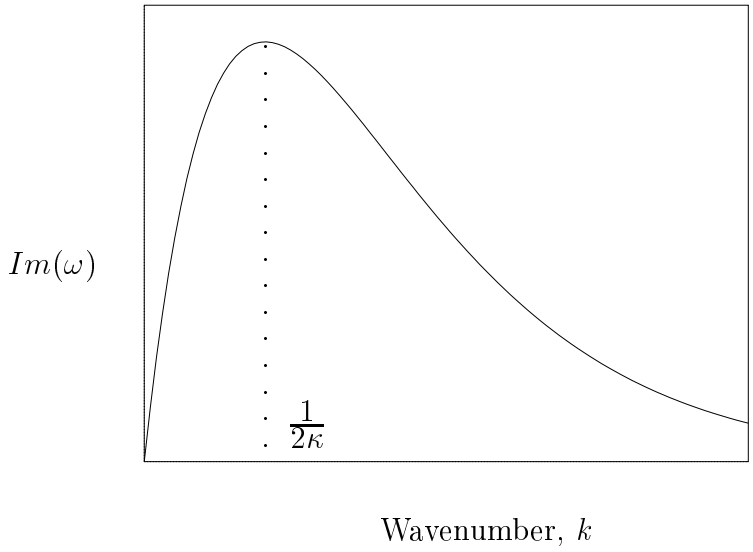

Figure 3.5: Growth rate $\sigma \sim k\kappa \exp(-2k\kappa)$ plotted against wavenumber k for fixed small κ. The function has a maximum at $k = (2\kappa)^{-1}$.

Representative case: $\kappa = 1/2$

For the rest of the study of short waves, since we are interested in unbounded Couette flow, for convenience we put the interface at the representative point $\kappa = \frac{1}{2}$, *i.e.* the shear-rate is -1 at the upper interface. The geometry is simple two-dimensional unbounded shear flow of superposed fluids, with the interface parallel to the direction of flow, as shown in figure 3.4.

Even this reduced problem requires numerical solution (because of the advective terms proportional to y in equations (3.36) – (3.38)), but ω is a function only of C, W_1 and W_2, and the central features may be identified by examining extreme cases.

3.4.2 The effect of polymer concentration on short waves

Concentrated solution, $C \to \infty$, but arbitrary flow strength W

As the concentration parameter C tends to ∞ (or in the notation of chapter 2, $\mu = 0$), the Oldroyd-B fluid effectively loses its solvent contribution giving the Upper-Convected Maxwell fluid (UCM). This fluid was studied in Couette flow by Renardy [174], and the stability problem solved analytically. The neutral stability curves in the W_1-W_2 plane are shown in figure 3.6. We note that the interface is stable if *either* $W_1 = W_2$ *or* W_1 and W_2 are widely different.

Dilute solution, $C \to 0$

In the dilute limit, both fluids are nearly Newtonian. All the perturbation quantities may be expanded as powers of C and the eigenvalue problem solved iteratively using 'Maple' [29]. The eigenvalue is:

$$\omega = -\frac{1}{4}C^2(W_1 - W_2)(W_1 + W_2) + \frac{1}{8}iC^3(W_1 - W_2)(W_1 + W_2) \times (W_1 - W_2 - 4i + 2(W_1 - i)\mathcal{E}(2i/W_1) - 2(W_2 + i)\mathcal{E}(-2i/W_2)) + O(C^4) \quad (3.46)$$

where $\mathcal{E}(x) \equiv \int_0^\infty \frac{e^{-xt}}{1+t}dt$ is the exponential integral function.

We note that the effect of elasticity appears only at order C^3. At leading order in C, this shows neutral stability (as expected) when $W_1 = W_2$, but

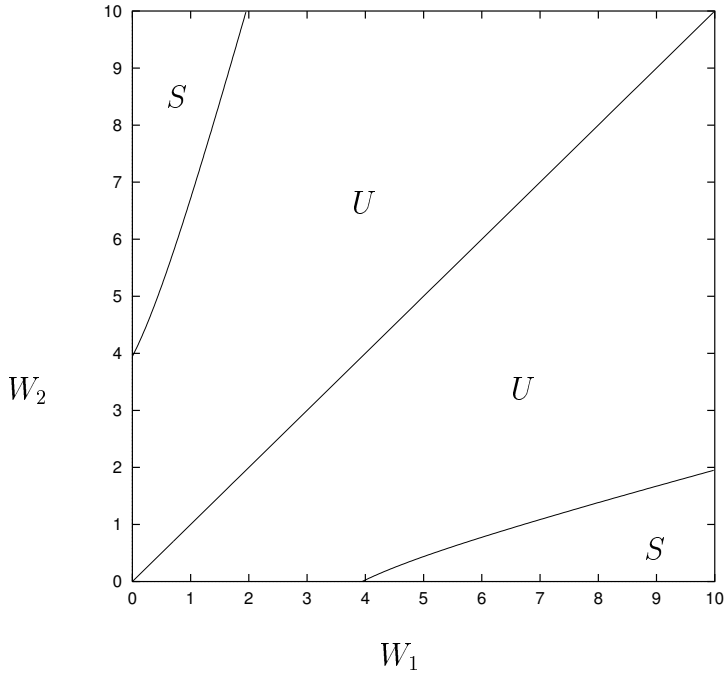

Figure 3.6: Neutral stability curves for $C = \infty$, $k = \infty$, $\kappa = \frac{1}{2}$. U = unstable, S = stable [174]. There is stability if $W_1 = W_2$ or if W_1 and W_2 are very different from each other. Elsewhere the interface is unstable.

instability for *all* other W_1, W_2. This is qualitatively different from Renardy's result for UCM above.

Intermediate concentrations

Because the concentrated limit is stable for widely separated values of W_1 and W_2 but the dilute limit is not, there must exist some critical concentration C_{crit} above which restabilisation occurs. We define this concentration by looking at the behaviour of ω as W_2 increases, with $W_1 = 0$. For $C < C_{crit}$ the imaginary part of ω is always positive, whereas for $C > C_{crit}$ the growth rate is negative as $W_2 \to \infty$. Numerical results show $C_{crit} \approx 8$. Above this

value we can find pairs of Weissenberg numbers for which the flow is stable to perturbations of short wavelength. Indeed, for these values the flow is found (using the methods of section 3.5) to be stable to all wavelengths, provided the long-wave modes are also stable: for example, at $C = 100$, $\kappa = 0.5$, $W_1 = 0$, the flow is stable for all $W_2 > 4.25$.

3.4.3 The effect of flow strength on short waves

The weak flow limit, $W_1, W_2 \to 0$

If both Weissenberg numbers tend to zero, keeping their ratio constant, we can expand the streamfunction, stretches and eigenvalue as Poincaré series for arbitrary C, and obtain:

$$\omega = -\tfrac{1}{4}\tfrac{C^2}{(1+C)^2}(W_1 - W_2)(W_1 + W_2) +$$
$$\tfrac{1}{16}\tfrac{C^3}{(1+C)^4}(W_1 - W_2)(W_1 + W_2)(3(W_1^2 + W_2^2) + 2C(2(W_1^2 + W_2^2) - W_1W_2)) +$$
$$\tfrac{i}{32}\tfrac{C^3}{(1+C)^5}(W_1 - W_2)^2(W_1 + W_2) \times$$
$$((C^2 + 3C + 1)(3(W_1^2 + W_2^2) + 4W_1W_2) + W_1^2 + W_2^2)$$
$$+ O(W_i^6). \quad (3.47)$$

We note for these slow weak flows that the growth of the disturbance is inhibited by the total zero-shear viscosity $1 + C$ (not just the solvent viscosity). Furthermore, because in the limit $W_i \to 0$ there is no elasticity, the growth rate must vanish as $W_i \to 0$. Our result for ω is consistent with this requirement, *i.e.* this is *not* a spurious instability having large growth rate that would violate a slow flow expansion (section 1.3.7).

In a slow flow expansion, as explained in chapter 1, any simple fluid may be regarded as an nth-order fluid with an error of $O(W^n)$. Surprisingly, perhaps, the first term giving a nonzero growth rate is $O(W_i^5)$, thus we anticipate that a fourth-order fluid would not be able to capture this behaviour. We expect that a sixth-order fluid would be needed, but, although such a result would be universal, the result is unlikely to be useful in view of the large number of undetermined coefficients in the slow flow expansion.

Strong flow limit, high elasticity, $W_2 \to \infty$

In the large Weissenberg number limit, at leading order the stretches a_{11} and a_{12} in equations (3.36) – (3.38) scale as W^2 (for $y = O(1)$) so that the vorticity equation (3.35) loses its highest derivative. Thus the limit is singular, suggesting the appearance of boundary layers. In order to simplify the problem, we consider the case where a Newtonian fluid occupies one half-plane, $y > 0$, (which is equivalent to setting $W_1 = 0$) with strong elastic forces only in $y < 0$.

Detailed analysis reveals that two lengthscales arise in the elastic fluid near the interface. First, there is a boundary layer of width $1/W_2$, across which the pressure is approximately constant but the velocities ψ, $D\psi$ and the shear stress $\boldsymbol{\sigma}_{12}$ change by a factor of order W_2. Within this layer, there is a balance between the growth (or decay) of the perturbation and the elastic relaxation terms in the evolution of the stretches. Second, on a lengthscale of order unity (remembering that all lengthscales have been rescaled by k^{-1} here), there arises an incompressible elastic deformation in which elastic forces dominate viscous forces so that $\psi \sim ye^{-y}$ and $\nabla^2 p = 0$.

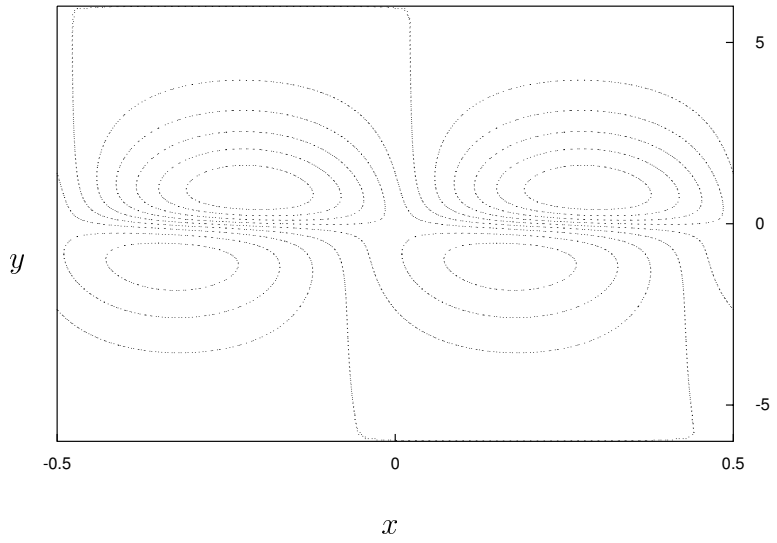

Figure 3.7: Streamlines of the perturbation to Couette flow; unstable case. $C = 0.2$, $W_2 = 5$. The Weissenberg number W_2 is large enough for an elastic boundary layer to be apparent at the interface.

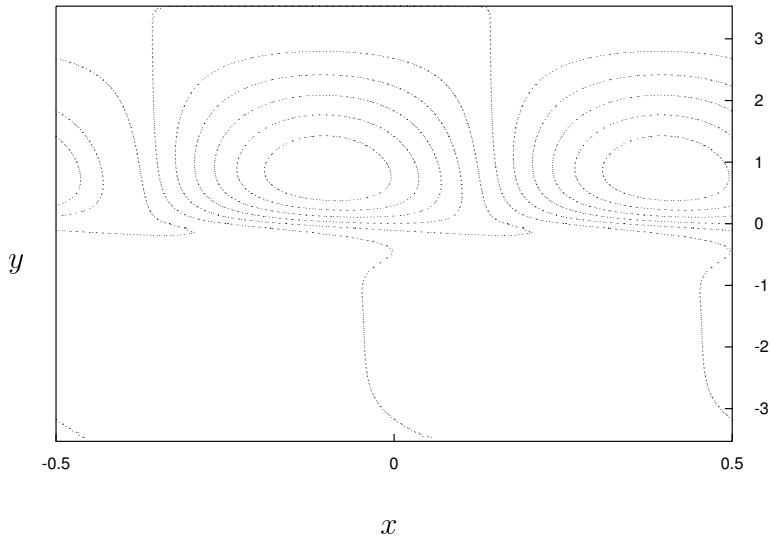

Figure 3.8: Streamlines of the perturbation to Couette flow; stable case. $C = \infty$ (UCM fluid), $W_2 = 5$. As in figure 3.7, the value of W_2 is sufficiently high for the elastic boundary layer to be seen.

The advection due to shear remains important.

Typical streamlines of the perturbation flow (calculated numerically) are shown in figures 3.7 and 3.8, showing the elastic boundary layer.

The eigenvalue ω is of order $1/W_2$ but its sign is not obvious, and needs to be determined numerically as a function of C. As noted above we find that the growth rate changes sign at $C \approx 8$.

This limit is difficult to analyse and the result may be surprising because although the jump in $\mathbf{\Sigma}_{xx}$ is large ($W_1 - W_2$ is large) the growth rate ω is nevertheless small ($O(1/W_2)$). The reason is that two comparably large effects are in competition: the highly elastic fluid strongly resists the perturbation, with the boundary layer acting rather like an extra surface tension. This greatly reduces the growth rate and can (for sufficiently high concentrations $C > C_{crit}$) prevent the instability.

Arbitrary flow strength

We conclude from the asymptotic cases examined above that, for fixed $C < C_{crit}$, the growth rate of disturbances will be small (and positive) if $W_1 - W_2$ is small (since this reduces the driving force) and small in magnitude if $W_1 - W_2$ is large (since the elastic resistance then rises). Thus there is an intermediate value of $W_1 - W_2$ at which growth is largest, as shown in figure 3.9.

3.5 Numerical results

Away from the limits $k \to 0$ (section 3.3) and $k \to \infty$ (section 3.4), a numerical study was used.

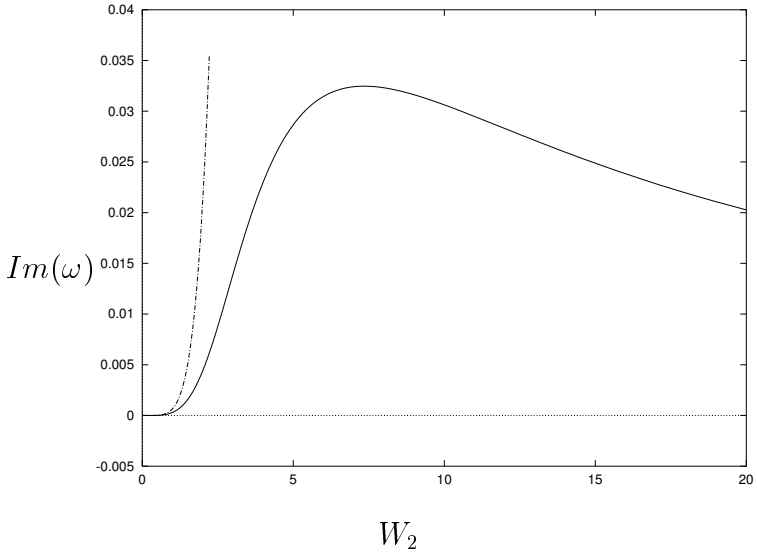

Figure 3.9: Growth rate against W_2 when $C = 0.2$, $W_1 = 0$; the dotted curve is the asymptote found for small W. As $W_2 \to \infty$, the growth rate is proportional to $1/W_2$, but the coefficient is not known analytically.

The system (3.15) – (3.23) is a fourth-order differential equation for $\psi(y)$ with three-point boundary conditions. Because of the interfacial jump conditions, the simple numerical method described in chapter 2 needs extending.

Instead of integrating from the centreline to the wall, the basis stream-functions are integrated to the interface from both the wall and the centreline. The four jump conditions at the interface then become (defining ζ through the kinematic boundary condition (3.23)) a matrix equation of the form:

$$\boldsymbol{M}\boldsymbol{\Psi} = \mathbf{0} \tag{3.48}$$

where $\boldsymbol{\Psi}$ is the vector of coefficients of each of the four linearly independent basis functions. Thus the determinant of $\boldsymbol{M}(\omega)$ needs to be made zero. A Newton-Raphson procedure is used, as in the case with no interface.

Figures 3.10 to 3.13 show representative cases of the behaviour of the growth rate with wavenumber k, for the most unstable disturbances.

In this illustration, we have chosen the value $\kappa = \frac{1}{2}$, for which sinuous and varicose long-wave modes are both unstable if the outer fluid is more elastic, and both stable otherwise. The sinuous mode is the more unstable for long waves [79], but can be overtaken by the varicose mode at some wavenumber of order unity. The modes necessarily have the same behaviour for very short waves.

If the outer fluid is less elastic, then long waves are stable, and the behaviour is more complicated. The least stable mode at long waves is again that identified by Chen [33], but continuation of this mode to high wavenumbers does not necessarily give the least stable short-wave mode. Similarly, continuation of sinuous and varicose modes may also lead to different roots of the short-wave problem. A selection of the typical growth rate curves is

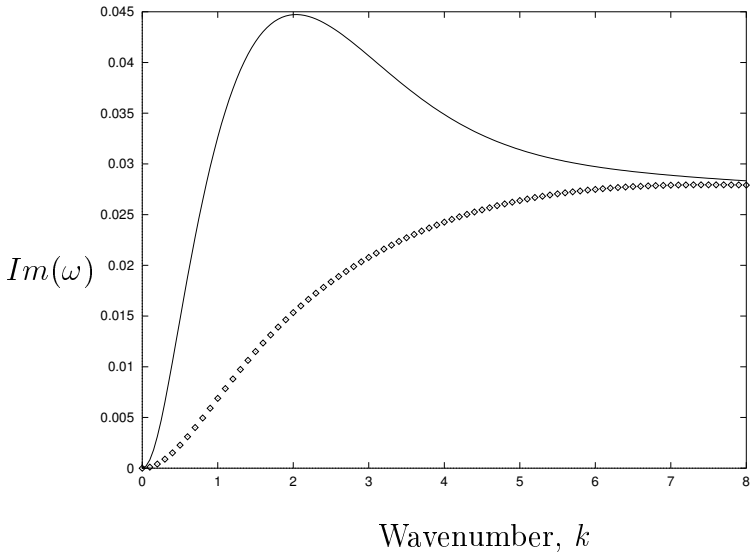

Figure 3.10: Growth rates plotted against k for a case where both long and short waves are unstable: $C = 0.2$, $\kappa = 0.5$, $W_1 = 4$, $W_2 = 0$. The outer fluid is the more elastic, and the fastest growing mode is sinuous with $k \sim 2$. The solid curve is the sinuous mode, the points show the varicose mode.

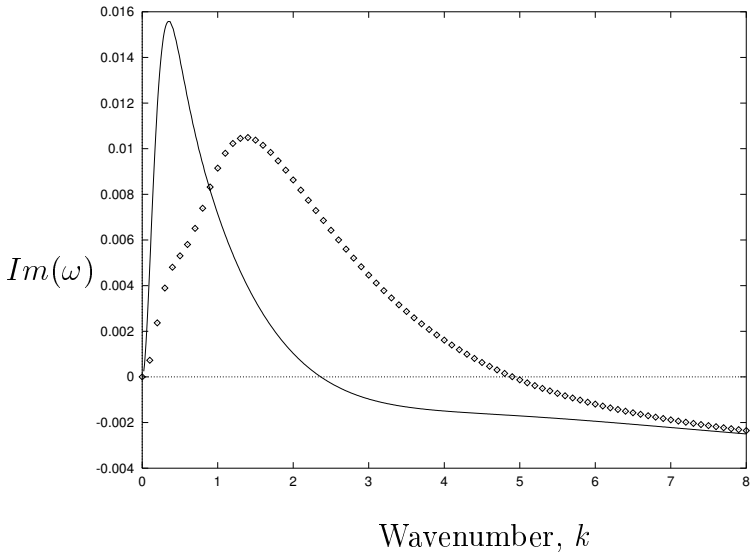

Figure 3.11: Growth rates plotted against k for a case where long waves are unstable and short stable: $C = \infty$ (UCM), $\kappa = 0.5$, $W_1 = 5$, $W_2 = 0$. The outer fluid is the more elastic, and the fastest growing mode is sinuous with $k \sim 0.5$. The first peak is the sinuous mode, and the points show the varicose mode.

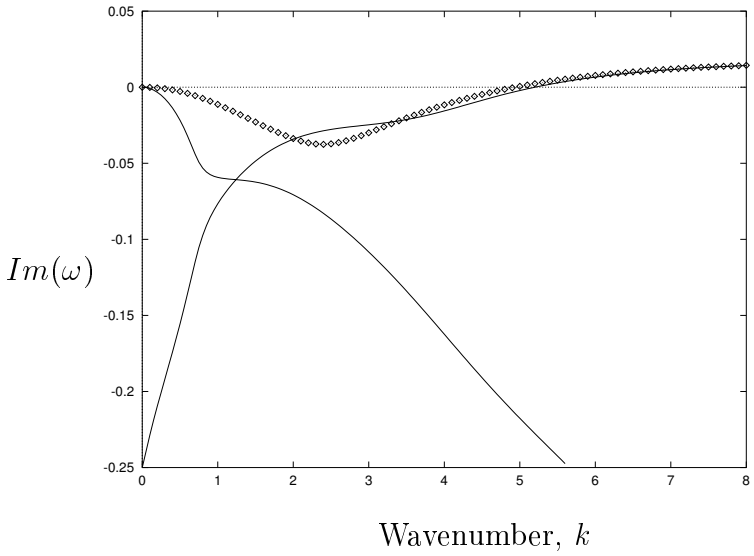

Figure 3.12: Growth rates plotted against k for a case where long waves are stable and short unstable: $C = 0.2$, $\kappa = 0.5$, $W_1 = 0$, $W_2 = 4$. The inner fluid is the more elastic, and the fastest growing mode has $k = \infty$. The varicose mode (points) almost always has the higher growth rate; two different sinuous modes are shown (solid lines).

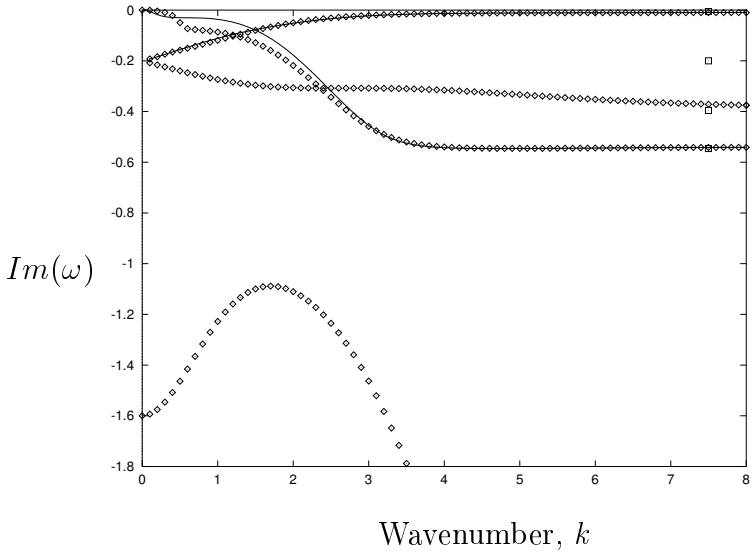

Figure 3.13: Growth rates plotted against k for a case where both long and short waves are stable: $C = \infty$ (UCM), $\kappa = 0.5$, $W_1 = 0$, $W_2 = 5$. The inner fluid is the more elastic; all modes decay. The sinuous modes are solid lines, the points are the varicose modes. In the short-wave limit, the dispersion relation is a polynomial which has five roots [174], four of which are marked here with small squares. The fifth has a decay rate of 5.8, and is not on the scale of this graph.

plotted in figures 3.12 and 3.13. Note that, when one of the Weissenberg numbers is zero, there is a mode for which long waves decay at rate $1/W$, *i.e.* the relaxation rate of the elastic fluid. This corresponds to an elastic wave, confined in the elastic fluid close to the interface (analysis of equations (3.15) – (3.23) reveals a boundary layer of width k), which relaxes at the molecular relaxation rate[1].

For dilute solutions with C small (figure 3.12), the most unstable disturbances are either short wave, or have k of order unity, *i.e.* the disturbance wavelength is comparable with the channel width. Thus the long-wave analysis, though sufficient to demonstrate instability, may be a poor predictor of the type, wavelength and growth rate of instability seen experimentally [162].

For large C (figure 3.13), Renardy's analysis [174] for UCM as $k \to \infty$ gives a quintic polynomial for ω having five distinct roots. We are able to find the least stable branch for both sinuous and varicose modes, and all the modes we find match up with the short-wave limit.

3.6 Conclusions

We have investigated the stability to linear perturbations of a two-fluid planar Poiseuille flow of Oldroyd-B fluids, matching all the fluid properties except elasticity, while neglecting inertia and surface tension.

For dilute Oldroyd-B fluids, short waves are unstable over the full range of Weissenberg numbers $W_1 \neq W_2$. Near the UCM limit, however, there is

[1] We are grateful to the referee of [218] for pointing this out.

instability for only a finite range of $W_1 - W_2$. The instability occurs for small W at $O(W^5)$ so the phenomenon should not be limited to Oldroyd-B fluids. As the wavelength tends to zero, the growth rate remains finite.

Long waves are unstable to sinuous modes if the coating is more elastic than the core, and to varicose modes if the more elastic fluid occupies a small enough fraction of the channel. The short-wave behaviour of the system is independent of the type of perturbation (sinuous or varicose) and of which fluid forms the core and which the coating.

Since the long-wave stability characteristics are reversed by interchanging the core and coating, the short- and long-wave limits are fundamentally different from one another. In most cases, the short wave mode is unstable, and, having finite growth rate, is predicted to grow faster than the long-wave mode, whose growth rate is small. The largest growth rate usually occurs for some moderate wavelength comparable with the channel width.

We have not been able to verify this wavelength prediction with reference to existing experiments. Mavridis & Shroff [134] have investigated this geometry, but their photographs are taken after processing, and the instability has developed well into the nonlinear régime. The distortions of the unstable interface are irregular in shape and length, but a dominant lengthscale (in the single available photograph of the interface) appears to be an order of magnitude smaller than the channel width, *i.e.* within our short-wave régime.

An ingredient neglected in our short-wave analysis is surface tension. A dimensionless group that measures the relative importance of normal stress

and surface tension effects is an elastic capillary number:

$$\frac{N_1}{Tk} = \frac{\mu_* \lambda \dot{\gamma}_*^2}{T_* k_*} \tag{3.49}$$

Here T is the surface tension coefficient, k the wavenumber of the perturbation at the interface, and N_1 the jump in the first normal stress difference. Starred quantities are in their dimensional form. λ is the fluid relaxation time, and $\dot{\gamma}_*$ the shear-rate at the interface, so that $\lambda\dot{\gamma}_*$ is the Weissenberg number. μ_* is the shear viscosity.

For viscous polymeric liquids with $\mu_* \sim 1$P, and surface tension coefficient $T_* \sim 10$ dyne/cm, at a shear-rate of $\dot{\gamma}_* \sim 1\text{s}^{-1}$ and relaxation time λ of order 1s this imposes the strong requirement that the wavelengths considered should exceed 10cm. Since however the elastic capillary number scales with $\dot{\gamma}_*^2$, at shear-rates of 10^2s^{-1}, the neglect of surface tension is justified provided that the wavelength is in excess of 10^{-3}cm. In a channel of width 1cm this value of k lies on the short-wave plateau of figures 3.10 – 3.13.

The mechanism of all the instabilities here is the jump in N_1. This variation in N_1 is present also in elastic liquid flows where N_1 varies continuously across the channel (and for which surface tension vanishes). It may therefore be expected that continuous stratification may also generate instability. This observation is the motivation for the work in chapter 4.

Chapter 4

Instability of Fluid having Continuously Stratified Normal Stress

4.1 Introduction

Purely elastic instabilities of homogeneous Oldroyd-B fluids are known to occur in flows having curved streamlines (section 1.4.2), and in plane parallel flows of coextruded fluids where the viscosity is constant but where there is a discontinuity in normal stress (chapter 3). We do not know of any case in which a plane parallel flow of a fluid with constant viscosity, but whose elastic properties are continuously stratified across the channel, has been shown to be unstable.

A strong suggestion that such an instability *could* arise is given by the physical explanation of long-wave instabilities for coextruded elastic liquids provided by Hinch *et al* [79]. The idea, discussed in chapter 3, is that a perturbation of the interface exposes the jump in normal stress at the interface, which drives a flow. One might guess, then, that if a variation in normal stress occurs over a thin enough region, the same mechanism will generate an instability in a continuously stratified fluid. Indeed, at first sight this long-wave mechanism suggests that even a Poiseuille flow of an Oldroyd-B fluid with uniform elastic properties will be unstable, because the cross-stream variation of normal stress due to the variation of the shear-rate across the channel appears rapid to a long-wave disturbance. However, such a flow is stable (section 1.5.1). The long-wave argument above is, in general, erroneous for a fluid with continuously varying properties, because it fails to take proper account of convective effects. As shown in chapter 3, in a flow with a fluid-fluid interface there is a long-wave instability (having wavenumber $k \to 0$). The streamfunction is convected with velocity u, the streamwise velocity at the interface, and the growth is a second-order effect. Thus the

complex frequency ω is:

$$\omega = ku + i\sigma k^2 + O(k^3) \tag{4.1}$$

where σ is a constant having magnitude of order unity. Now if, instead, the fluid properties vary over a distance d that is small compared with the width of the channel, different fluid layers within this region are convected at velocities which differ by a quantity of order d. Thus different layers generate perturbation elastic stresses that are out of phase with each other by an amount of order kd. In order for the phase difference not to swamp the effect of the 'jump' (which is of order k^2), we need $kd \lesssim k^2$, and therefore $d \lesssim k \ll 1$. Very long waves with $k \ll d$ are expected to be stabilised.

We show, in this chapter, that channel flows of elastic liquids having constant viscosity and continuously varying elasticity can be subject to instabilities. For the (somewhat artificial) model problem we have chosen, both long-wave asymptotic (section 4.4) and numerical (section 4.5) solutions are available.

Since, however, the calculation shows that the mechanism is robust, we anticipate that it will appear too in other channel flows that involve rapid variations in material properties leading to rapid changes in N_1. Another example of such a flow is investigated in chapter 5.

4.2 Geometry and constitutive model

We consider an Oldroyd-B fluid whose constitutive equation is given in dimensional form by:

$$\boldsymbol{\Sigma} = -P\boldsymbol{I} + \mu_*(\boldsymbol{\nabla U} + \boldsymbol{\nabla U}^\top) + G(\boldsymbol{\eta})\boldsymbol{A} \tag{4.2}$$

$$\overset{\nabla}{\boldsymbol{A}} = -\frac{1}{\tau(\boldsymbol{\eta})}(\boldsymbol{A} - \boldsymbol{I}) \tag{4.3}$$

where $\boldsymbol{U}$ is the velocity field, $\boldsymbol{\Sigma}$ the stress tensor, and $\boldsymbol{A}$ the microstructural configuration tensor[1]. The elastic modulus G and time constant τ are each functions of a Lagrangian variable $\boldsymbol{\eta}(\boldsymbol{x}, t)$ that labels each material point. Because $\boldsymbol{\eta}$ is a material property,

$$\frac{D\boldsymbol{\eta}}{Dt} = 0. \tag{4.4}$$

In investigating the stability of a steady planar channel flow, sketched in figure 4.1, this description may be simplified by identifying each material point by its position $y = \eta$ in the absence of any perturbation. In effect, we regard the continuously stratified Oldroyd-B fluid as a multi-layer coextrusion flow in which an infinite number of nozzles feed fluid into the channel, each at its own level.

In a steady parallel flow the fluid has viscosity $\mu_* + G(\eta)\tau(\eta)$ at level $y = \eta$. In order to isolate the instability mechanism associated with normal stress, and not viscosity variation, we choose the modulus so that $G(\eta) = \mu_* C/\tau(\eta)$, where C is a constant. The viscosity is then $\mu_*(1 + C)$, independent of η as

[1] The deviatoric stress may be shown using equation (4.4) to satisfy the alternative form of the Oldroyd-B equation $\overset{\nabla}{\boldsymbol{\Sigma}'} + \frac{1}{\tau(\eta)}\boldsymbol{\Sigma}' = 2\mu_* \left[\overset{\nabla}{\boldsymbol{E}} + \left(\frac{1}{\tau(\eta)} + \frac{G(\eta)}{\mu_*}\right)\boldsymbol{E}\right]$.

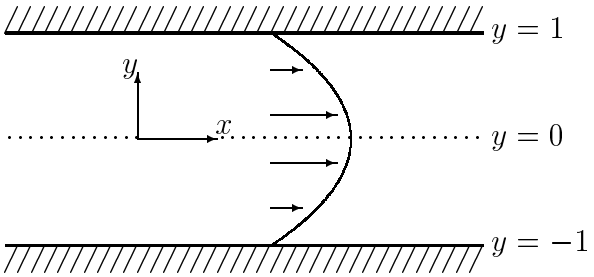

Figure 4.1: Flow geometry

for a homogeneous fluid. The first normal stress coefficient, on the other hand, is $2\mu_* C\tau(\eta)$, which we may vary arbitrarily by suitable choices of $\tau(\eta) > 0$.

We make the equations dimensionless using the solvent viscosity, μ_*, the half channel width, L, and the centreline fluid velocity, U_0. Defining $W(\eta) = U_0\tau(\eta)/L$, the equations become:

$$\boldsymbol{\Sigma} = -P\boldsymbol{I} + (\boldsymbol{\nabla U} + \boldsymbol{\nabla U}^\top) + \frac{C}{W}\boldsymbol{A} \tag{4.5}$$

$$\overset{\nabla}{\boldsymbol{A}} = -\frac{1}{W}(\boldsymbol{A} - \boldsymbol{I}). \tag{4.6}$$

It should be remembered that W is convected with material particles, thus $W = W(\eta)$ and $\eta = \eta(x, y, t)$, where $D\eta/Dt = 0$.

This is the equation given in chapter 2 by the conditions $\mu = 1$, $n = 1$, C constant. The base state is therefore:

$$\boldsymbol{U} = (1 - y^2, 0) \tag{4.7}$$

$$\boldsymbol{A} = \begin{pmatrix} 1 + 8W^2y^2 & -2Wy \\ -2Wy & 1 \end{pmatrix} \tag{4.8}$$

$$\mathbf{\Sigma} = \begin{pmatrix} -P + C/W + 8CWy^2 & -2y(1+C) \\ -2y(1+C) & -P + C/W \end{pmatrix} \tag{4.9}$$

$$P = P_\infty + C/W - 2(1+C)x. \tag{4.10}$$

It remains to choose the profile $W(\eta)$. We consider a symmetric profile so that $W(\eta) = W(-\eta)$. A convenient choice for $\eta > 0$ is then:

$$W = \overline{W} + \frac{\Delta W}{\pi} \arctan((\eta - \kappa)/q) \tag{4.11}$$

in which W changes by an amount ΔW across a layer, centred at $\eta = \kappa$, of dimensionless width $q = d/L$. In the limit $q \to 0$:

$$W \to \begin{cases} W = \overline{W} + \Delta W/2 & \eta > \kappa \\ W = \overline{W} - \Delta W/2 & \eta < \kappa \end{cases} \tag{4.12}$$

so we should recover the two-fluid coextrusion problem of chapter 3.

4.3 Perturbation flow

Referring back to chapter 2, and using the transformed equations of section 2.7, we find that the perturbation equations are:

$$-8ikCy^2W'\zeta + ik\sigma_{11} + \sigma'_{12} = 0 \tag{4.13}$$

$$ik\sigma_{12} + \sigma'_{22} = 0 \tag{4.14}$$

and the perturbation stresses are:

$$\sigma_{11} = -p + 2ik\psi' + \tfrac{C}{W}a_{11} \tag{4.15}$$

$$\sigma_{12} = \psi'' + k^2\psi + \tfrac{C}{W}a_{12} \tag{4.16}$$

$$\sigma_{22} = -p - 2ik\psi' + \tfrac{C}{W}a_{22} \tag{4.17}$$

in which:

$$\left(-i\omega + ik(1-y^2) + \frac{1}{W}\right) a_{11} = 16ikW^2y\psi + 2(1+8W^2y^2)ik\psi' - 4Wy\psi'' - 4ya_{12} \tag{4.18}$$

$$\left(-i\omega + ik(1-y^2) + \frac{1}{W}\right) a_{12} = -2ikW\psi + (1+8W^2y^2)k^2\psi + \psi'' - 2ya_{22} \tag{4.19}$$

$$\left(-i\omega + ik(1-y^2) + \frac{1}{W}\right) a_{22} = -2ik\psi' - 4Wyk^2\psi \tag{4.20}$$

$$(-i\omega + ik(1-y^2))\zeta = -ik\psi \tag{4.21}$$

with boundary conditions:

$$\psi(1) = \psi'(1) = 0 \tag{4.22}$$

$$\text{Sinuous } \psi'(0) = \psi'''(0) = 0 \tag{4.23s}$$

$$\text{Varicose } \psi(0) = \psi''(0) = 0. \tag{4.23v}$$

The advantage of the transformation in section 2.7 is now apparent: the form of these equations is identical to those for which W is a constant except for the appearance of $W'(y)$ in equation (4.13).

In the familiar coextrusion case (chapter 3) involving two distinct fluids, W' is zero within either fluid, and integration of equation (4.13) across the interface yields the continuity condition:

$$[\sigma_{12}] = 8ikC\kappa^2 \Delta W \zeta(\kappa) \tag{4.24}$$

where κ is the position of the interface and brackets denote a jump across it. This limiting case would be impossible in the formulation of section 2.6.

4.4 Long-wave asymptotics

The considerations discussed in the introduction suggest that the most likely candidate for a long-wave ($k \to 0$) instability is a layer having width of order k. In consequence, we consider the distinguished limit in which $q = \tilde{q}k$ and $k \to 0$ with $\tilde{q}$ fixed. In that case, except in a layer of size k around $y = \kappa$, W takes constant values $\overline{W} + \Delta W$ for $y > \kappa$, and $\overline{W} - \Delta W$ for $y < \kappa$. As a result, the flow has the dynamics of coextruded Oldroyd-B fluids with matched viscosities $1 + C$. So far as the outer flow is concerned we may impose, by equation (4.13), a discontinuity $[\sigma_{12}]$ in tangential stress at $y = \kappa$. The magnitude of this discontinuity (which may be complex) is as yet unknown, and must be determined by analysis of the thin layer itself. We anticipate that the frequency of the disturbance will continue to have the form of equation (4.1):

$$\omega = ku + i\sigma k^2 \tag{4.25}$$

and thus the Deborah number, $\omega\tau$, associated with the perturbation is small. The perturbation elastic stresses respond quasi-statically to the flow, so giv-

ing rise to a Newtonian stress having shear viscosity $(1 + C)$.

4.4.1 Outer flow

As in chapter 3, the outer solution may be expressed entirely in terms of $[\sigma_{12}]$. We obtain:

$$\psi(\kappa) = \frac{[\sigma_{12}] f(\kappa)}{2(1+C)} \tag{4.26}$$

where $f = f_s$ for a sinuous mode, $f = f_v$ for a varicose mode and:

$$f_s(\kappa) = \kappa(1-\kappa)^2 \tag{4.27s}$$

$$f_v(\kappa) = \tfrac{1}{2}\kappa(1-\kappa)^2(\kappa^2 + 2\kappa - 1). \tag{4.27v}$$

4.4.2 Inner solution

Within the thin layer, the relevant lengthscale for y is k. Because k is small, the pressure within the layer is constant, and the x-momentum equation (4.13) reduces to:

$$(1+C)\psi''' - 8iCky^2 W'\zeta = 0 \tag{4.28}$$

where (equation (4.21)):

$$\zeta = -ik\psi/[-i\omega + ik(1-y^2)].$$

Since the layer is thin, we may expand about $y = \kappa$, writing:

$$\xi = k^{-1}(y - \kappa) \quad \text{with} \quad \xi = O(1). \tag{4.29}$$

Then from the expression (4.1) for ω we have:

$$\omega = k(1-\kappa^2) + i\sigma k^2 \tag{4.30}$$

where σ might itself be complex, so that:

$$(1+C)\frac{d^3\psi}{d\xi^3} - 8iCk^2\frac{\kappa^2}{i\sigma + 2\kappa\xi}\psi(\kappa)\frac{dW}{d\xi} = 0. \tag{4.31}$$

It follows, as expected, that as $k \to 0$, ψ and ψ' are continuous across the layer, and that ψ has the value $\psi(\kappa)$ in equation (3.27) or (3.30). Furthermore, to be self-consistent we must have:

$$\begin{aligned}
[\sigma_{12}] = (1+C)[\psi'']_{-\infty}^{\infty} &= (1+C)k^{-2}[d^2\psi/d\xi^2]_{-\infty}^{\infty} \\
&= (1+C)k^{-2}\int_{-\infty}^{\infty}\frac{d^3\psi}{d\xi^3}d\xi \\
&= 8iC\kappa^2\psi(\kappa)\int_{-\infty}^{\infty}\frac{dW/d\xi}{i\sigma+2\kappa\xi}d\xi.
\end{aligned} \tag{4.32}$$

Substituting for $\psi(\kappa)$ gives the dispersion relation for σ:

$$\int_{-\infty}^{\infty}\frac{dW/d\xi}{i\sigma+2\kappa\xi}d\xi = \frac{(1+C)}{4iC\kappa^2 f(\kappa)} \tag{4.33}$$

where $f(\kappa) = f_s(\kappa)$ for a sinuous mode, and $f(\kappa) = f_v(\kappa)$ for a varicose mode.

For coextrusion of two distinct fluids, $dW/d\xi = \Delta W\delta(\xi)$, and thus:

$$\sigma = \sigma_0 = \Delta W\frac{4C\kappa^2 f(\kappa)}{(1+C)}. \tag{4.34}$$

If, on the other hand, we consider a continuous variation for W (equation (4.11)), then:

$$\frac{dW}{d\xi} = \frac{1}{\pi}\frac{\Delta W\tilde{q}}{\xi^2+\tilde{q}^2} \tag{4.35}$$

and thus:

$$\frac{1}{\pi}\int_{-\infty}^{\infty}\frac{\tilde{q}\,d\xi}{(\tilde{q}^2+\xi^2)(i\sigma+2\kappa\xi)}=\frac{1}{i\sigma_0}. \tag{4.36}$$

This integral is easily evaluated by the calculus of residues, giving:

$$\frac{1}{i\sigma_0}=\begin{cases}(i\sigma+2i\kappa\tilde{q})^{-1} & Re(\sigma)>0\\ (i\sigma-2i\kappa\tilde{q})^{-1} & Re(\sigma)<0.\end{cases} \tag{4.37}$$

We deduce that if $|\sigma_0|<2\kappa\tilde{q}$ there are no acceptable modes of the kind sought, but that if $|\sigma_0|>2\kappa\tilde{q}$ then:

$$|\sigma|=|\sigma_0|-2\kappa\tilde{q}. \tag{4.38}$$

All these estimates are confirmed by a full long-wave matched asymptotic expansion, included in section 4.6.

We conclude that in the long-wave limit:

a. Disturbances are propagated with the velocity, $U(\kappa)$, at the zero of the arctan profile.

b. The growth rate of disturbances, σk^2, is positive if *both* the analogous two-fluid situation is unstable *and* the interface is sharp enough, *i.e.* the thickness, d, of the layer is such that $d<|\sigma_0|kL/(2\kappa)$.

c. In this case, the eigenvalue (still in its nondimensional form) to the full problem becomes:

$$\omega=k(1-\kappa)^2+ik^2(\sigma_0-2\kappa q/k)+O(k^3). \tag{4.39}$$

d. Increasing σ_0 (by increasing ΔW) results in an increase in the largest value of q for which the eigenvalue exists. This process cannot be extended beyond the condition $\sigma_0\ll k^{-1}$.

e. For any nonzero width, d, of the layer, no asymptotically long-wave disturbance is available.

f. Because $f_s(\kappa) > f_v(\kappa)$, where both sinuous and varicose disturbances are unstable, sinuous modes are always more unstable than varicose ones, as in the long-wave limit of the coextrusion instability.

We cannot tell from a long-wave analysis the fate of waves which have wavelengths comparable with the channel width. For this purpose we need a full numerical solution, described in the next section.

4.5 Numerical results

Equations (4.13) – (4.20) define a fourth order ordinary differential equation for the unknown eigenvalue ω. We solve this problem, as described in chapter 2, using orthogonalisation, shooting from the centreline boundary conditions to the wall.

For very small values of q, the eigenvalues were found, as expected, to be similar to those for the two-fluid problem. As q increased, however, and the width of 'blurring' increased, the eigenvalues quickly became neutral. For $q > 0.04$ in most parameter ranges no interfacial modes, stable or unstable, could be found. An example set of results is shown in figure 4.2. In flows for which the maximum growth rate is larger, the instability persists for higher values of q.

In the long-wave limit, the growth or decay is lost earlier than for moderate length waves. The reason for this is the differing convection on different sides of the 'interface', as explained in the introduction, and is shown clearly

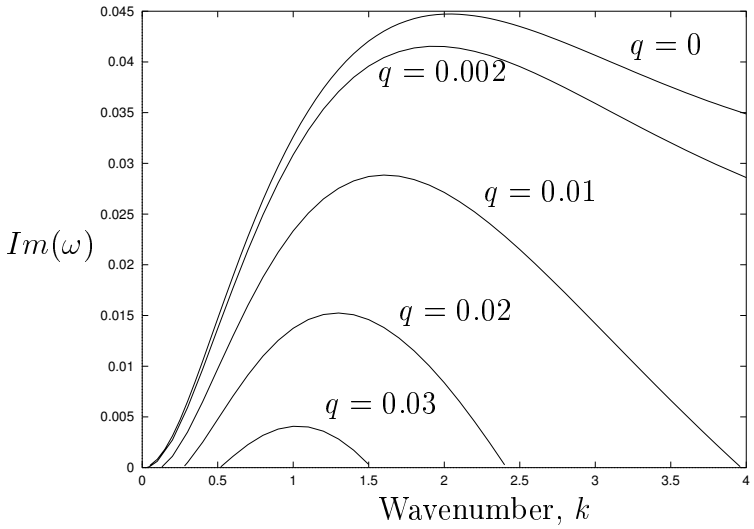

Figure 4.2: Decay of instability for increased 'blurring': Sinuous modes, $C = 0.2$, $\overline{W} = 2$, $\Delta W = 4$.

in the analysis of section 4.4. The numerical and asymptotic results are in agreement.

Analytically, the disappearance or appearance of a mode must be associated with a singularity of the governing equations: in this case, the term $-i\omega + ikU$ becomes zero at the point where the mode appears. This term comes from the material derivative D/Dt, and is present only because of the advection of W as a material quantity. We expect, therefore, that this root should exist only where there is advection of material properties.

4.6 Appendix: Long-wave asymptotics

In this appendix, we show the detailed asymptotic expansion used in section 4.4. We use k as our small parameter. The set of equations we are

solving is:

$$\left(-i\omega + ik(1-y^2) + \frac{1}{W}\right) a_{11} = 16ikW^2 y\psi + 2(1+8W^2y^2)ik\psi' - 4Wy\psi'' - 4ya_{12} \quad (4.40)$$

$$\left(-i\omega + ik(1-y^2) + \frac{1}{W}\right) a_{12} = -2ikW\psi + (1+8W^2y^2)k^2\psi + \psi'' - 2ya_{22} \quad (4.41)$$

$$\left(-i\omega + ik(1-y^2) + \frac{1}{W}\right) a_{22} = -2ik\psi' - 4Wyk^2\psi \quad (4.42)$$

$$\sigma_{11} = -p + 2ik\psi' + \tfrac{C}{W}a_{11} \quad (4.43)$$

$$\sigma_{12} = \psi'' + k^2\psi + \tfrac{C}{W}a_{12} \quad (4.44)$$

$$\sigma_{22} = -p - 2ik\psi' + \tfrac{C}{W}a_{22} \quad (4.45)$$

$$-8ikCy^2W'\zeta + ik\sigma_{11} + \sigma_{12}' = 0 \quad (4.46)$$

$$ik\sigma_{12} + \sigma_{22}' = 0 \quad (4.47)$$

$$-ik\psi - (-i\omega + ik(1-y^2))\zeta = 0 \quad (4.48)$$

$$W = \overline{W} + \tfrac{\Delta W}{\pi}\arctan((y-\kappa)/q) \quad (4.49)$$

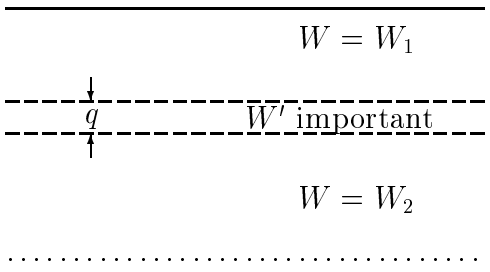

Figure 4.3: Three regions for asymptotic analysis of a fluid in which W varies sharply with η.

with boundary conditions:

$$\text{Sinuous} \quad \psi'(0) = \psi'''(0) = 0 \tag{4.50s}$$

$$\text{Varicose} \quad \psi(0) = \psi''(0) = 0 \tag{4.50v}$$

$$\psi(1) = \psi'(1) = 0. \tag{4.51}$$

We set $q = \tilde{q}k$ and assume $\tilde{q}$ to be positive.

There are clearly three regions (figure 4.3): two outer regions consisting of the main body of each fluid, where the Weissenberg number is not noticeably varying and the equations are those of a normal Oldroyd-B fluid; and the interior of the varying layer, in which the W' term plays a large part.

4.6.1 Outer region

We consider the two outer regions first. Here, at leading order in k, the equation becomes:

$$\psi'''' = 0. \tag{4.52}$$

Our two outer solutions are, in the fluid nearer the wall:

$$\psi = \phi_1 = E_2(y-1)^2 + E_3(y-1)^3 \tag{4.53}$$

and in the centre fluid:

$$\text{Sinuous} \quad \psi = \phi_2 = F_0 + F_2 y^2 \tag{4.54s}$$

$$\text{Varicose} \quad \psi = \phi_2 = F_1 + F_3 y^3. \tag{4.54v}$$

4.6.2 Inner region

Within the inner region, we expect all the perturbations to vary rapidly on a lengthscale k, so we rescale the cross-channel coordinate, $y = \kappa + k\xi$, and work in terms of ξ. We let $d = \partial/\partial\xi$. The resultant equations have an obvious scaling, so we let $\alpha_{12} = k^2 a_{12}/W$, $\alpha_{11} = k^2 a_{11}/W$, $\alpha_{22} = a_{22}/W$. We also rescale the stresses: $s_{11} = k^2\sigma_{11}$, $s_{12} = k^2\sigma_{12}$ and $s_{22} = \sigma_{22}$. As in the coextrusion case, we set:

$$\omega = k(1-\kappa^2) + ik^2\sigma. \tag{4.55}$$

Defining $z = k\zeta$, the new equations are:

$$\begin{aligned}(1 + k^2W\sigma - ik^2W(2\kappa\xi + k\xi^2))\alpha_{11} = {} & 16ik^3W^2\kappa\psi + \\ & 16ik^4W^2\xi\psi + 2k^2(1 + 8W^2(\kappa + k\xi)^2)id\psi - \\ & 4W(\kappa + k\xi)d^2\psi - 4\kappa W\alpha_{12} - 4kW\xi\alpha_{12}\end{aligned} \tag{4.56}$$

$$\begin{aligned}(1 + k^2W\sigma - ik^2W(2\kappa\xi + k\xi^2))\alpha_{12} = {} & -2ik^3W\psi + \\ & (1 + 8W^2(\kappa + k\xi)^2)k^4\psi + d^2\psi - 2k^2W(\kappa + k\xi)\alpha_{22}\end{aligned} \tag{4.57}$$

$$(1 + k^2 W\sigma - ik^2 W(2\kappa\xi + k\xi^2))\alpha_{22} = -2id\psi - 4W\kappa k^2\psi - 4W\xi k^3\psi \quad (4.58)$$

$$s_{11} = -k^2 p + 2ik^2 d\psi + C\alpha_{11} \quad (4.59)$$

$$s_{12} = (d^2 + k^4)\psi + C\alpha_{12} \quad (4.60)$$

$$s_{22} = -kp - 2id\psi + C\alpha_{22} \quad (4.61)$$

$$-8iCk^2(\kappa + k\xi)^2 z dW + ik^2 s_{11} + ds_{12} = 0 \quad (4.62)$$

$$is_{12} + ds_{22} = 0 \quad (4.63)$$

$$\psi = (i\sigma + 2\kappa\xi + k\xi^2)z \quad (4.64)$$

Equation (4.62) tells us that we need to work to order k^2 in order to see the effect of the stratification. We set $\psi = \psi_0 + k\psi_1 + k^2\psi_2 + O(k^3)$.

Order 1 Calculation

Solving at leading order we obtain:

$$\psi_0 = A_0 + B_0\xi + C_0\xi^2. \quad (4.65)$$

We know that we want equivalence with the two-fluid problem as the layer thickness goes to zero, so we impose $B_0 = C_0 = 0$ at this point.

Order k Calculation

The next order of solution gives:

$$\psi_1 = A_1 + B_1\xi + C_1\xi^2. \quad (4.66)$$

Again, we use our prior knowledge to deduce that $C_1 = 0$.

Order k^2 Calculation

For matching onto the outer solutions, we do not need to find ψ_2 exactly, we simply need to find the change in ψ'' and ψ''' across the layer. Let us look at ψ''' first.

Third derivative

The third derivative, $\psi''' = k^{-3}d^3\psi$. Hence we look again at equation (4.62), substituting in the definitions of s and α. We may assume that $dW \to 0$ as $|\xi| \to \infty$ leaving it smaller than any relevant power of k. Hence:

$$[(1 + C + iCk^2W(i\sigma + 2\kappa\xi) + iCk^3W\xi^2)d^3\psi \\ + iCk^2W(-2\kappa d^2\psi + k(2d\psi - 2\xi d^2\psi)) - ik^4p] = O(k^4\psi) \quad (4.67)$$

where [...] indicates the change in value over the layer. We can use the fact that $d\psi = k\psi'$ to show that the change in ψ''' is of order k and is therefore zero to leading order.

Second derivative

Finally we need to find $[\psi''] = [d^2\psi_2]$ across the layer. We have solved two orders in k; at the next order, using all the solution values from the first two orders, we find:

$$d^3\psi_2 = 8i\tfrac{C}{1+C}A_0\kappa^2 dW(i\sigma + 2\kappa\xi)^{-1}. \quad (4.68)$$

Since $W = \overline{W} + \frac{\Delta W}{\pi}\arctan(\xi/\tilde{q})$, we have $dW = \frac{\Delta W}{\pi}\tilde{q}/(\tilde{q}^2 + \xi^2)$. This leaves us with an integral to find $[d^2\psi_2]$ which may be easily solved by contour

methods to give:

$$[d^2\psi_2] = 8i\frac{C}{1+C}A_0\kappa^2\tilde{q}\frac{\Delta W}{\pi}\int\frac{1}{(\tilde{q}^2+\xi^2)(i\sigma+2\kappa\xi)}d\xi \tag{4.69}$$

$$= 8\frac{C}{1+C}A_0\kappa^2\Delta W\begin{cases}(\sigma+2\tilde{q}\kappa)^{-1} & Re(\sigma)>0\\ (\sigma-2\tilde{q}\kappa)^{-1} & Re(\sigma)<0.\end{cases} \tag{4.70}$$

4.6.3 Matching

We have six constants to determine: E_2, E_3, and either F_0 and F_2 or F_1 and F_3 from the outer, and A_0 and B_1 from the inner. A_1 does not appear at leading order when we rescale to the outer solution.

In order to finish the calculation, we must specify either varicose or sinuous-type modes: by way of example we show the varicose case.

The six matching equations are (in order ψ''' down to ψ):

$$\begin{pmatrix} 0 & 0 & 0 & 6 & 0 & -6\\ G & 0 & -2 & 6(1-\kappa) & 0 & 6\kappa\\ 0 & -1 & 0 & 0 & 1 & 3\kappa^2\\ 0 & 1 & 2(1-\kappa) & -2(1-\kappa)^2 & 0 & 0\\ -1 & 0 & 0 & 0 & \kappa & \kappa^3\\ 1 & 0 & -(1-\kappa)^2 & (1-\kappa)^2 & 0 & 0\end{pmatrix}\begin{pmatrix}A_0\\B_1\\E_2\\E_3\\F_1\\F_3\end{pmatrix}=0 \tag{4.71}$$

where:

$$G = 8\frac{C}{1+C}\kappa^2\Delta W\begin{cases}(\sigma+2\tilde{q}\kappa)^{-1} & Re(\sigma)>0\\ (\sigma-2\tilde{q}\kappa)^{-1} & Re(\sigma)<0.\end{cases} \tag{4.72}$$

The solvability condition for nontrivial solutions of this matrix system becomes:

$$Gf_v(\kappa) = \tfrac{1}{2}G\kappa(1-\kappa)^2(\kappa^2+2\kappa-1) = 2. \tag{4.73}$$

The equivalent equation for a sinuous mode is:

$$Gf_s(\kappa) = G\kappa(1-\kappa)^2 = 2. \tag{4.74}$$

In either case:

$$G\sigma_0 = 8\tfrac{C}{1+C}\kappa^2\Delta W \tag{4.75}$$

where σ_0 is the corresponding eigenvalue for the two-fluid case. Applying equation (4.72), we obtain:

$$\sigma = \sigma_0 - 2\tilde{q}\kappa \tag{4.76}$$

if $Re(\sigma) > 0$, and:

$$\sigma = \sigma_0 + 2\tilde{q}\kappa \tag{4.77}$$

otherwise. These equations can only be self-consistent if $|\sigma_0| > 2\tilde{q}\kappa$; otherwise the eigenvalue does not exist. We reached the same conclusion in a less formal way in equation (4.38) of section 4.4.

Chapter 5

Channel Flows having Variations in Polymer Concentration

5.1 Introduction

In chapter 4, we generalised the instability caused by a jump in W to that arising from a steep gradient in $W(\eta)$. As we will prove explicitly in chapter 7, this instability depends upon the fact that the relaxation time, W, is taken to be a material property, and therefore to be carried with each fluid parcel.

For a real fluid, this assumption may not be correct: such small-scale advection cannot be verified experimentally, and it is not clear from physical arguments that relaxation-time is *necessarily* a property of a fluid and not in any way a property of its strain-rate environment.

The other dimensionless parameter in the Oldroyd-B model is concentration of polymer, which corresponds to a real physical quantity that is easily understood. The concentration in any material parcel changes only through slow cross-streamline diffusion of the polymer molecules, which may be assumed to be negligible if the polymers are long and the concentration gradients not too great. We shall return to this condition in section 5.5.

In this chapter, therefore, we consider a generalised Oldroyd-B fluid for which the concentration is a continuously stratified material property, $C = C(\eta)$, which varies steeply across the channel. We begin with the Heaviside limit for $C(\eta)$, equivalent to the flow of two distinct fluids.

The new complication in this chapter is that since the base state viscosity is discontinuous, so is the velocity gradient at the interface. Thus, although this problem is in some ways more natural than that studied in chapter 4, it is also more difficult. We shall assume that the relaxation time does not vary across the channel for this calculation. The extension to the case in which both C and W are stratified is straightforward.

5.2 Base state

As shown in chapter 2, the unidirectional channel flow profile is given as:

$$U' = P_0 y/(1+C) \tag{5.1}$$

$$\boldsymbol{A} = \begin{pmatrix} 1+2(WU')^2 & WU' \\ WU' & 1 \end{pmatrix} \tag{5.2}$$

$$P = P_\infty + C/W + P_0 x \tag{5.3}$$

$$\boldsymbol{\Sigma} = \begin{pmatrix} -P_\infty - P_0 x + 2CW(U')^2 & P_0 y \\ P_0 y & -P_\infty - P_0 x \end{pmatrix}. \tag{5.4}$$

In these expressions, the concentration C may depend on y. In the case where:

$$C = \begin{cases} C_1 & |y| > \kappa \\ C_2 & |y| < \kappa \end{cases} \tag{5.5}$$

the undetermined quantities above become:

$$P_0 = \frac{-2(1+C_1)(1+C_2)}{(1+C_1)\kappa^2 + (1+C_2)(1-\kappa^2)} \tag{5.6}$$

$$U = \frac{P_0}{2(1+C_1)(1+C_2)} \begin{cases} (1+C_2)(y^2-1) & |y| > \kappa \\ (1+C_1)(y^2-\kappa^2) + (1+C_2)(1-\kappa^2) & |y| < \kappa. \end{cases} \tag{5.7}$$

This is the Newtonian profile for two fluids of viscosity $1+C_1$ and $1+C_2$ respectively (sketched in figure 5.1 for a case where $C_1 > C_2$). Note that it involves a discontinuity in U' at $y = \kappa$. There is additionally a discontinuity in N_1 of magnitude $2WP_0^2\kappa^2[C/(1+C)^2]$ at the interface.

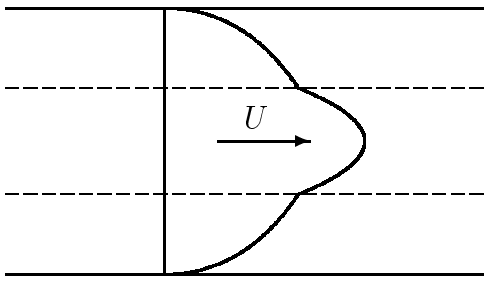

Figure 5.1: Flow profile U in the channel, for the case of two separate fluids in which the higher viscosity fluid is on the outside, $C_1 > C_2$.

5.3 Stability problem for two fluids

5.3.1 Governing equations

Each fluid is an Oldroyd-B fluid, and so the perturbation equations for each fluid are (as in chapter 3):

$$ik\sigma_{11} + \sigma'_{12} = 0 \tag{5.8}$$

$$ik\sigma_{12} + \sigma'_{22} = 0 \tag{5.9}$$

$$\sigma_{11} = -p + 2ik\psi' + \frac{C}{W}a_{11} \tag{5.10}$$

$$\sigma_{12} = \psi'' + k^2\psi + \frac{C}{W}a_{12} \tag{5.11}$$

$$\sigma_{22} = -p - 2ik\psi' + \frac{C}{W}a_{22} \tag{5.12}$$

$$\left(-i\omega + ikU + \frac{1}{W}\right)a_{11} = ik\psi A'_{11} + 2A_{12}\psi'' + 2A_{11}ik\psi' - 4ya_{12} \tag{5.13}$$

$$\left(-i\omega + ikU + \frac{1}{W}\right) a_{12} = ik\psi A'_{12} + \psi'' + A_{11}k^2\psi - 2ya_{22} \tag{5.14}$$

$$\left(-i\omega + ikU + \frac{1}{W}\right) a_{22} = -2ik\psi' + 2A_{12}k^2\psi \tag{5.15}$$

with the streamline perturbation defined as:

$$(-i\omega + ikU)\zeta = -ik\psi. \tag{5.16}$$

We have boundary conditions at the wall and centreline of the channel:

$$\psi(1) = \psi'(1) = 0 \tag{5.17}$$

$$\text{Sinuous } \psi'(0) = \psi'''(0) = 0 \tag{5.18s}$$

$$\text{Varicose } \psi(0) = \psi''(0) = 0. \tag{5.18v}$$

At the interface, $y = \kappa + \zeta \exp(ikx - i\omega t)$, we require continuity of $\boldsymbol{U} + \boldsymbol{u}$ and of the traction $(\boldsymbol{\Sigma} + \boldsymbol{\sigma}).\boldsymbol{n}$. These conditions become continuity at $y = \kappa$ of ψ, $\psi' + \zeta U'$, $\sigma_{12} - ik\zeta\Sigma_{11}$ and σ_{22}. It is the appearance of the $\zeta U'$ term here, involving the discontinuity of U', that differs from chapter 3.

5.3.2 Long-wave limit

In the limit of small k, we pose the series:

$$\omega = k\omega_1 + ik^2\sigma + O(k^3) \tag{5.19}$$

and expand all quantities in k. The details of this analysis are in section 5.6.

Sinuous mode

Using, for convenience, the notation:

$$g(\chi, \phi_1, \phi_2) \equiv \chi\phi_1 + (1-\chi)\phi_2 \tag{5.20}$$

we obtain, at leading order, for a sinuous mode:

$$\psi_0(\kappa) = \frac{(1+C_2)\kappa(1-\kappa)^2(C_1-C_2)\zeta}{g(\kappa, 1+C_1, 1+C_2)g(\kappa^2, 1+C_1, 1+C_2)} \tag{5.21}$$

and thus:

$$\omega_1 = \frac{(1+C_2)(1-\kappa^2)}{g(\kappa^2, 1+C_1, 1+C_2)} + \frac{(1+C_2)\kappa(1-\kappa)^2(C_1-C_2)}{g(\kappa, 1+C_1, 1+C_2)g(\kappa^2, 1+C_1, 1+C_2)}. \tag{5.22}$$

We note that the disturbance does not convect with the interface, as it does for the matched-viscosity case of chapter 3. At this leading order, the fluids are Newtonian so we may check this result by comparing with the flow (in the same geometry) of two Newtonian fluids with different viscosities[1].

[1] Consider the channel flow of two Newtonian fluids with viscosities μ_1, μ_2. The perturbation to the interface exposes the jump in U' due to the viscosity difference, causing a discontinuity in velocity at the interface, a perturbation to the velocity integral Q:

$$Q = \int_0^{\kappa+\zeta} U_2' dy + \int_{\kappa+\zeta}^1 U_1' dy = -1 - \zeta[U']_\kappa.$$

The extra part of Q, $-\zeta[U']$, must then be balanced by the perturbation Q, $\int_0^1 u'\, dy$, and since the perturbation flow (for a sinuous mode) is linear (and the shear stress continuous), the velocity profile is:

$$u(y) = \frac{-\zeta[U']}{\mu_1\kappa + \mu_2(1-\kappa)} \begin{cases} \mu_2(y-1) & y > \kappa \\ \mu_1 y & y < \kappa. \end{cases}$$

The growth rate, which occurs at order k^2, is:

$$\sigma = \left(\tfrac{1}{2}\kappa(\kappa-1)^2 \frac{M_0[U'] + [\Sigma_{11}]}{g(\kappa, 1+C_1, 1+C_2)} + \tfrac{1}{3}(\kappa-1)^3 M_1[U'] + \tfrac{1}{4}(\kappa-1)^4 \frac{M_1[U'](1+C_2)}{g(\kappa, 1+C_1, 1+C_2)} \right) \quad (5.23)$$

where:

$$M_0 = \frac{-WP_0(1+C_2)^2(\kappa-1)^2}{2g(\kappa, 1+C_1, 1+C_2)^2} \left(\frac{C_1}{1+C_1} - \frac{C_2}{1+C_2} \right) - 2WP_0\kappa + \frac{2WP_0\kappa g(\kappa, (1+C_1)^2, (1+C_2)^2)}{g(\kappa, 1+C_1, 1+C_2)(1+C_1)(1+C_2)} \quad (5.24)$$

$$M_1 = \frac{WP_0}{g(\kappa, 1+C_1, 1+C_2)} \frac{C_1(1+C_2)}{(1+C_1)^2} \quad (5.25)$$

$$[U'] = P_0\kappa \left(\frac{1}{1+C_1} - \frac{1}{1+C_2} \right) \quad (5.26)$$

$$[\Sigma_{11}] = 2WP_0^2\kappa^2 \left(\frac{C_1}{(1+C_1)^2} - \frac{C_2}{(1+C_2)^2} \right) \quad (5.27)$$

and:

$$P_0 = \frac{-2(1+C_1)(1+C_2)}{g(\kappa^2, 1+C_1, 1+C_2)}. \quad (5.28)$$

Mass conservation for the perturbation flow then gives:

$$\psi(\kappa) = \tfrac{1}{2}(\kappa-1)^2 \frac{\zeta[U']\mu_2}{g(\kappa, \mu_1, \mu_2)}$$

and hence (as in equation (5.22)):

$$\omega = kU(\kappa) + k\frac{\mu_2\kappa(1-\kappa)^2(\mu_1-\mu_2)}{g(\kappa, \mu_1, \mu_2)g(\kappa^2, \mu_1, \mu_2)}.$$

The growth rate is proportional to the Weissenberg number W, indicating once again that it is normal stress that drives the instability, and, as we would expect, the case $C_1 = C_2$ is neutrally stable. However, in other cases the sign of this growth rate is not obvious. The disturbance is stable for some triples (κ, C_1, C_2) and unstable for others. For instance, at $\kappa = \frac{1}{2}$ we have:

C_1	C_2	σ
2	6	$-0.037679\ W$
0	6	$0.003390\ W$
6	2	$0.052286\ W$
6	0	$0.069442\ W$

(5.29)

in which we observe that instability may occur when either $C_1 > C_2$ or $C_2 > C_1$, depending on the specific parameter values.

In the limit $\kappa \to 0$, the growth rate becomes:

$$\begin{aligned} \sigma &\sim -\frac{1}{3}\kappa W C_1 \left[\frac{1}{1+C}\right] \\ &= \frac{1}{3}\kappa W (C_1 - C_2)\frac{C_1}{(1+C_1)(1+C_2)} \end{aligned} \tag{5.30}$$

so the mode is unstable if $C_1 > C_2$, *i.e.* if the large outer fluid has the higher viscosity.

As $\kappa \to 1$, we have:

$$\begin{aligned} \sigma &\sim 4(\kappa-1)^2 W \frac{(1+C_2)^2}{1+C_1}\left(\left[\frac{C}{(1+C)^2}\right] - \frac{C_2}{(1+C_2)}\left[\frac{1}{(1+C)}\right]\right) \\ &= 4(\kappa-1)^2 W (C_1 - C_2)\frac{(1+C_2)}{(1+C_1)^3} \end{aligned} \tag{5.31}$$

which again indicates weak instability (at order $(\kappa-1)^2$) if $C_1 > C_2$.

Varicose mode

For a varicose mode, the scalings of the equations are similar. The leading-order growth rate has been calculated using 'Maple' [29].

We look at the limits of small and large κ. For a slender inner fluid, $\kappa \to 0$, we have:

$$\sigma \sim \kappa^3 W(C_1 - C_2)\frac{(C_2C_1 - 2 - C_1)}{(1 + C_2)^2(1 + C_1)} \tag{5.32}$$

whose sign is not obvious.

We expect that, in the wall limit $\kappa \to 1$, the two interfaces are too far apart to feel each other's effect. The growth rates should be the same for sinuous and varicose modes. We do indeed obtain:

$$\sigma \sim 4(\kappa - 1)^2 W(C_1 - C_2)\frac{(1 + C_2)}{(1 + C_1)^3}. \tag{5.33}$$

Figure 5.2 shows a plot of growth rate σ/W against interfacial position κ for the illustrative case $C_1 = 6$, $C_2 = 0$. In this figure, we see that the sinuous modes generally have the higher long-wave growth rate. However, it is possible for varicose modes alone to be unstable: for small κ, if $C_1 = 0$ then the growth rate is $\sigma = 2\kappa^3 W C_2(1 + C_2)^{-2}$ for the varicose mode, while the sinuous mode is stable.

5.3.3 Numerical results

In this section, we are studying the interfacial stability of two coextruded fluids with different polymer concentrations. The purpose of this is to generate an understanding of the instability. In the next section, we will generalise to

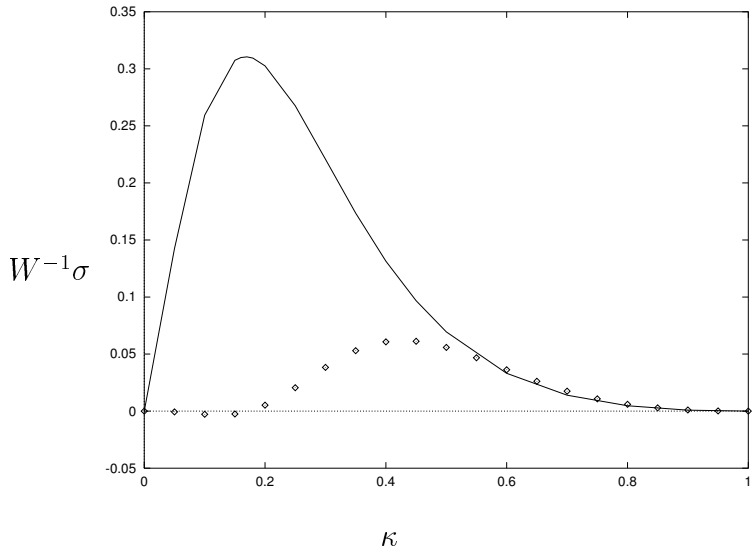

Figure 5.2: Plot of the growth rate of long waves against interface position, κ, for the representative case $C_1 = 6$, $C_2 = 0$. The solid line is for sinuous modes and the points for varicose modes. The sinuous modes usually have higher growth rate, and are always unstable, whereas the varicose modes are stable for $\kappa < 0.175$.

the case of a steep concentration gradient within a single fluid, *i.e.* a 'blurred' interface.

The interfacial mode is expected to have a short-wave asymptote of finite growth rate, as we saw for the case of fluids with differing elasticities. However, this short-wave analysis is not relevant to a 'blurred' interface (which has a short lengthscale of its own), so we do not investigate short waves, but rather move on to a numerical study of waves of moderate wavelengths.

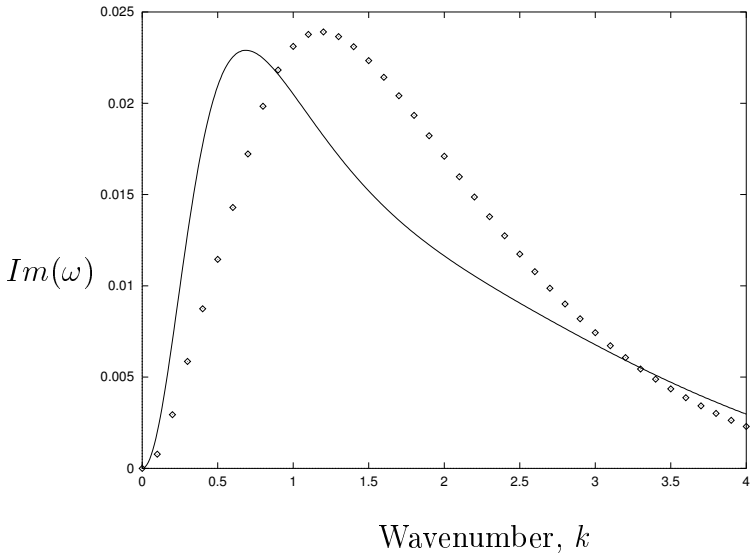

Figure 5.3: Plot of growth rate against wavenumber for a representative case in which both sinuous and varicose modes are unstable. $C_1 = 6$, $C_2 = 2$, $\kappa = 0.5$ and $W = 4$. The solid line shows the behaviour of sinuous modes, and the points the behaviour of varicose modes.

The equations are solved using the numerical method described in chapter 3, integrating from the wall and centre-line to the interface, and applying jump conditions there. Some typical plots of growth rate against wavenumber are shown in figures 5.3 and 5.4. The long-wave asymptote $Im(\omega) \sim k^2\sigma$

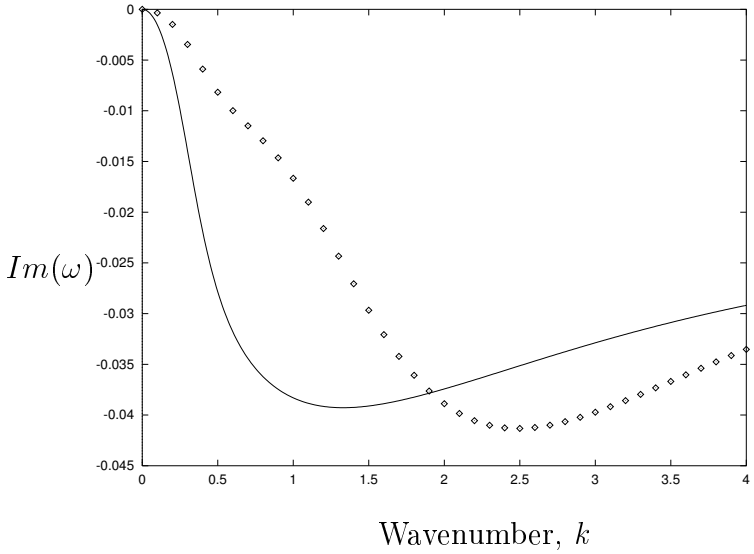

Figure 5.4: Plot of growth rate against wavenumber for a representative case in which both sinuous and varicose modes are stable. $C_1 = 2$, $C_2 = 6$, $\kappa = 0.5$ and $W = 4$. The solid line shows the behaviour of sinuous modes, and the points the behaviour of varicose modes.

is evident in these curves, and where long waves are unstable there is a wavelength on the same scale as the channel width which is most unstable. It is this wavelength which we might expect to survive longest during 'blurring' of the interface.

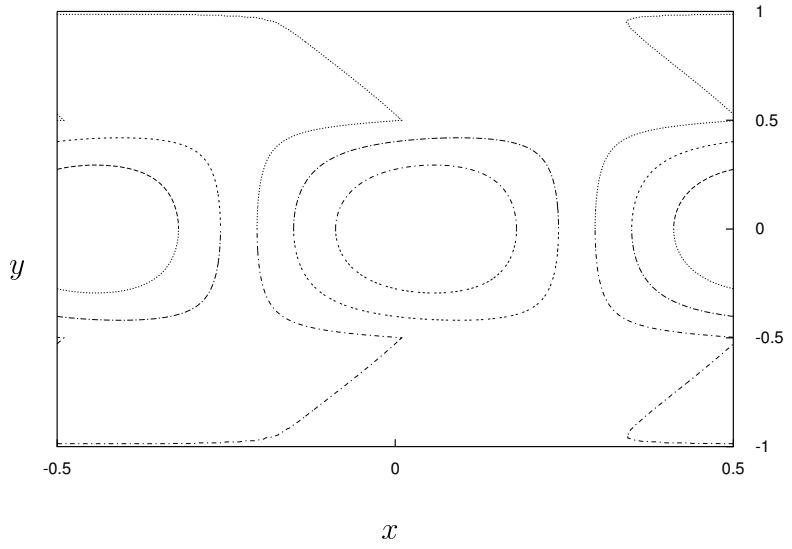

Figure 5.5: Streamlines of the perturbation flow, for coextruded fluids at two different concentrations. The most unstable wavenumber, $k = 0.69$, is chosen for a sinuous mode with $C_1 = 6$, $C_2 = 2$ and $W = 4$.

Figure 5.5 shows the streamlines of the perturbation flow for the most unstable point on the sinuous plot of figure 5.3. These are of similar form to the schematic streamlines shown in figure 3.2 on page 91, because the mechanism for long-wave instability here is the same as that in chapter 3. However, the discontinuity in viscosity produces streamlines with discontinuous slope at the interface.

5.4 Single fluid with varying concentration

Referring back to chapter 2, and substituting the advected stresses, we find that the perturbation equations for a continuously stratified fluid are:

$$ik\sigma_{11} + \sigma'_{12} = -2ikW\zeta P_0^2 y^2 (C(1+C)^{-2})' \tag{5.34}$$

$$ik\sigma_{12} + \sigma'_{22} = 0 \tag{5.35}$$

$$\sigma_{11} = -p + 2ik\psi' + \frac{C}{W}a_{11} \tag{5.36}$$

$$\sigma_{12} = \{\psi'' + \zeta P_0 y((1+C)^{-1})'\} + k^2\psi + \frac{C}{W}a_{12} \tag{5.37}$$

$$\sigma_{22} = -p - 2ik\psi' + \frac{C}{W}a_{22} \tag{5.38}$$

$$\left(-i\omega + ikU + \frac{1}{W}\right) a_{11} = ik\psi\frac{4W^2P_0^2y}{(1+C)^2} + 2A_{12}\{\psi'' + \zeta P_0 y((1+C)^{-1})'\} + 2ikA_{11}\psi' + 2a_{12}U' \tag{5.39}$$

$$\left(-i\omega + ikU + \frac{1}{W}\right) a_{12} = ik\psi\frac{WP_0}{(1+C)} + \{\psi'' + \zeta P_0 y((1+C)^{-1})'\} + A_{11}k^2\psi + U'a_{22} \tag{5.40}$$

$$\left(-i\omega + ikU + \frac{1}{W}\right) a_{22} = -2ik\psi' + 2A_{12}k^2\psi \tag{5.41}$$

$$(-i\omega + ikU)\zeta = -ik\psi \tag{5.42}$$

with boundary conditions:

$$\psi(1) = \psi'(1) = 0 \tag{5.43}$$

$$\text{Sinuous } \psi'(0) = \psi'''(0) = 0 \tag{5.44s}$$

$$\text{Varicose } \psi(0) = \psi''(0) = 0. \tag{5.44v}$$

As for the case of varying W (chapter 4), these equations are the same as for a single unstratified Oldroyd-B fluid, except for the terms involving ζ in equations (5.34) – (5.40).

The connection between these extra terms and their delta-function counterparts, for the case of two separate fluids discussed above, is clear: in equation (5.34), the term $-2ikW\zeta P_0^2 y^2 (C(1+C)^{-2})'$ becomes $-ik\zeta[\Sigma_{11}]$, *i.e.* it is a jump in N_1. Similarly, in equations (5.37), (5.39) and (5.40), the term $\zeta P_0 y((1+C)^{-1})'$ becomes $\zeta[U']$, *i.e.* a jump in velocity gradient caused by the jump in viscosity.

5.4.1 Specific C-profile

As an illustration we take $C(\eta)$ as:

$$C(\eta) = \overline{C} + \frac{\Delta C}{\pi} \arctan((\eta - \kappa)/q) \tag{5.45}$$

so that the limit $q \to 0$ is a Heaviside function, equivalent to the two-fluid case with $C_1 = \overline{C} + \Delta C/2$ and $C_2 = \overline{C} - \Delta C/2$.

As for the $W(\eta)$ case, discussed for long waves in section 4.4, we can divide the fluid into two regions: an outer, in which the fluid has the same

response as for the interfacial problem, and an inner, in which the variation of C is important. As noted above, the real part of the eigenvalue for the two-fluid case here does *not* correspond to the interfacial velocity. Nevertheless, the perturbation flow is still driven entirely by forcings at the interface, and so the interface region is central to the dynamics. The scalings are therefore the same as for the $W(\eta)$ problem. As the 'blurring' is increased, differential advection of different layers within the interface causes the forcing due to N_1 from these different layers to drift out of phase. It follows that no mode can be found for very long waves with $q \gg k$, and that the form of σ becomes:

$$\sigma = \sigma_0(1 - Aq/k) \tag{5.46}$$

for some constant A. Unfortunately, in this case the eigenvalue for the two-fluid problem is not simply expressible, so a full analytic solution of the general problem is not practicable.

A numerical study (of the same form as that in chapter 4) reveals that the response to 'blurring' of the interface is indeed as expected (figure 5.6 shows an example). Roots are shown for $q = 0$, 0.01, 0.02 and 0.03. The mode disappears when $Im(\omega) = 0$. As for the $W(\eta)$ case, higher values of q can be attained, that still show instability, by increasing the two-fluid growth rate σ_0, in this case by increasing W. However, the condition (in the long-wave limit) that $\sigma_0 \ll k^{-1}$ means that this process cannot continue indefinitely; thus no roots could be found for $q \geq 0.05$.

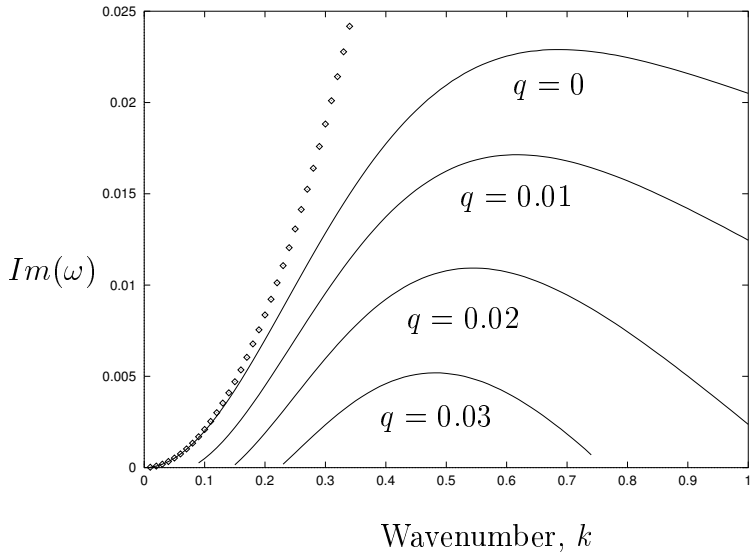

Figure 5.6: Growth rate plotted against wavenumber for an increasingly 'blurred' C profile. $W = 4$, $\overline{C} = 4$, $\Delta C = 4$, $\kappa = 0.5$. The long-wave asymptotic growth-rate (quadratic in k) for $q = 0$, from section 5.3.2 (table (5.29)), is shown in points. At $q = 0.04$ the eigenvalue has ceased to exist.

5.5 Conclusions

We have studied a fluid which models a suspension of microscopic dumbbells whose concentration C varies. This concentration is advected with the fluid, *i.e.* cross-streamline diffusion is neglected. If the diffusion were to be taken into account, the increased 'blurring' of the interface could provide a stabilising mechanism. However, a dumbbell diffuses through its own diameter on a timescale determined by Brownian motion, which (like the relaxation time) is order 1. Thus the cross-channel diffusion rate scales as the square of the ratio of dumbbell size to channel width. We have already assumed that this ratio is small in order to use continuum mechanics; for a channel of 1cm and dumbbells of size 1μm, the diffusion rate is of order 10^{-8}. We thus conclude

that diffusion is unimportant here.

For this material, we find similar results to those for the (less physical but analytically more tractable) fluid of chapter 4. As the unstable interface between two fluids is 'blurred', the growth rate of the instability decreases, and finally the mode ceases to exist. Waves having wavelengths comparable to the channel width survive the longest in this process.

The important result of this chapter is evidence of an elastic instability in a fluid with no sharp interface and no curvature of the base state streamlines; and for which there is a sound physical basis.

We are not aware of any experiment in which the concentration of polymer across a channel has been deliberately varied. Such experiments would be of interest. Our calculation suggests that steep concentration gradients must be included if our instability is to arise; concentration gradients due to imperfect upstream mixing are unlikely to be sufficient.

The analysis of this chapter has a bearing on a proposed mechanism for the sharkskin instability described in section 1.4.5. Chen & Joseph [36] suggest that the high stresses near the wall can cause the polymer molecules to migrate inwards, creating a depleted wall region. They then propose that the interface dividing this region from the bulk of the fluid would be subject to an interfacial instability of the type discussed in chapter 3 and section 5.3.2.

Our analysis shows that a thin outer layer with lower viscosity than the bulk will be stable to long waves in the absence of inertia, and that a small amount of 'blurring' of the interface will stabilise short waves. An interface created by migration will never be truly sharp, and therefore the purely elastic instability mechanism they propose could not occur in practice, at

least on a continuum scale.

5.6 Appendix: Details of the expansion for long waves

In this section, we show the full details of the asymptotic expansion used in section 5.3.2.

Leading order calculation

In the base state:

$$P_0 = \frac{-2(1+C_1)(1+C_2)}{g(\kappa^2, 1+C_1, 1+C_2)} \tag{5.47}$$

where $g(\chi, \phi_1, \phi_2) \equiv \chi\phi_1 + (1-\chi)\phi_2$.

Then at leading order, for a sinuous mode:

$$\psi_0 = \frac{\zeta[U']}{2g(\kappa, 1+C_1, 1+C_2)} \begin{cases} (1+C_2)(y-1)^2 & y > \kappa \\ (1+C_2)(\kappa-1)^2 + (1+C_1)(y^2-\kappa^2) & y < \kappa \end{cases} \tag{5.48}$$

where:

$$[U'] = P_0\kappa\left[\frac{1}{(1+C)}\right] = \frac{2\zeta\kappa(C_1-C_2)}{g(\kappa^2, 1+C_1, 1+C_2)}. \tag{5.49}$$

Hence:

$$\frac{\psi_0(\kappa)}{\zeta} = \frac{(1+C_2)\kappa(1-\kappa)^2(C_1-C_2)}{g(\kappa, 1+C_1, 1+C_2)g(\kappa^2, 1+C_1, 1+C_2)} \tag{5.50}$$

and:

$$\omega_1 = \frac{(1+C_2)(1-\kappa^2)}{g(\kappa^2, 1+C_1, 1+C_2)} + \frac{(1+C_2)\kappa(1-\kappa)^2(C_1-C_2)}{g(\kappa, 1+C_1, 1+C_2)g(\kappa^2, 1+C_1, 1+C_2)}. \tag{5.51}$$

For reference, we note that at the interface:

$$\psi_0 = \frac{\zeta[U']}{2g(\kappa, 1+C_1, 1+C_2)}(1+C_2)(\kappa-1)^2 \tag{5.52}$$

$$\psi_0' = \frac{\zeta[U']}{g(\kappa, 1+C_1, 1+C_2)} \begin{cases} (1+C_2)(\kappa-1) & y=\kappa_+ \\ (1+C_1)\kappa & y=\kappa_- \end{cases} \tag{5.53}$$

$$\psi_0'' = \frac{\zeta[U']}{g(\kappa, 1+C_1, 1+C_2)} \begin{cases} (1+C_2) & y=\kappa_+ \\ (1+C_1) & y=\kappa_- \end{cases} \tag{5.54}$$

$$\psi_0''' = 0. \tag{5.55}$$

Order k calculation

The quantities involved in the jump conditions at order k are:

$$[(1+C)\psi_1''']_\kappa = \frac{-iWP_0\zeta[U']}{g(\kappa, 1+C_1, 1+C_2)} C_1 \frac{(1+C_2)}{(1+C_1)} \tag{5.56}$$

and:

$$[(1+C)\psi_1'']_\kappa = \frac{-iWP_0(1+C_2)^2\zeta[U'](\kappa-1)^2}{2g(\kappa, 1+C_1, 1+C_2)^2}\left(\frac{C_1}{(1+C_1)} - \frac{C_2}{(1+C_2)}\right)$$
$$- 2iWP_0\kappa\zeta[U'] + \frac{2iWP_0\kappa\zeta[U']g(\kappa, (1+C_1)^2, (1+C_2)^2)}{g(\kappa, 1+C_1, 1+C_2)(1+C_1)(1+C_2)} + i\zeta[\Sigma_{11}] \tag{5.57}$$

where:

$$\begin{aligned}[\Sigma_{11}] &= 2WP_0^2\kappa^2[C/(1+C)^2] \\ &= \frac{8W\kappa^2(C_1(1+C_2)^2 - C_2(1+C_1)^2)}{g(\kappa^2, 1+C_1, 1+C_2)^2}. \end{aligned} \tag{5.58}$$

We denote:

$$[(1+C)\psi_1'']_\kappa = i\zeta M_0[U'] + i\zeta[\Sigma_{11}] \tag{5.59}$$

$$[(1+C)\psi_1''']_\kappa = -i\zeta M_1[U'](1+C_1) \tag{5.60}$$

to obtain:

$$\begin{aligned}\psi_1 = \frac{i\zeta(M_0[U'] + [\Sigma_{11}])}{2g(\kappa, 1+C_1, 1+C_2)} &\begin{cases} \kappa(y-1)^2 \\ \kappa(\kappa-1)^2 + (\kappa-1)(y^2-\kappa^2) \end{cases} + \\ \frac{M_1 i\zeta[U']}{6} &\begin{cases} 3(\kappa-1)(y-1)^2 - (y-1)^3 \\ 2(\kappa-1)^3 \end{cases} + \\ \frac{M_1 i\zeta[U'](\kappa-1)^2}{4g(\kappa, 1+C_1, 1+C_2)} &\begin{cases} (1+C_2)(y-1)^2 & y > \kappa \\ (1+C_2)(\kappa-1)^2 + (1+C_1)(y^2-\kappa^2) & y < \kappa \end{cases} \end{aligned} \tag{5.61}$$

and therefore:

$$\begin{aligned}\psi_1(\kappa) = i\zeta \Bigg(&\tfrac{1}{2}\kappa(\kappa-1)^2 \frac{M_0[U'] + [\Sigma_{11}]}{g(\kappa, 1+C_1, 1+C_2)} + \tfrac{1}{3}(\kappa-1)^3 M_1[U'] + \\ &\tfrac{1}{4}(\kappa-1)^4 \frac{M_1[U'](1+C_2)}{g(\kappa, 1+C_1, 1+C_2)} \Bigg). \end{aligned} \tag{5.62}$$

Growth rate

The growth rate, which occurs at order k^2, is:

$$\sigma = k^2 \left(\tfrac{1}{2}\kappa(\kappa-1)^2 \frac{M_0[U'] + [\Sigma_{11}]}{g(\kappa, 1+C_1, 1+C_2)} + \tfrac{1}{3}(\kappa-1)^3 M_1[U'] + \tfrac{1}{4}(\kappa-1)^4 \frac{M_1[U'](1+C_2)}{g(\kappa, 1+C_1, 1+C_2)} \right) \quad (5.63)$$

where:

$$M_0 = \frac{-WP_0(1+C_2)^2(\kappa-1)^2}{2g(\kappa, 1+C_1, 1+C_2)^2} \left(\frac{C_1}{(1+C_1)} - \frac{C_2}{(1+C_2)} \right) - 2WP_0\kappa + \frac{2WP_0\kappa g(\kappa, (1+C_1)^2, (1+C_2)^2)}{g(\kappa, 1+C_1, 1+C_2)(1+C_1)(1+C_2)} \quad (5.64)$$

$$M_1 = \frac{WP_0}{g(\kappa, 1+C_1, 1+C_2)} \frac{C_1(1+C_2)}{(1+C_1)^2} \quad (5.65)$$

$$[U'] = P_0\kappa \left(\frac{1}{(1+C_1)} - \frac{1}{(1+C_2)} \right) \quad (5.66)$$

$$[\Sigma_{11}] = 2WP_0^2\kappa^2 \left(\frac{C_1}{(1+C_1)^2} - \frac{C_2}{(1+C_2)^2} \right) \quad (5.67)$$

and:

$$P_0 = \frac{-2(1+C_1)(1+C_2)}{g(\kappa^2, 1+C_1, 1+C_2)} \quad (5.68)$$

as stated in section 5.3.2.

Chapter 6

Channel Flows of a White-Metzner Fluid

6.1 Introduction

In chapters 4 and 5, we demonstrated the instability of channel flows for two forms of generalised Oldroyd-B fluid, with a mechanism depending on gradients or jumps in the first normal stress difference, N_1. We referred to this as a 'coextrusion' instability, and noted that it will only occur if the gradient in N_1 is large.

We now consider a more realistic constitutive equation for a polymer melt: one which will show a shear-thinning viscosity, while also having gradients in N_1. The *White-Metzner* fluid has these properties, and in addition specialises to a fluid we have already studied, which therefore provides a helpful reference point for numerical studies. We define the fluid by setting $\mu = 0$, $C = 1$ and $c = \varpi = 0$, in the formulation of chapter 2. In other words, there is no solvent viscosity or variation in the elasticity parameter W. There remains at our disposal the choice of the shear dependent viscosity.

The simplest mathematical form of stress as a function of shear-rate which shows shear-thinning is a power-law:

$$\sigma_{12} = \tau\dot{\gamma} = W\dot{\gamma}^n \tag{6.1}$$

where $0 < n \leq 1$. Note that, although σ_{12} is well-defined everywhere, its derivative may not exist at $\dot{\gamma} = 0$, and furthermore $\tau = W\dot{\gamma}^{n-1}$ has a singularity at $\dot{\gamma} = 0$ for $n < 1$. This technical difficulty is discussed further in section 6.2.2. It could be remedied by using (say) a Carreau viscosity function (defined in section 1.3.9), but only at the cost of introducing at least one more dimensionless group, and this is a course we prefer not to take here.

In the special case $n = 1$, we recover the UCM fluid.

In a simple shear flow where $\boldsymbol{u} = (\dot{\gamma}y, 0)$, the White-Metzner model has the stress:

$$\boldsymbol{\sigma} = \begin{pmatrix} -p + 1/W + 2W\dot{\gamma}^{2n} & \dot{\gamma}^n \\ \dot{\gamma}^n & -p + 1/W \end{pmatrix}. \tag{6.2}$$

6.2 Governing equations for a channel flow

6.2.1 Statement of the equations

The base flow is given by chapter 2 as:

$$U(y) = 1 - y^{(n+1)/n}. \tag{6.3}$$

The remaining base state variables are then:

$$\dot{\gamma}_0 = |U'| = -U' = \left(\tfrac{n+1}{n}\right) y^{1/n} \tag{6.4}$$

$$\tau_0 = W \left(\tfrac{n+1}{n}\right)^{n-1} y^{(n-1)/n} \tag{6.5}$$

$$\boldsymbol{A} = \begin{pmatrix} 1 + 2\left(\tfrac{n+1}{n}\right)^{2n} W^2 y^2 & -\left(\tfrac{n+1}{n}\right)^{n} W y \\ -\left(\tfrac{n+1}{n}\right)^{n} W y & 1 \end{pmatrix} \tag{6.6}$$

$$P = P_\infty + 1/W + P_0 x \tag{6.7}$$

$$\boldsymbol{\Sigma} = \begin{pmatrix} -P_\infty - P_0 x + 2W P_0^2 y^2 & P_0 y \\ P_0 y & -P_\infty - P_0 x \end{pmatrix} \tag{6.8}$$

$$P_0 = -\left(\tfrac{n+1}{n}\right)^{n}. \tag{6.9}$$

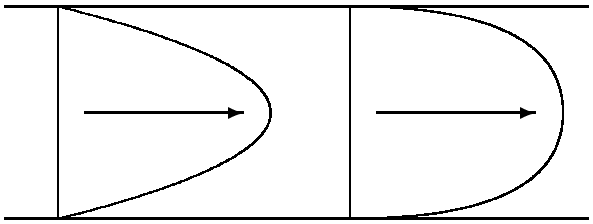

Figure 6.1: Base-flow velocity profile for two values of n. On the left is the parabolic profile of $n = 1$ (a UCM fluid), while a shear-thinning fluid with $n \ll 1$ is on the right.

The velocity profile U is sketched in figure 6.1 for two values of n: for $n = 1$ it is parabolic, because the fluid has a constant viscosity, and for small n it is close to plug-flow through most of the channel, with boundary layers near $y = \pm 1$.

The linearised momentum equations for a perturbation to this flow are, as in section 2.6:

$$ik\sigma_{11} + \sigma'_{12} = 0 \tag{6.10}$$

$$ik\sigma_{12} + \sigma'_{22} = 0 \tag{6.11}$$

$$\sigma_{11} = -p + \frac{1}{W}a_{11} \tag{6.12}$$

$$\sigma_{12} = \frac{1}{W}a_{12} \tag{6.13}$$

$$\sigma_{22} = -p + \frac{1}{W}a_{22}. \tag{6.14}$$

The pressure p may be eliminated from equations (6.10) – (6.14) to give a vorticity equation:

$$a''_{12} + k^2 a_{12} + ik(a'_{11} - a'_{22}) = 0. \tag{6.15}$$

The evolution equations for the perturbations $\boldsymbol{a}$ are:

$$\left(-i\omega + ikU + \frac{1}{\tau_0}\right) a_{11} = ik\psi A'_{11} + 2A_{12}\psi'' + 2A_{11}ik\psi' + 2U'a_{12} + \frac{\tau_1}{\tau_0^2}(A_{11} - 1) \quad (6.16)$$

$$\left(-i\omega + ikU + \frac{1}{\tau_0}\right) a_{12} = ik\psi A'_{12} + \psi'' + A_{11}k^2\psi + U'a_{22} + \frac{\tau_1}{\tau_0^2}A_{12} \quad (6.17)$$

$$\left(-i\omega + ikU + \frac{1}{\tau_0}\right) a_{22} = -2ik\psi' + 2A_{12}k^2\psi \quad (6.18)$$

where:

$$\tau_0 = W\left(\tfrac{n+1}{n}\right)^{n-1} y^{(n-1)/n}. \quad (6.19)$$

τ_0 is the relaxation time associated with the base state, and τ_1 is its perturbation value, given as:

$$\tau_1 = -W(n-1)\left(\tfrac{n+1}{n}\right)^{n-2} y^{(n-2)/n}(\psi'' + k^2\psi). \quad (6.20)$$

Finally the boundary conditions become:

$$\psi(1) = \psi'(1) = 0 \quad (6.21)$$

$$\text{Sinuous } \psi'(0) = \psi'''(0) = 0 \quad (6.22\text{s})$$

$$\text{Varicose } \psi(0) = \psi''(0) = 0. \quad (6.22\text{v})$$

Our aim, as usual, is to determine the eigenvalue ω for a nontrivial solution to this set of equations.

It is notoriously easy to generate spurious numerical instabilities from equations of this kind. We therefore start by constructing asymptotic approximations against which our numerics can be checked. In addition, the availability of well-known solutions for $n = 1$ provides further checks to our results.

6.2.2 A mathematical difficulty

In forming a single equation for ψ from the governing equations (6.15) – (6.20), we would have to take derivatives of the term $(-i\omega + ikU + \frac{1}{\tau_0})$, which will involve derivatives of $y^{(1-n)/n}$. This will give terms proportional to $y^{(1-2n)/n}$ and to $y^{(1-3n)/n}$, which can cause a problem near the centre-line $y = 0$ if $n \neq 1$.

Physically, this difficulty is caused by the form of the relaxation-function (which also acts as shear viscosity):

$$\tau(\dot{\gamma}) = W\dot{\gamma}^{n-1} \tag{6.23}$$

which is non-smooth at $\dot{\gamma} = 0$. When we impose a base-state shear-rate $\dot{\gamma}_0$ and add a perturbation $\dot{\gamma}_1$, the resultant relaxation time is:

$$\tau(\dot{\gamma}_0 + \dot{\gamma}_1) = W(\dot{\gamma}_0 + \dot{\gamma}_1)^{n-1} \approx W\dot{\gamma}_0^{n-1} + (n-1)W\dot{\gamma}_0^{n-2}\dot{\gamma}_1 \tag{6.24}$$

expanding as a Taylor series, providing $\dot{\gamma}_0$ is nonzero. Near the centre-line, $\dot{\gamma}_0$ may be smaller than $\dot{\gamma}_1$, and the principle of linearisation breaks down.

We note however that the perturbation to the shear-rate, $\dot{\gamma}_1$, is proportional to $\psi'' + k^2\psi$. For a varicose mode, ψ is an odd function of y and so $\dot{\gamma}_1 = 0$ at the channel centre-line. Thus the linearisation is 'rescued', and

the system has a removable singularity at $y = 0$. Numerically, we may start the integration a small distance from the channel centre, and, because the singularity is removable, the magnitude of this distance does not affect the results.

For a sinuous mode, however, the singularity is not removable, and if a numerical 'patch' is introduced (or equivalently a Carreau viscosity function is used), the size of the patch has a marked effect on the results, particularly as $n \to 1_-$. Therefore, for the remainder of this chapter, we will consider varicose modes only, satisfying equation (6.22v).

6.3 Long waves

In the long-wave limit, as $k \to 0$, we expand ψ in powers of k. It is convenient to rescale the Weissenberg number W by the wall shear-rate $\dot{\gamma}_{\mathrm{w}} = (n+1)/n$ to give $\mathcal{W} = \tau_{\mathrm{wall}} = W((n+1)/n)^{n-1}$; note that this gives us $\mathcal{W} = W$ when $n = 1$. The leading- and first-order calculations are summarised here.

6.3.1 Order 1 calculation

From integration of equation (6.15) and substitution of equation (6.17), we obtain:

$$\psi_0'' = (A_0 + B_0 y)\left(-i\omega_0 + \frac{y^{(1-n)/n}}{\mathcal{W}}\right) \tag{6.25}$$

where A_0 and B_0 are constants of integration. For varicose modes, ψ must be an odd function of y, so the condition at $y = 0$ gives $A_0 = 0$. Because the equation is linear, we may set $B_0 = 1$ without loss of generality. We are

looking for a solution of equation (6.25) satisfying $\psi(0) = 0$, $\psi(1) = 0$ and $\psi'(1) = 0$.

Integrating twice and applying the ψ' condition at $y = 1$, and ψ at $y = 0$, gives:

$$\psi_0 = -i\omega_0(\tfrac{1}{6}y^3 - \tfrac{1}{2}y) + \frac{n(ny^{(2n+1)/n} - (2n+1)y)}{\mathcal{W}(n+1)(2n+1)}. \tag{6.26}$$

Finally, the condition on ψ at $y = 1$ yields:

$$\omega_0 = -\frac{i}{\mathcal{W}}\frac{3n}{2n+1}. \tag{6.27}$$

We have shown that infinitely long waves ($k \to 0$) are stable for all n and W. This eigenvalue corresponds to the pure relaxation mode $-i/W$ in the case $n = 1$.

6.3.2 Order k calculation

Setting $\alpha = (-i\omega + ikU + \tau_0^{-1})$, we write:

$$\omega = \omega_0 + k\omega_1 + O(k^2) \tag{6.28}$$

$$\psi = \psi_0 + k\psi_1 + O(k^2) \tag{6.29}$$

$$\alpha = \alpha_0 + k\alpha_1 + O(k^2) \tag{6.30}$$

$$a_{ij} = a_{ij}^0 + ka_{ij}^1 + O(k^2). \tag{6.31}$$

It may seem counter-intuitive, at first sight, that the growth rate should have a term of order k. Let us consider the transformation $k \to -k$: because the perturbation is of the form $\exp(ikx - i\omega t)$, this corresponds to a physical perturbation of wavelength k^{-1}, in a system in which the x-direction is reversed. Now the real part of ω represents convection of the disturbance, and

the imaginary part represents growth, so we would expect ω_r to be reversed by this transformation, but ω_i to be unchanged. Thus:

$$\omega(-k) = -\omega^r(k) + i\omega^i(k). \tag{6.32}$$

Any mode as defined above:

$$\omega = i\omega_0^i + k(\omega_1^r + i\omega_1^i) \tag{6.33}$$

does not appear to satisfy this condition, if ω_1^i is nonzero. However, the presence of a corresponding mode with complex conjugate term of order k can rescue the situation. If we label such a complex conjugate pair of roots by A and B, then:

$$\begin{aligned} \omega_{\mathrm{A}}(k) &= i\omega_0^i + k(\omega_1^r + i\omega_1^i) \\ \omega_{\mathrm{B}}(k) &= i\omega_0^i + k(\omega_1^r - i\omega_1^i) \\ \omega_{\mathrm{A}}(-k) &= i\omega_0^i - k(\omega_1^r + i\omega_1^i) \\ \omega_{\mathrm{B}}(-k) &= i\omega_0^i - k(\omega_1^r - i\omega_1^i). \end{aligned} \tag{6.34}$$

The growth rate of mode A for negative k is that of mode B for positive k and vice versa. Figure 6.2 shows a sketch of the behaviour of the real and imaginary parts of these roots with k. We conclude that an $O(k)$ term may legitimately appear in ω_i, and indeed this is the behaviour for the UCM model ($n = 1$).

When the leading-order quantities are substituted into the first-order expansion in small k, the result is a third order ODE for ψ_1. If we define $\tilde{\alpha_0} = \mathcal{W}\alpha_0$, $\tilde{\psi_0} = \mathcal{W}\psi_0$, $\tilde{a}_{11}^0 = a_{11}^0/\mathcal{W}$ and $\tilde{a}_{12}^1 = a_{12}^1/\mathcal{W}$, so that all quantities $\tilde{x}$ are independent of $\mathcal{W}$, we obtain an equation whose coefficients are not functions of $\mathcal{W}$. We deduce that the form of ω_1 is a function of n only:

$$\tilde{\alpha_0} = \frac{-3n}{2n+1} + y^{(1-n)/n} \tag{6.35}$$

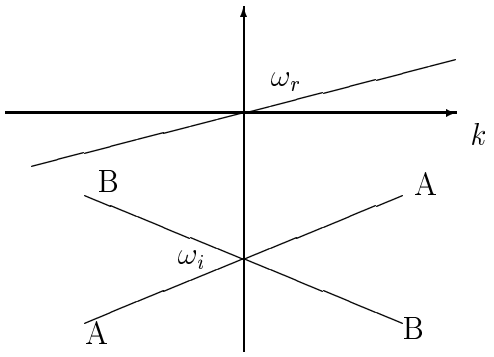

Figure 6.2: Schematic of the behaviour of two complex conjugate roots of the long-wave system, as k moves through positive and negative values.

$$\alpha_1 = -i\omega_1 + i(1 - y^{(n+1)/n}) \tag{6.36}$$

$$\tilde{\alpha_0}\tilde{a}^0_{11} = -2n\left(\frac{n+1}{n}\right) y^{1/n}\frac{\tilde{\psi_0}''}{\tilde{\alpha_0}} - 2n\left(\frac{n+1}{n}\right) y\tilde{\psi_0}'' \tag{6.37}$$

$$\tilde{\alpha_0}\tilde{a}^1_{12} = -\alpha_1 n\frac{\tilde{\psi_0}''}{\tilde{\alpha_0}} - i\left(\frac{n+1}{n}\right)\tilde{\psi_0} + 2i\left(\frac{n+1}{n}\right) y^{1/n}\frac{\tilde{\psi_0}'}{\tilde{\alpha_0}} + n\psi_1'' \tag{6.38}$$

$$(\tilde{a}^1_{12})' + i\tilde{a}^0_{11} = C_0. \tag{6.39}$$

In general we cannot find an analytic solution of these equations, but in the Maxwell limit, $n = 1$, they are soluble. Solution and application of the boundary conditions yields:

$$\mathcal{G}(\omega_1) = 120\omega_1^4 - 95\omega_1^3 + 566\omega_1^2 - 440\omega_1 + 80 + 120\omega_1^2(\omega_1 - 1)^2\sqrt{\omega_1 - 1}\arctan\left(\frac{1}{\sqrt{\omega_1 - 1}}\right) = 0. \tag{6.40}$$

Roots of this equation appear in two complex conjugate pairs:

$$\omega_1 = \begin{cases} 0.29039769 \pm 0.05012283i \\ 0.89882760 \pm 0.12682973i. \end{cases} \tag{6.41}$$

We can demonstrate that no further roots exist by using winding number techniques. $\mathcal{G}$ is analytic in ω away from branch cuts at $0 \leq \omega \leq 1$ and $1 \leq \omega \leq \infty$ on the real axis. These branch cuts are caused by the logarithm inherent in both $\sqrt{\omega}$ and $\arctan(\omega)$, for complex ω.

It is straightforward to check that $\mathcal{G}$ does not have a zero for either $|\omega| \to 0$ or $|\omega| \to \infty$. It follows that the number of roots of $\mathcal{G}$, $N(\mathcal{G})$, is given as:

$$N(\mathcal{G}) = \frac{1}{2\pi i} \oint \frac{\mathcal{G}'(\omega_1)}{\mathcal{G}(\omega_1)} d\omega_1 \tag{6.42}$$

where the integral is performed around the contour shown in figure 6.3.

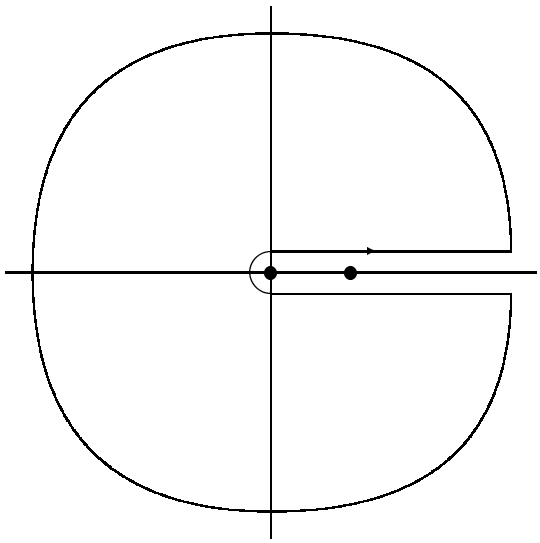

Figure 6.3: The ω_1 plane, showing a schematic of the contour of integration used for determination of the winding number $N(\mathcal{G})$.

The winding number $N(\mathcal{G})$ is the number of times that the function $\mathcal{G}$ goes round the origin as ω_1 traverses the contour of the integral. Plotting $\mathcal{G}$ in the complex plane for values on the contour, and counting the times this curve encircles the origin, gives the number of roots of $\mathcal{G}$. In this case, $N(\mathcal{G}) = 4$.

6.3.3 Long waves and low n

For a highly shear-thinning fluid with $n \to 0$, we consider the joint limit for long waves in which $k \to 0$ and $n \to 0$, with the ratio $\lambda^2 = kW/2n$ constant. We assume that ω will be an order 1 quantity, and check this *a posteriori*.

The full equations are:

$$a_{12}'' + 4\frac{n^2\lambda^4}{W^2}a_{12} + 2i\frac{n\lambda^2}{W}(a_{11}' - a_{22}') = 0 \tag{6.43}$$

$$\left(-i\omega + 2i\frac{n\lambda^2}{W}U + \frac{1}{\tau_0}\right)a_{11} = -2Wyn\psi'' + 8in\lambda^2 Wy\psi + 4i\frac{n\lambda^2}{W}(1 + 2W^2y^2)\psi' + 2U'a_{12} - 8(n-1)\frac{n^2\lambda^4}{W}y\psi \tag{6.44}$$

$$\left(-i\omega + 2i\frac{n\lambda^2}{W}U + \frac{1}{\tau_0}\right)a_{12} = n\psi'' - 2in\lambda^2\psi + U'a_{22} + 4\frac{n^2\lambda^4}{W^2}(n + 2W^2y^2)\psi \tag{6.45}$$

$$\left(-i\omega + 2i\frac{n\lambda^2}{W}U + \frac{1}{\tau_0}\right)a_{22} = -4i\frac{n\lambda^2}{W}\psi' - 8\frac{n^2\lambda^4}{W}y\psi \tag{6.46}$$

$$\tau_0 = Wny^{(n-1)/n}. \tag{6.47}$$

Neglecting all but leading-order terms, we obtain:

$$a_{12}'' = 0 \quad \Longrightarrow \quad a_{12} = Ay + A_1 \tag{6.48}$$

$$\left(-i\omega + \frac{1}{\tau_0}\right) a_{12} = -2in\lambda^2\psi + n\psi'' \tag{6.49}$$

$$\tau_0 = Wny^{(n-1)/n}. \tag{6.50}$$

This leaves us with:

$$-iA\omega y + \frac{Ay^{1/n}}{Wn} = -2i\lambda^2\psi + \psi'' \tag{6.51}$$

which is satisfied to leading order in small n by:

$$\psi = \frac{A\omega}{2\lambda^2}y + \frac{Any^{1/n}}{W} + B\sinh\left((1+i)\lambda y\right) \tag{6.52}$$

in which we have applied the condition that $\psi(0) = 0$.

The wall boundary conditions, $\psi(1) = 0$ and $\psi'(1) = 0$, give:

$$0 = \frac{A\omega}{2\lambda^2} + \frac{A}{W} + B(1+i)\lambda\cosh((1+i)\lambda) \tag{6.53}$$

$$0 = \frac{A\omega}{2\lambda^2} + B\sinh\left((1+i)\lambda\right) + O(n) \tag{6.54}$$

and so:

$$\omega = \frac{1}{W}\frac{2\lambda^2}{(1+i)\lambda\coth\left((1+i)\lambda\right) - 1}. \tag{6.55}$$

In the limit $\lambda \to 0$, or $k \to 0$ for small finite n, this becomes:

$$\omega = -\frac{3i}{W} \tag{6.56}$$

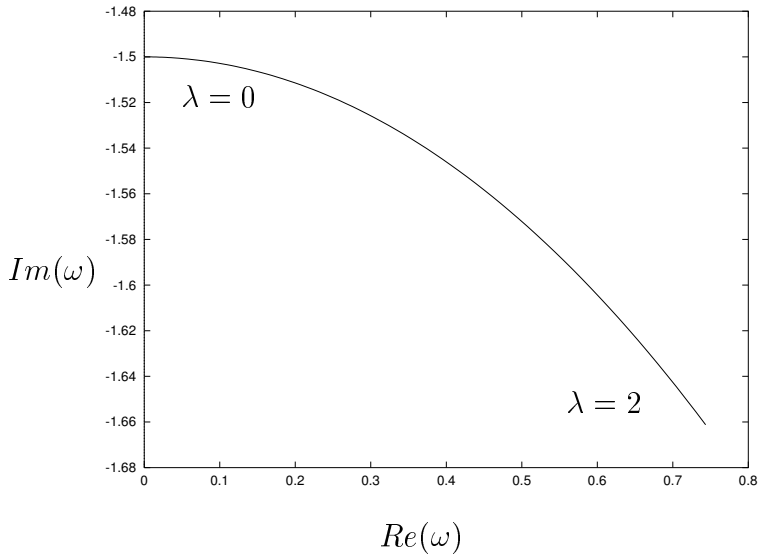

Figure 6.4: Behaviour of ω as λ increases in the long-wave shear-thinning limit of a White-Metzner fluid. The Weissenberg number is $W = 2$. All values of λ give stable ω.

which is indeed the $n \to 0$ limit of the leading-order expression for $k \to 0$, given by equation (6.27) with $\mathcal{W} \sim Wn$.

For other values of λ, ω is shown (in the complex plane) in figure 6.4; the flow is stable for all λ.

A sample plot of the eigenfunction (for the case $\lambda = 1$, $n = 0.01$, and $W = 2$, for which $\omega = 0.199 - 1.511i$) is given in figure 6.5, and the resulting streamlines of the perturbation flow in figure 6.6.

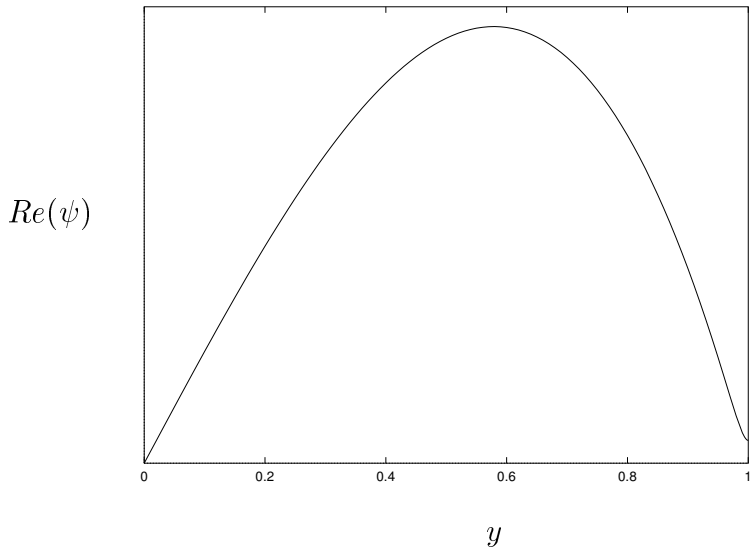

Figure 6.5: Streamfunction ψ plotted across the channel for the long-wave shear-thinning limit of a White-Metzner fluid. The Weissenberg number is $W = 2$, and $n = k = 0.01$, so $\lambda = 1$. The boundary conditions at $y = 1$ are not satisfied exactly, but the error is of order n, compared with the magnitude of ψ in the bulk of the channel.

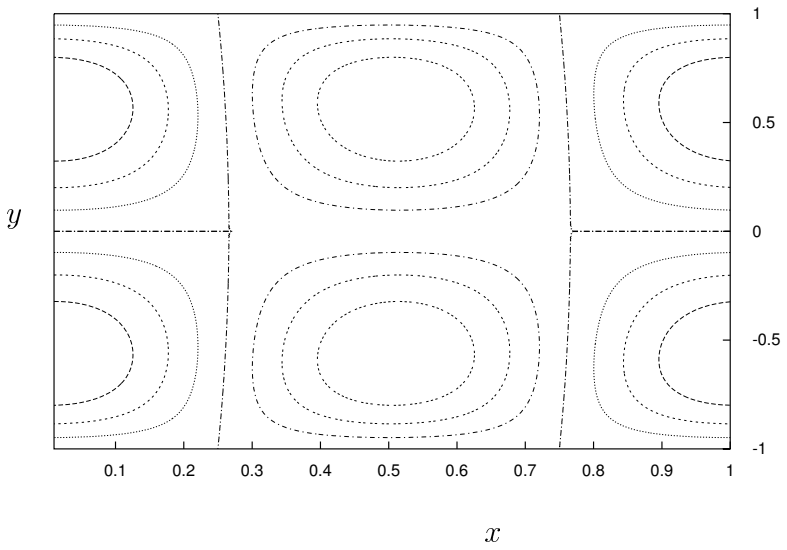

Figure 6.6: Streamlines of the perturbation flow, for the asymptotic limit of low n and low k. The streamfunction is shown in figure 6.5, and the parameter values are $n = k = 0.01$, $W = 2$.

6.4 Short waves

6.4.1 Analytic scalings for short waves

The White-Metzner fluid has no intrinsic lengthscale, like the Maxwell fluid to which it specialises. The only lengthscales in the problem, then, are: the channel width, normalised to 1 in dimensionless form; the wavelength, k^{-1}; and any scale occurring in the base flow.

If we take a very highly shear-thinning fluid ($n \ll 1$), then the base state velocity has steep gradients in a thin layer near the wall. This layer gives a third lengthscale to the flow, given in dimensionless form as n.

For very short waves (shorter than n, if n is small), we expect all the lengths in the problem to scale with the wavelength, k^{-1}, and the disturbance to be localised at some point in the channel.

While it is possible that a mode may be localised anywhere, the distinguished points are near the centre of the channel, and the wall, $y = 1$. We concentrate on wall modes here.

We let $z = k(y-1)$, d denote $\partial/\partial z$, and let $k^{-1} \to 0$. We rescale a_{ij} by a factor of k^2, and as we would expect, the relevant shear-rate is the rate at the wall, $\dot{\gamma}_{\mathrm{w}} = (n+1)/n$. We define the relaxation time at the wall, $\mathcal{W} = \tau(\dot{\gamma}_{\mathrm{w}}) = W((n+1)/n)^{n-1}$ (as we did for the long-wave limit of section 6.3) to obtain:

$$\left(-i\omega - i\dot{\gamma}_{\mathrm{w}} z + \frac{1}{\mathcal{W}}\right) a_{11} = 2i(1 + 2\mathcal{W}^2\dot{\gamma}_{\mathrm{w}}^2)d\psi - 2\mathcal{W}\dot{\gamma}_{\mathrm{w}} n d^2\psi - 2\dot{\gamma}_{\mathrm{w}} a_{12} - 2\mathcal{W}\dot{\gamma}_{\mathrm{w}}(n-1)\psi \quad (6.57)$$

$$\left(-i\omega - i\dot{\gamma}_{\rm w} z + \frac{1}{\mathcal{W}}\right) a_{12} = (1 + 2\mathcal{W}^2\dot{\gamma}_{\rm w}^2)\psi + nd^2\psi - \dot{\gamma}_{\rm w} a_{22} + (n-1)\psi \tag{6.58}$$

$$\left(-i\omega - i\dot{\gamma}_{\rm w} z + \frac{1}{\mathcal{W}}\right) a_{22} = -2\mathcal{W}\dot{\gamma}_{\rm w}\psi - 2id\psi \tag{6.59}$$

$$(d^2 + 1)a_{12} + id(a_{11} - a_{22}) = 0 \tag{6.60}$$

with boundary conditions:

$$\psi(0) = \psi'(0) = 0 \tag{6.61}$$

$$\psi \to 0 \quad \text{as} \quad z \to \infty. \tag{6.62}$$

Note the similarity of these equations to equations (3.35) – (3.38) for the Oldroyd-B fluid of chapter 3, with shear-rate $\dot{\gamma}_{\rm w} = 2\kappa$. This similarity is the reason for using $\mathcal{W}$. Although different boundary conditions are to be applied, the only difference between these equations and those for a Maxwell fluid is the coefficient of the highest derivative, and the final term in equations (6.57) and (6.58). Both these changes come from the perturbation τ_1, caused by the infinitesimal change in effective shear-rate. The equations are, of course, the same as for the Maxwell fluid when $n = 1$.

For the case $n = 1$ (using the eigenfunctions of Gorodtsov & Leonov [71]), the leading-order eigenvalue as $k \to \infty$ is:

$$\omega = \frac{-\dot{\gamma}_{\rm w}}{1 - \beta - i\dot{\gamma}_{\rm w}\mathcal{W}} \tag{6.63}$$

where $\beta = (1 + (\dot{\gamma}_{\rm w}\mathcal{W})^2)^{1/2}$, $\dot{\gamma}_{\rm w} = 2$, $\mathcal{W} = W$ and $\beta > 0$. This root is stable for all values of $\mathcal{W}$.

For other values of n, these equations are not soluble analytically, but as for the case of two Oldroyd-B fluids in chapter 3, we can obtain this short-wave limit numerically.

6.4.2 Numerical results for short waves

In the short-wave limit, a numerical study reveals only one root with the wall-boundary-layer scaling outlined above. This root is known in the limit $n = 1$, and may be continued to lower n.

We note that as $n \to 0$, if we keep the original Weissenberg number W fixed, both $\mathcal{W}^{-1}$ and $\dot{\gamma}_{\rm w}$ become $O(n^{-1})$. Thus, if ω is to have any effect in equations (6.57) – (6.59), we expect $\omega \sim n^{-1}$ as $n \to 0$.

Because $\mathcal{W}$ becomes small as $n \to 0$, we revert here to the original Weissenberg number, W. For any fixed value of W, the root remains stable as n decreases, until n becomes small ($n < 0.2$), when instability may occur, depending on the value of W. Thus sufficiently short waves grow, though at finite rate for any fixed n.

This is a new instability. It differs from the coextrusion instability of chapters 4 and 5. Because it occurs only for small (but finite) n, we refer to it as a *shear-thinning* instability. Two examples ($W = 1$ and $W = 2$) are shown in figures 6.7 and 6.8, and sample streamfunctions from each curve are shown in figure 6.9. Figure 6.10 shows the perturbation streamlines for the unstable mode at $W = 2$, $n = 0.15$. Numerical difficulties occur for smaller n, because of the large values of ω and the high shear-rates involved.

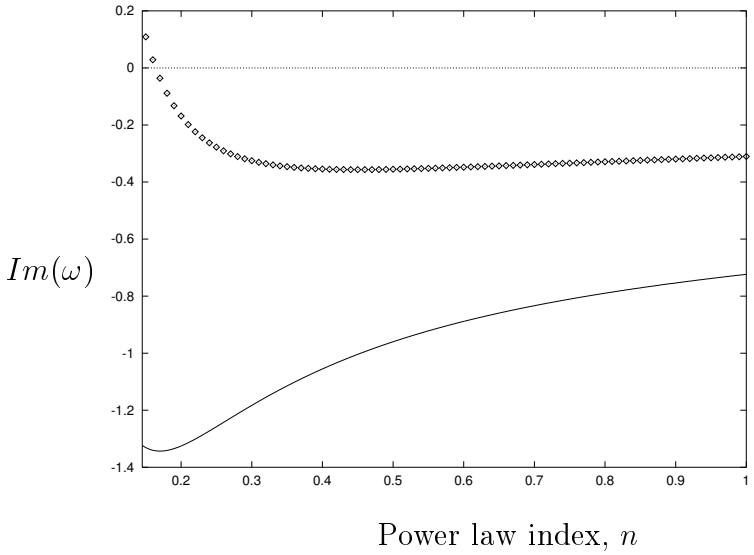

Figure 6.7: Imaginary part of the complex growth rate of short-wave disturbances, plotted against power law index n, for White-Metzner fluids with $W = 1$ (solid line) and $W = 2$ (points). The mode remains stable as long as n is moderate, but instability is observed for $n < 0.2$. The values at $n = 1$ correspond with equation (6.63).

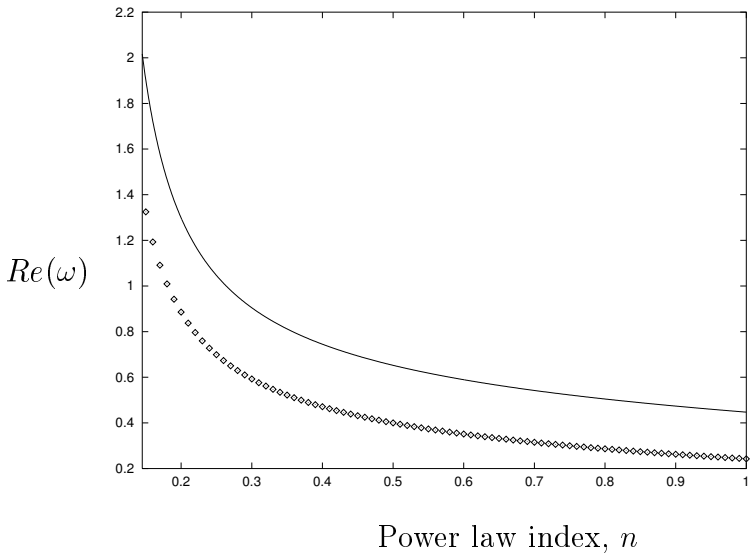

Figure 6.8: Real part of the eigenvalues shown in figure 6.7.

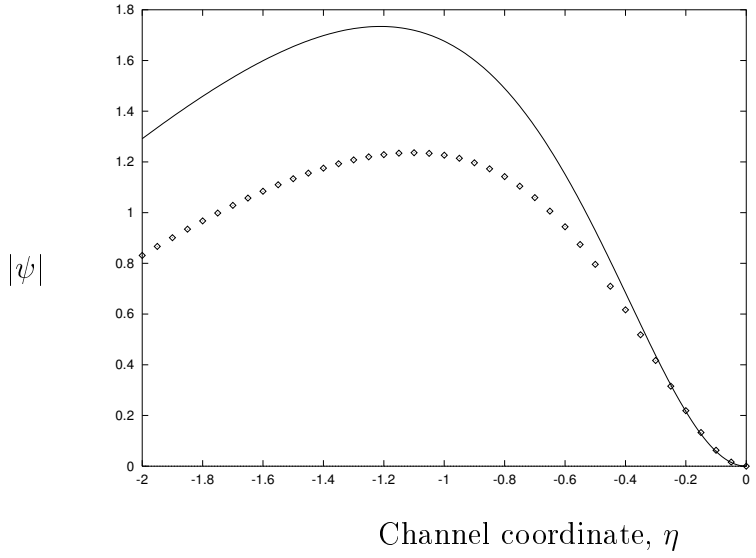

Figure 6.9: The modulus of the complex streamfunction, $|\psi|$, plotted across the boundary-layer. Both functions are for a value of $n = 0.15$. The solid lines are for a stable case, $W = 1$, and the points for an unstable case, $W = 2$.

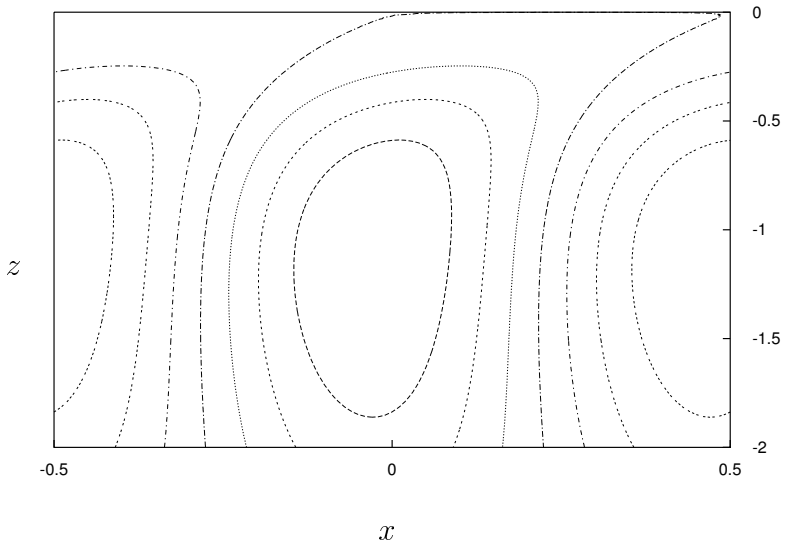

Figure 6.10: Streamlines of the more unstable streamfunction from figure 6.9. The disturbance decays away from the wall (at the top of the picture). $W = 2$, $n = 0.15$.

6.5 Intermediate wavelengths: numerical results

Following the behaviour of roots of ω in the complex plane is difficult and we proceed by parameter continuation. As a first step, therefore, we consider the modes of the UCM fluid ($n = 1$) as k varies.

In this limit, long waves show four stable roots, all coalescing at $k = 0$. These four roots can all be found numerically, and may be analytically continued into the régime of finite k. As figure 6.11 shows, one of these roots ceases to exist at $k \approx 0.4$. This is because the problem has a continuous spectrum (which is stable), a branch cut in the ω-plane. This is a non-analytic region, and so analytic continuation is invalid. The disappearing root (we shall refer to it as root A) enters the continuous spectrum at the branch point, where $k \approx 0.4$.

Of the three roots which exist for high k, only one (root B) matches the short-wave asymptotics of section 6.4. This is because the others do not obey our assumed scaling, but rather have $\omega \sim k + O(1)$ as $k \to \infty$. In other words, they become concentrated around the centre-line, rather than the wall. This limit has not been studied, because of the singularity in the White-Metzner fluid at zero shear-rate. However, the Maxwell fluid is well-posed for the entire channel, and for that case these two decaying roots are acceptable physical modes. In the very short-wave limit, they are confined within a central region of plug-flow, and represent the stable response of the fluid to small perturbations about a state of rest.

Turning now to the more general problem in which $n \neq 1$, there is

still a continuous spectrum of modes, located at $y = y_0$, where the factor $(-i\omega + ik(1 - y_0^{(n+1)/n}) + \tau_0^{-1})$ is zero:

$$\left\{ \omega = k(1 - y_0^{(n+1)/n}) - \frac{i}{W}\left[\frac{(n+1)}{n} y_0^{1/n}\right]^{1-n} \; ; \; \psi = \delta(y - y_0) \right\}. \qquad (6.64)$$

Figure 6.12 shows this spectrum in the ω-plane for $W = 2$, $k = 1$ for a few illustrative values of n. We note that the extreme values of the continuous spectrum are given by $y_0 = 1$, for which:

$$\omega = -\frac{i}{W}\left(\frac{n+1}{n}\right)^{1-n} \qquad (6.65)$$

and $y_0 = 0$, for which (unless $n = 1$):

$$\omega = k. \qquad (6.66)$$

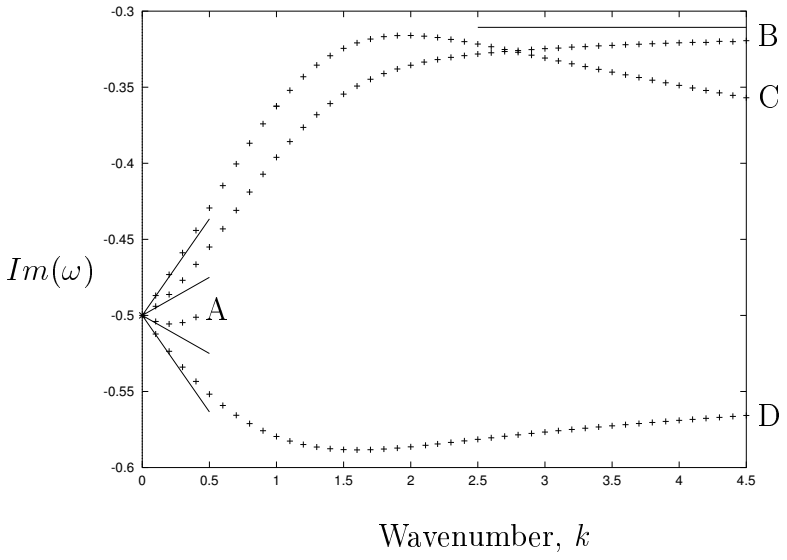

Figure 6.11: Growth rates plotted against wavenumber k, for an Upper-Convected Maxwell fluid with $W = 2$. The long-wave ($k \to 0$) asymptotes shown are calculated in section 6.3, and the short-wave limit in section 6.4.

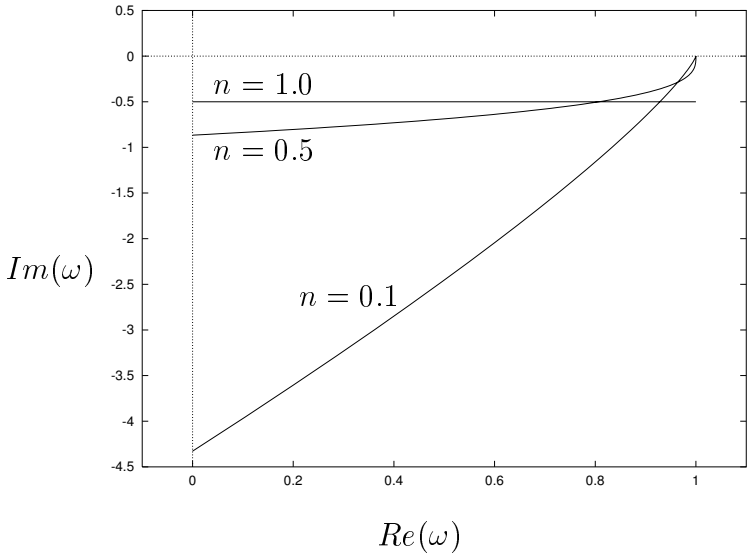

Figure 6.12: The continuous spectrum (in the ω-plane) for a White-Metzner fluid. $W = 2$ and $k = 1$; three different values of n are shown.

Because the continuous spectrum reaches the line of neutral stability whenever $n \neq 1$, analytic continuation of roots will only be of limited value. Roots may cease to exist, and this method cannot guarantee to find all acceptable roots of the dispersion relation.

As an illustration, figures 6.13 and 6.14 show all the roots we have found for ω as n varies, when $W = k = 2$. There are four roots which are highly unstable for small n (B, E, F and G), only one of which (root B) continues in n up to $n = 1$. Another root, H, is weakly unstable, and also disappears at a critical value of n. We know the four roots (A, B, C and D, as defined in figure 6.11) at $n = 1$; only two of them, A and B, continue to exist for small n. Root A was first continued downward in n at lower k before moving to $k = 2$, and continues to exist and is stable beyond the scale of figure 6.13 when n is small.

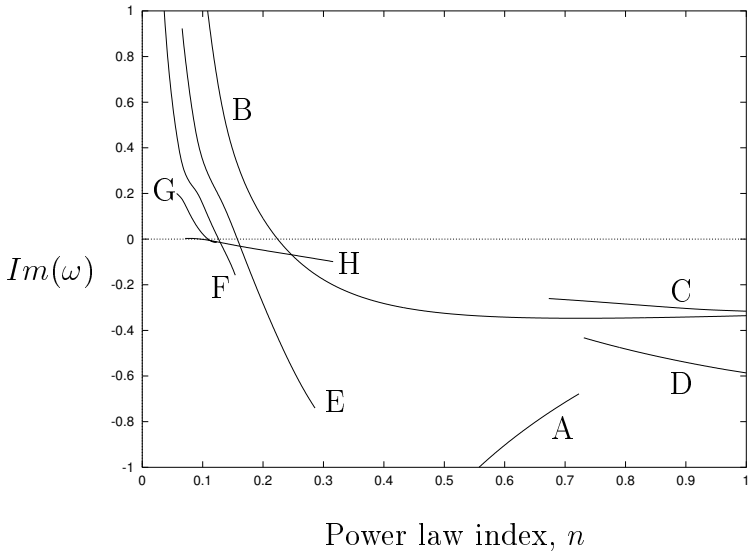

Figure 6.13: Plot of the growth rate against power-law index of roots found numerically, for the White-Metzner fluid. $W = k = 2$.

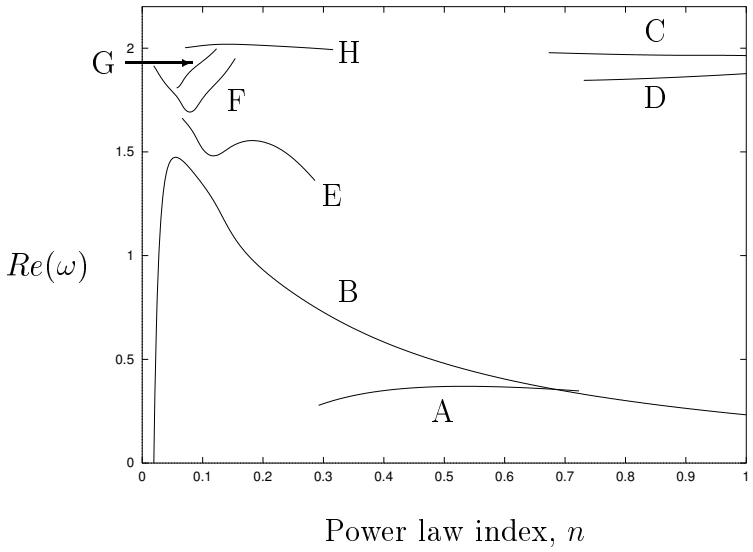

Figure 6.14: Plot of the real part of the eigenvalues shown in figure 6.13.

We are unable to continue our calculation to very small n. The difficulty is numerical. As $n \to 0$, the equations become singular, and the streamfunction derivatives increasingly large. Small errors in the function values are amplified by the integration until they swamp the true value, and no root can be found[1].

It is interesting to consider the asymptotic behaviour of these four roots as $n \to 0$. At first glance, the growth rate $Im(\omega)$ seems to be growing without bound, at least for the most unstable root, B. However, plotting this root logarithmically (both as $\log(Im(\omega))$ against n, and as $\log(Im(\omega))$ against $\log n$), it becomes clear that the root is in fact exponential in n, and is therefore bounded (though large) as $n \to 0$. Since we expect very short waves to grow at rate $Im(\omega) \sim n^{-1}$ as $n \to 0$, this bounded growth rate can only apply to any fixed, finite value of the wavenumber, k. Figure 6.15 shows the best power-law fit and the best exponential fit to the imaginary part of root B. Its real part (shown in figure 6.14) starts to change rapidly shortly before the calculation fails. The region of this variation is too short to show conclusively whether this change is of power-law or exponential form. Thus we cannot tell whether or not the real part of ω stays bounded as $n \to 0$.

The other three strongly unstable roots, E, F and G, are similar to one another. Figure 6.14 shows that they have bounded real parts as $n \to 0$, and their imaginary parts are also bounded, consistent with exponential growth rates as for root B.

In figure 6.16, we show the shape of typical unstable eigenfunctions. The

[1]Spurious numerical roots, of the type outlined in section 2.9, are sometimes found, but these are not roots of the dispersion relation.

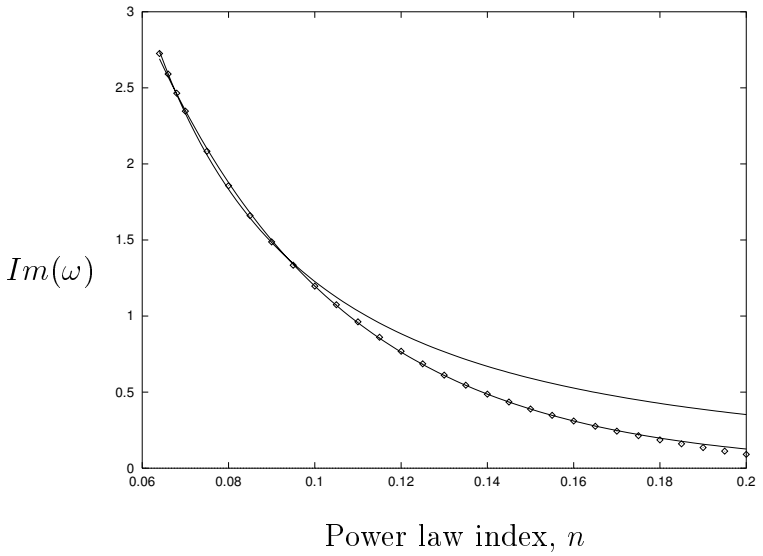

Figure 6.15: Plot of the low n behaviour of the growth rate of root B, for a White-Metzner fluid with $W = k = 2$. The points show the numerical data, while the two solid curves are the best power-law and exponential fits. The exponential curve $Im(\omega) \sim 11.4\, e^{(-22.5n)}$ gives the better fit.

two curves shown are for $n = 0.1$ and $n = 0.2$, allowing some insight into the dependence of the streamfunction shape on n. The scalings of this function will be discussed in section 6.6. Figure 6.17 shows the perturbation streamlines associated with the $n = 0.1$ curve of figure 6.16.

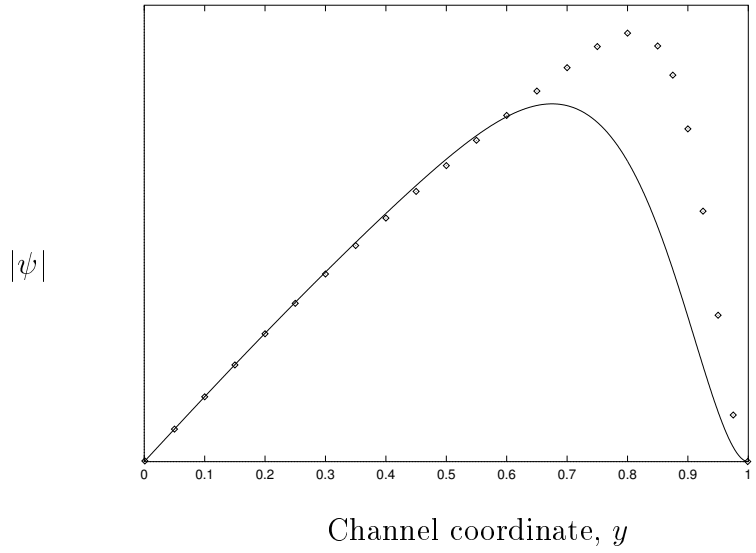

Figure 6.16: Two typical eigenfunctions for small values of n. The modulus of the streamfunction is plotted, for root B, at $W = 2$, $k = 2$. The solid line is for $n = 0.2$, and the points for $n = 0.1$.

To complete the picture of this instability, a study of its wavenumber-dependence is needed. For no values of k and W did we find instability for $n > 0.3$. We choose two representative sets of parameter values: $n = 0.1$, $W = 2$, for which all five of the unstable modes we have found are present and short waves are also unstable; and $n = 0.2$, $W = 2$, for which short waves are known to be stable, and only three modes have been found at $k = 2$.

Figures 6.18 and 6.19 show the imaginary and real parts of the five roots at $n = 0.1$. The most unstable of these corresponds to the known short-wave

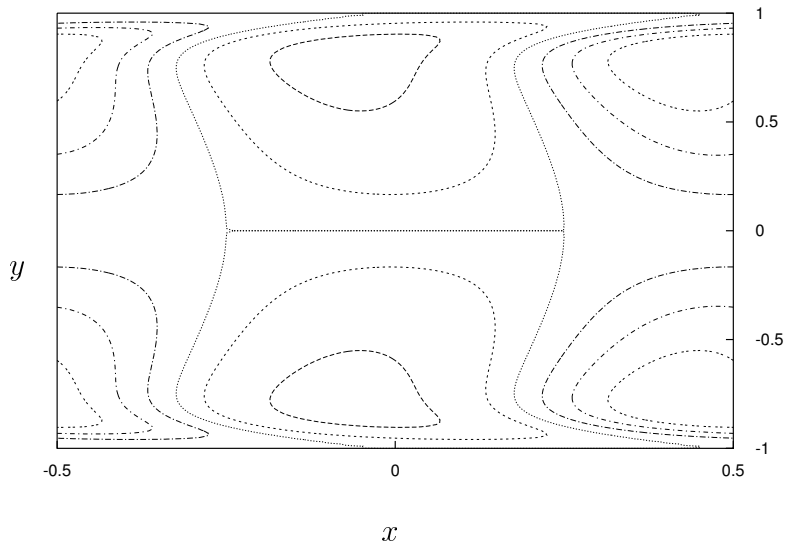

Figure 6.17: Streamlines of the perturbation flow for an unstable White-Metzner fluid. $W = 2$, $k = 2$, and $n = 0.1$. The mode chosen is root B. Much of the variation in the flow takes place close to the wall.

root as $k \to \infty$, and to the known long-wave root as $k \to 0$. The other four roots cease to exist when the waves become long (k small), by merging into the continuous spectrum. For this case, the most unstable disturbance is a short wave.

Three of the five roots in figures 6.18 and 6.19, roots B, E and F, are sufficiently widely spaced to be clearly distinguishable on the plot, but the other two, roots G and H, are very close together. In fact, they are close to a mode-crossing point, as their behaviour demonstrates (shown on a larger scale in figures 6.20 and 6.21).

Finally, the three roots at $n = 0.2$ are shown in figures 6.22 and 6.23. In this case, the most unstable disturbance has k of order unity. The corresponding eigenfunction is shown in figure 6.24.

6.6 Highly shear-thinning limit, $n \to 0$

From the numerical studies of sections 6.4.2 and 6.5, we observe that very highly shear-thinning fluids with $n \ll 1$ can show instability. We would therefore like to understand the scalings appropriate for the case in which $n \to 0$.

The highest derivative in the perturbation equations, ψ'''', which comes from a_{12}'', has a coefficient proportional to n. This is because the perturbation shear stress is of order $n\psi''$. The equations are not regular in the limit $n \to 0$, and therefore we expect some kind of boundary-layer structure to emerge in this limit. Indeed, as $n \to 0$, most of the variation in base-state velocity takes place very close to the wall, so we expect to see boundary layers in this

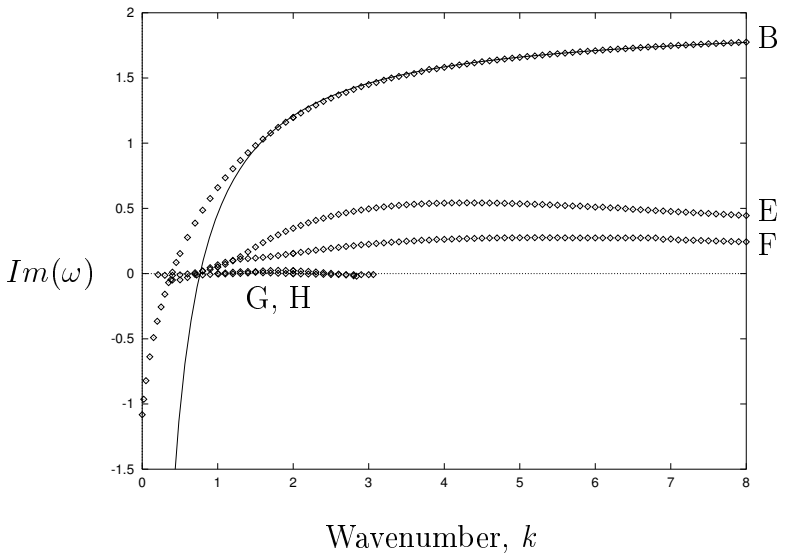

Figure 6.18: The wavenumber-dependence of the growth rate of the five unstable roots, for a White-Metzner fluid with $W = 2$ and $n = 0.1$. The numerical results are all shown as points, and the solid line is an extrapolation of the behaviour of the most unstable root, B, as $k \to \infty$. It is given by $Im(\omega) = Im(\omega_\infty) - 1.5\,k^{-1}$, where ω_∞ is the short-wave root found by the program of section 6.4.

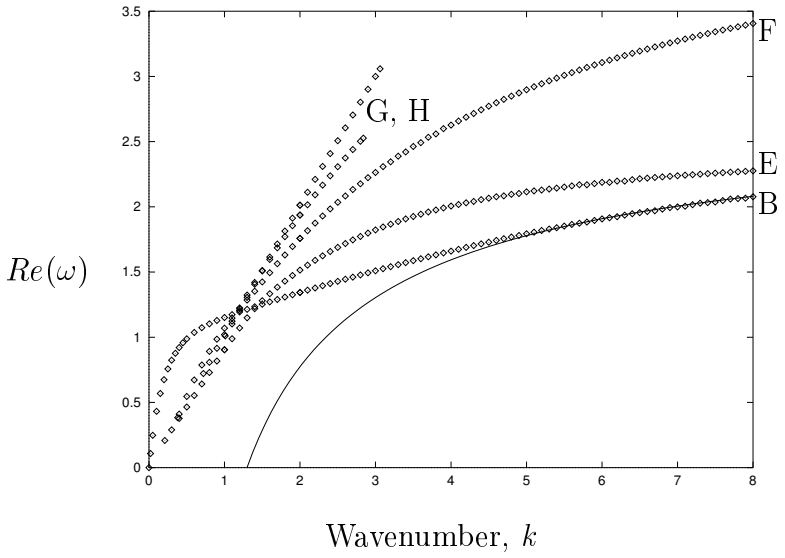

Figure 6.19: The real parts of the eigenvalues shown in figure 6.18. The solid line is an extrapolation of the behaviour of root B, the most unstable root, as $k \to \infty$, matching up with the numerical results for short waves from section 6.4. $W = 2$ and $n = 0.1$.

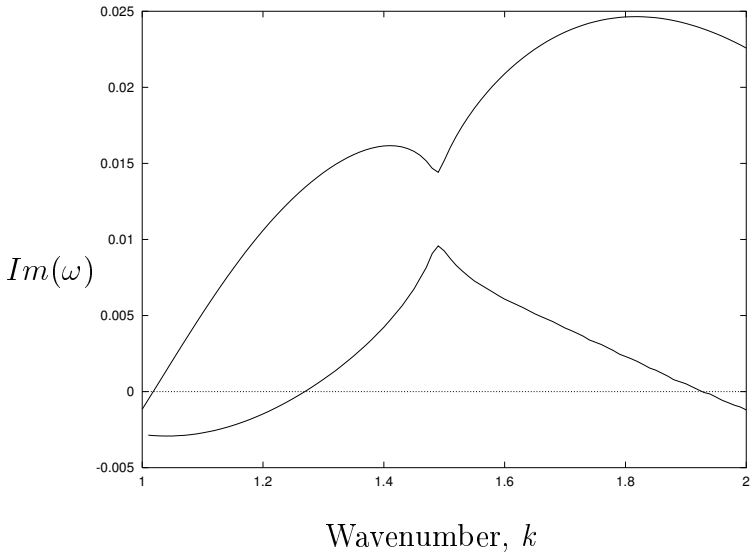

Figure 6.20: Close-up of part of figure 6.18. The two roots shown, roots G and H, are close (in parameter-space) to a point where they cross.

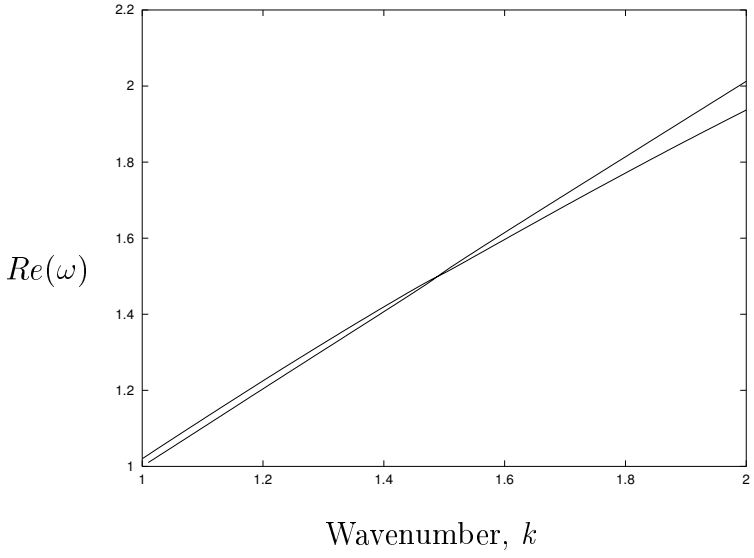

Figure 6.21: The behaviour of the real parts of roots G and H close to their mode-crossing. This plot shows the real part of the curves shown in figure 6.20.

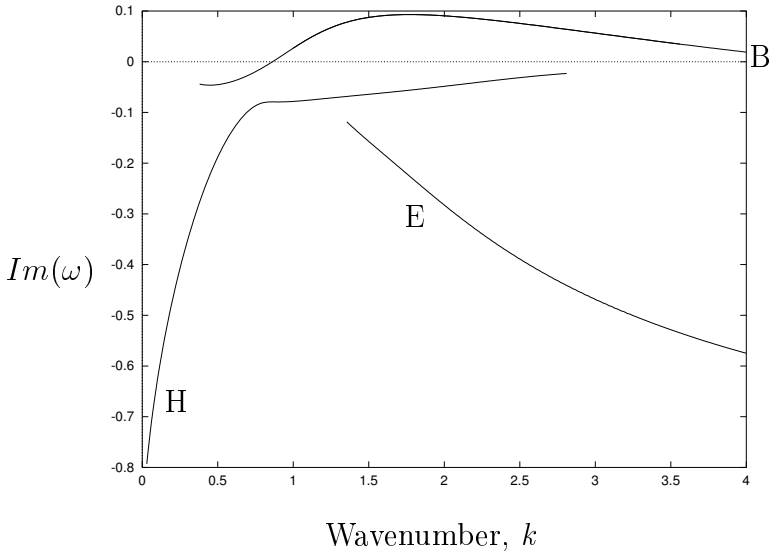

Figure 6.22: The wavenumber-dependence of the growth rate of the three roots, for a White-Metzner fluid with $W = 2$ and $n = 0.2$.

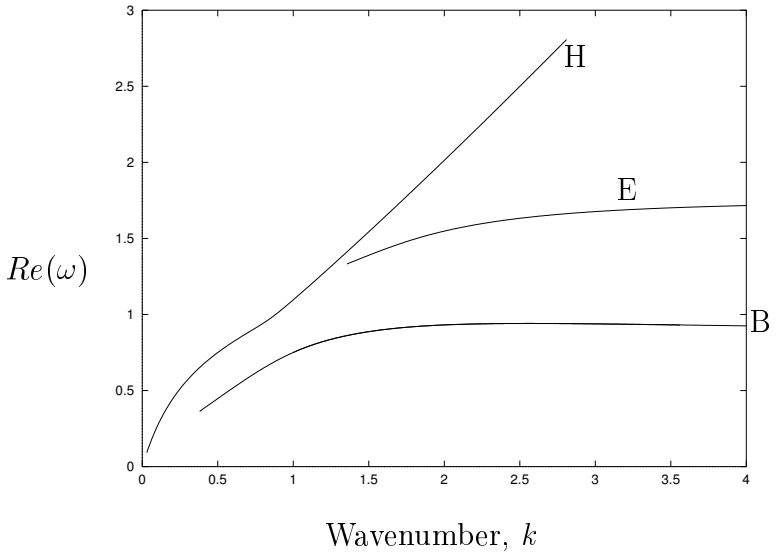

Figure 6.23: The wavenumber-dependence of the convective part of the eigenvalue of the three roots, for a White-Metzner fluid with $W = 2$ and $n = 0.2$. This plot shows the real part of the curves whose imaginary parts are in figure 6.22.

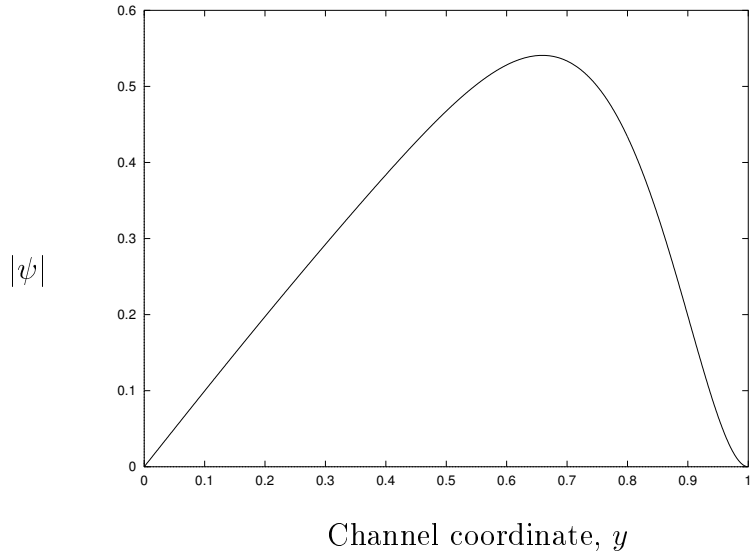

Figure 6.24: The eigenfunction of the most unstable mode, root B, for a White-Metzner fluid with $n = 0.2$ and $W = 2$. The wavenumber is $k = 1.77$, and the modulus of the streamfunction is shown.

region.

We consider the simplification which may be made to the equations in the limit of small n, while still retaining all the terms which are physically (and mathematically) important.

6.6.1 Governing equation

We will consider only the leading order behaviour as $n \to 0$. Throughout this section, there will be an implicit '$+ O(n^{1/2})$' on the right hand side of each equation. We neglect terms which are clearly not of leading order from the full equations for general n to obtain:

$$a_{12}'' + k^2 a_{12} + ik(a_{11}' - a_{22}') = 0 \tag{6.67}$$

$$\alpha = \left(-i\omega + ik + \frac{y^{1/n}}{Wn} \right) \tag{6.68}$$

$$\alpha a_{11} = -2Wyn\psi'' + 2(1 + 2W^2y^2)ik\psi' + (4ikW^2y + 2k^2Wy)\psi - 2a_{12}\frac{y^{1/n}}{n} \tag{6.69}$$

$$\alpha a_{12} = n\psi'' + (2W^2y^2k^2 - ikW)\psi - a_{22}\frac{y^{1/n}}{n} \tag{6.70}$$

$$\alpha a_{22} = -2ik\psi' - 2Wyk^2\psi \tag{6.71}$$

with boundary conditions:

$$\psi(1) = \psi'(1) = 0 \tag{6.72}$$

$$\psi(0) = \psi''(0) = 0. \tag{6.73}$$

Let us first consider the region far from the wall. Here, α is approximately constant, and so because each of the components of $\boldsymbol{a}$ is proportional to α^{-1}, it plays no part in the dynamics of equation (6.67). In order to maintain the shear stress $n\psi''$ at leading order, the flow must vary on a lengthscale of $n^{1/2}$ across the whole channel. This scaling is not obvious in the eigenfunctions of figure 6.16. This is because the values of n, there, are only $n = 0.1$ and $n = 0.2$, *i.e.* $n^{1/2} \approx 0.32$ and $n^{1/2} \approx 0.45$, neither of which is very small. The physical origin of the $n^{1/2}$ lengthscale is that rapid y-variations are required to generate a shear stress of order unity. Since this is likely to be the region of slowest variation of ψ (which we expect to have large derivatives close to the wall), we deduce that a'_{12} is always large compared to a_{12}. This allows us to perform the first integral of the vorticity equation (equivalent to stating that the perturbation pressure is constant across the channel):

$$a'_{12} + ik(a_{11} - a_{22}) = A. \tag{6.74}$$

We now need keep only those terms of a_{11} which may somewhere be as large as a'_{12}. The neglect of many terms is obvious, but we look in detail at the term $(a_{12}y^{1/n})/n$. This needs to be as large as a'_{12} to have an effect, which can only happen if $y^{1/n}/n$ is large. Where $y^{1/n}/n$ *is* large, $\alpha \gtrsim y^{1/n}/(Wn)$ and the term is only as large as a_{12}. Therefore, we neglect it everywhere, and equation (6.69) becomes:

$$\alpha a_{11} = 2(1 + 2W^2y^2)ik\psi'. \tag{6.75}$$

We also observe that:

$$\alpha a_{22} = -2ik\psi'. \tag{6.76}$$

Substituting in, we obtain:

$$a'_{12} + ik(a_{11} - a_{22}) = A \tag{6.77}$$

$$\alpha = \left(-i\omega + ik + \frac{y^{1/n}}{Wn}\right) \tag{6.78}$$

$$\alpha(a_{11} - a_{22}) = 4(1 + W^2y^2)ik\psi' \tag{6.79}$$

$$\alpha a_{12} = n\psi'' + 2ik\psi'\frac{y^{1/n}}{n\alpha} + (2W^2y^2k^2 - ikW)\psi. \tag{6.80}$$

The term $ik(a_{11} - a_{22})$ in the vorticity equation scales as ψ'. For it to have any influence, we need ψ' to be of the same order as $n\psi'''$; in other words, the scale of variation of ψ needs to be no faster than $n^{1/2}$. This can only occur far from the wall, where α is constant, and (since derivatives of ψ are large) we have at leading order:

$$ik(a_{11} - a_{22}) = ik(4(1 + W^2y^2)ik\psi')/\alpha \tag{6.81}$$

$$= \left\{-4(k^2 + W^2k^2y^2)\psi/\alpha\right\}' \tag{6.82}$$

and the vorticity equation becomes:

$$a_{12} = 4(k^2 + W^2k^2y^2)\psi/\alpha + Ay + B. \tag{6.83}$$

We define $\tilde{A} = A(-i\omega + ik)$ and $\tilde{W} = W(-i\omega + ik)$ to obtain:

$$n\psi'' + \frac{2ikW\psi'}{(1 + n\tilde{W}y^{-1/n})} - \Theta^2(y)\psi = \tilde{A}y + Ay\left(\frac{y^{1/n}}{Wn}\right) \tag{6.84}$$

where:

$$\Theta(y) = (4k^2 + ikW + 2W^2k^2y^2)^{1/2} \tag{6.85}$$

with $Re(\Theta) > 0$, and we have applied the boundary conditions at $y = 0$ to obtain $B = 0$. This equation contains all the information about the leading-order dynamics as $n \to 0$. Note that we have not yet made any assumption about the size of ω, except that $|\omega - k|$ is not small.

The boundary conditions are:

$$\psi(1) = \psi'(1) = 0 \tag{6.86}$$

$$\psi(0) = 0. \tag{6.87}$$

We have therefore shown that the $n \to 0$ dynamics are controlled by a second-order ODE (6.84), rather than the full fourth-order ODE (equations (6.10) – (6.20)).

6.6.2 Physical meaning of the reduced equation

In order to begin to understand the mechanism of instability, we need to know the physical origin of the four different terms in equation (6.84). It may be re-expressed as:

$$n\tau_0\psi'' + \frac{2ikW\psi'}{\alpha} - \Theta^2(y)\psi\tau_0 = Ay\tau_0\alpha \tag{6.88}$$

where:

$$\Theta^2(y) = 4k^2 + ikW + k^2N_1 \tag{6.89}$$

and:

$$\alpha = \left(-i\omega + ik + y^{1/n}/(Wn)\right) \tag{6.90}$$

$$= \left(-i\omega + ik + \tau_0^{-1}\right). \tag{6.91}$$

We look in detail at equation (6.88).

- The first term, $n\tau_0\psi''$, comes from the shear stress part of the vorticity equation. The shear stress is $\tau\dot{\gamma} = W\dot{\gamma}^n$, so the perturbation to it is $nW\dot{\gamma}_0^{n-1}\dot{\gamma}_1 = n\tau_0\dot{\gamma}_1$. The perturbation to the shear-rate is $-(\psi'' + k^2\psi)$, so the perturbation shear stress is approximately $-n\tau_0\psi''$.

- The second term comes from the coupling of the evolution of a_{12} to a_{22}. Physically, this coupling occurs even in the Maxwell limit $n = 1$, and corresponds to the effect of the base state shear-rate on the perturbation vorticity.

- The third term, $\Theta^2(y)\tau_0\psi$, is more complicated. It contains contributions from the inelastic part of the stress (the $W \to 0$ limit), from the material convection of A_{12} by the perturbation velocity, and from the base state first normal stress difference N_1.

- Finally, the constant A, which came from integrating the vorticity equation, is the perturbation pressure across the channel.

The form of α shows that there is a wall-layer. In the bulk of the fluid, $|-i\omega + ik| \gg y^{1/n}/(Wn)$, and convection is more important than relaxation. Close to the wall, however, the relaxation term, $y^{1/n}/(Wn)$, is of order n^{-1}, and therefore important. The balance of these two terms, if ω is order unity, occurs at $1 - y \sim n\log n$, so there is a wall layer of width $n\log n$.

6.6.3 Numerical results for small n

We consider here the case in which $k = W = 2$, *i.e.* the parameter values for which we saw the most interesting behaviour in section 6.5. We expect a numerical solution of this model problem to show qualitatively similar results to the full problem, but we would only expect quantitative agreement in the limit $n \to 0$. Because the differential equation is singular as $n \to 0$, neither problem is numerically soluble very close to this value, so the quantitative agreement cannot easily be checked.

Figure 6.25 shows the behaviour of all the roots we have obtained for this model problem, as n varies. There is an unstable mode whose growth rate increases as n decreases, as we found for the full problem. In this case, it is not clear whether the growth rate scales as a power of n or an exponential. However, this reduced problem is capable of producing growth rates which are clearly exponential in n, as shown in figure 6.27, for a lower value of k. The convection behaviour of this root is shown in figure 6.28: the evidence suggests that it is also finite as $n \to 0$.

We also consider the dependence of the growth rates on wavenumber, as we did in section 6.5. Figures 6.29 and 6.30 show the growth and convection rates of the two roots we have found, plotted against the wavenumber, for the two cases $n = 0.1$ and $n = 0.2$. It should be noted that the reduced equation also has a continuous spectrum, in this case at:

$$\left\{ \omega = k - \frac{i}{W} \frac{y_0^{1/n}}{n};\ \psi = \delta(y - y_0) \right\} \tag{6.92}$$

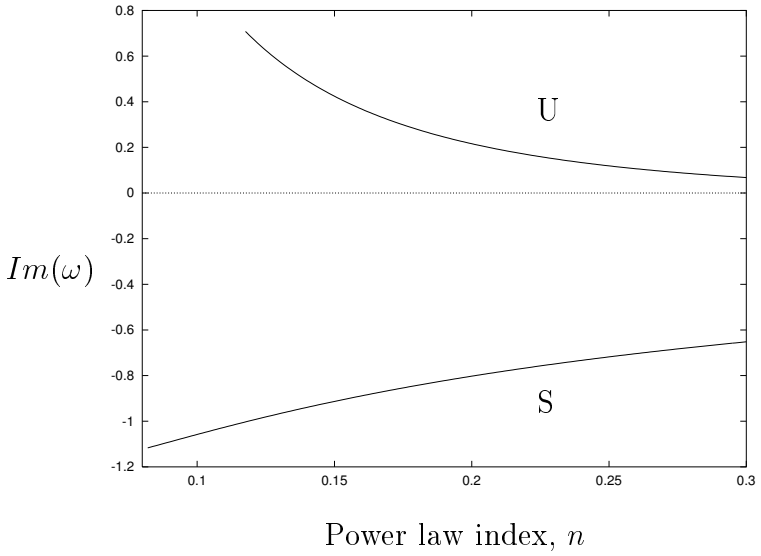

Figure 6.25: Plot of the growth rate against power-law index of roots found numerically for the reduced White-Metzner equation. $W = k = 2$, as for the full case in figure 6.13. The roots are labelled U and S for convenience only: in figure 6.27 we will see that root S can be unstable.

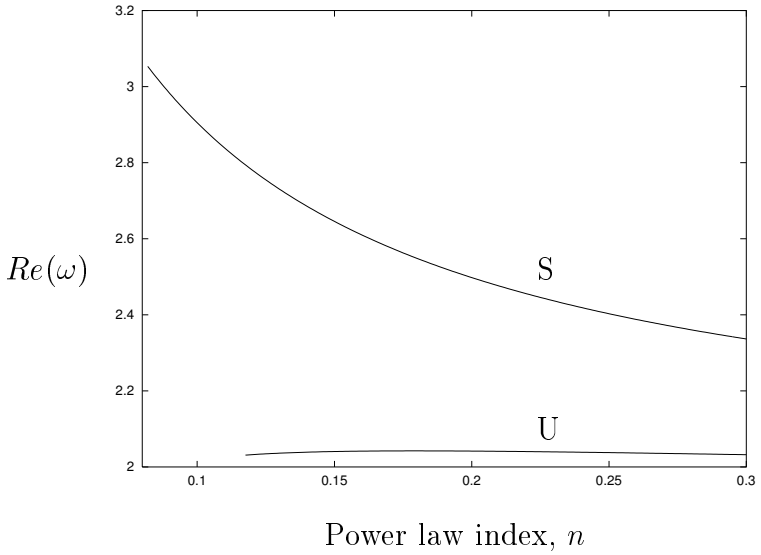

Figure 6.26: Plot of the convective part of the eigenvalues shown in figure 6.25.

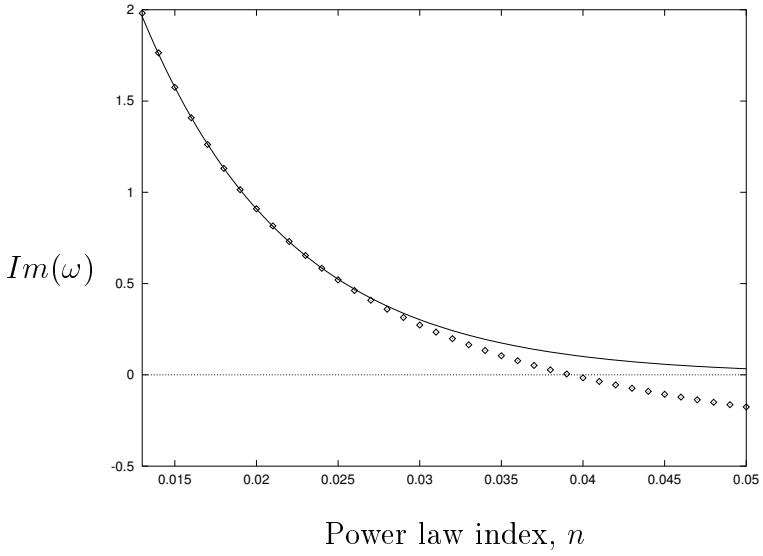

Figure 6.27: Plot of the growth rate against power-law index of root S of the reduced White-Metzner equation, where the mode is unstable. Here $W = 2$ and $k = 0.4$. The points show the numerical results, and the solid line is an exponential fit.

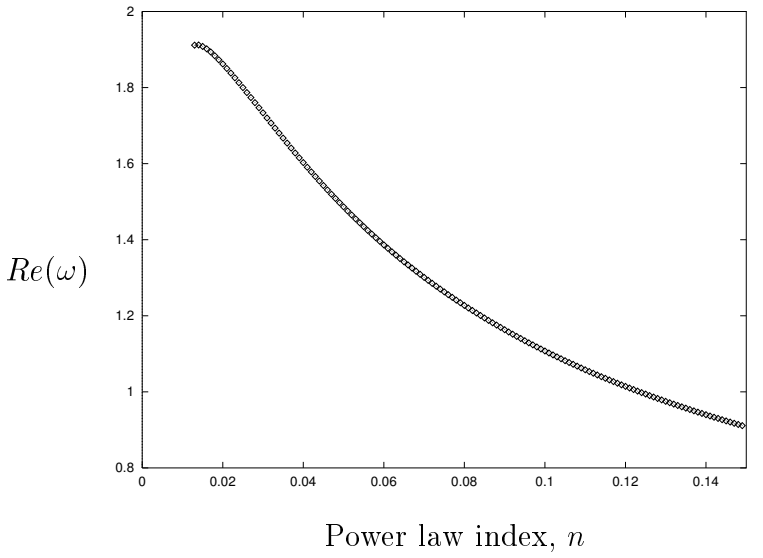

Figure 6.28: Plot of the convection of the eigenvalue from figure 6.27. There is no sign of unbounded growth as $n \to 0$.

which is equivalent to:

$$\left\{\omega = k - \frac{i}{W}\dot{\gamma}\,;\ 0 \leq \dot{\gamma} \leq n^{-1}\right\}. \tag{6.93}$$

This is the reason for the disappearance of the more unstable root, as k decreases.

Because of the thin layers in the base state of this flow (regions of size n close to the wall), the second-order equation we have derived is not appropriate for short waves with $k \gg n^{-1}$. When the wavelength is short, there are two competing short lengthscales, and we have not investigated this situation. Therefore, the increase in growth rate in figure 6.29, as k increases, should not be a cause for concern: the results are only valid for wavelengths of the same order as the channel width, *i.e.* $k \sim O(1)$.

6.7 Conclusions

We have considered the stability of channel flow of a White-Metzner fluid. We find numerical evidence of an instability when $n < 0.3$. This instability is purely elastic in origin, as there is no inertia in our calculation.

The detailed mechanism for the instability remains to be elucidated. There is no interface in the flow, and the base state streamlines are not curved, so this is neither an interfacial nor a Taylor-Couette instability. Nonetheless, N_1 is a crucial ingredient.

For the smallest values of n investigated, short waves are the most unstable; for larger n, waves with length comparable with the channel width grow fastest. They convect with an intermediate region of the fluid: neither

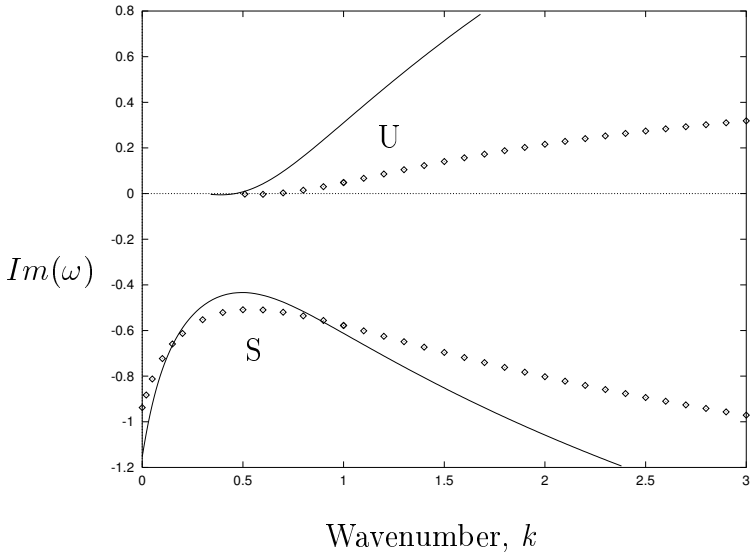

Figure 6.29: Plot of the growth rate against wavenumber for two roots of the reduced White-Metzner equation. The Weissenberg number is $W = 2$, and the solid lines show the case $n = 0.1$, the points $n = 0.2$.

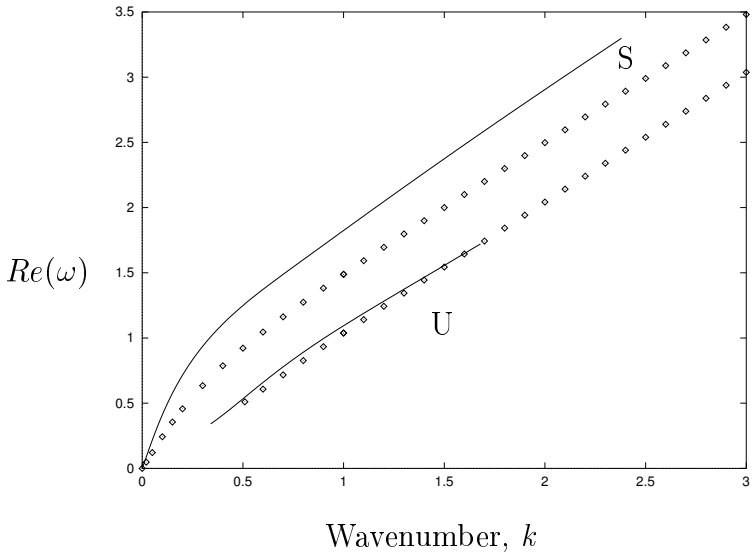

Figure 6.30: Plot of the convection rate of eigenvalues shown in figure 6.29.

the wall (which is stationary) nor the central region (which has velocity 1 in dimensionless coordinates, and corresponds to $\omega \approx k$).

6.8 Appendix: Preliminary asymptotics for $n \to 0$

In this appendix, we present some preliminary working towards an asymptotic solution of equation (6.84) of section 6.6, as $n \to 0$.

In order to solve the equation, we will have to assume a scaling for ω, and check our solution for self-consistency at the end. Motivated by the results of section 6.7, we assume that ω is $O(1)$.

6.8.1 Outer

Far from the wall, where $y^{1/n} \ll n$, equation (6.84) becomes:

$$n\psi'' - \Theta^2(y)\psi = \tilde{A}y \tag{6.94}$$

with boundary condition:

$$\psi(0) = 0. \tag{6.95}$$

This is solved by a multiple-scales method, using fast scale $y/n^{1/2}$ and slow, frequency-modulation scale y. The leading order solution is:

$$\psi = -\frac{\tilde{A}y}{\Theta^2(y)} + \frac{M}{\Theta(y)} \sinh\left(\Theta(y)\frac{y}{n^{1/2}}\right) \tag{6.96}$$

for some constant M. In order to determine the form of the coefficient of $\sinh\left(\Theta(y)yn^{-1/2}\right)$, we have worked to order $n^{1/2}$ and applied a secularity condition.

The structure of this solution is exponential, and has parts which grow as either $y \to 0$ or $y \to 1$. This is one reason why the numerical solution has

problems for small values of n. Whichever direction is chosen for the integration, an error can increase by a factor of $\exp(\Theta n^{-1/2})$ as the integration takes place, where $Re(\Theta) \geq 2k$.

6.8.2 Wall layer

The outer solution is valid for $y^{1/n} \ll n$. Therefore, for the regions close to the wall we will need $y^{1/n} \gtrsim n$, so we put $y = 1 - n \log x$. Then the region $1 \geq y^{1/n} \gtrsim n$ becomes $1 \leq x \lesssim n^{-1}$. The derivatives are:

$$\psi' = \frac{d_x \psi}{dy/dx} = -\frac{x}{n} d_x \psi \tag{6.97}$$

and:

$$\psi'' = \frac{d_x \psi'}{dy/dx} = -\frac{x}{n} d_x \left(-\frac{x}{n} d_x \psi \right) = \frac{1}{n^2} (x\, d_x \psi + x^2\, d_x^2 \psi). \tag{6.98}$$

Equation (6.84) becomes:

$$x^2 d_x^2 \psi + x d_x \psi - \frac{2ikWx d_x \psi}{(1 + n\tilde{W}x)} - n\Theta_1^2 \psi = \tilde{A}n + \frac{A}{Wx} \tag{6.99}$$

where:

$$\Theta_1 = \Theta(1) = (4k^2 + ikW + 2W^2 k^2)^{1/2} \tag{6.100}$$

with $Re(\Theta_1) > 0$. The boundary conditions are:

$$\psi(1) = \psi'(1) = 0. \tag{6.101}$$

We find that the region in which this scaling applies divides into two further regions.

Inner

First, we solve the inner equation in the region closest to the wall, $x \sim 1$. Equation (6.99) becomes:

$$x^2 d_x^2 \psi + x d_x \psi - 2ikWx d_x \psi = \frac{A}{Wx} \tag{6.102}$$

and we solve at leading order:

$$d_x \psi = \frac{A}{W(1+2ikW)}(x^{(2ikW-1)} - x^{-2}) \tag{6.103}$$

and hence:

$$\psi = \frac{A}{W(1+2ikW)}\left(\frac{x^{2ikW}-1}{2ikW} + x^{-1} - 1\right). \tag{6.104}$$

This has no undetermined constant, because we have applied both the wall boundary conditions.

Middle layer

The biggest term we neglected in the wall layer was of order nx so the next scale is $\eta = nx$. Equation (6.99) becomes:

$$\eta \frac{d^2\psi}{d\eta^2} + \frac{d\psi}{d\eta} - \frac{2ikW d\psi/d\eta}{(1+\tilde{W}\eta)} = 0 \tag{6.105}$$

and therefore:

$$\frac{d\psi}{d\eta} = \frac{G_0}{\eta}\left(\frac{\eta}{1+\tilde{W}\eta}\right)^{2ikW}. \tag{6.106}$$

We cannot integrate this directly, but rather give the form of ψ as:

$$\psi = G_0 \int_n^\eta \left(\frac{t}{1+\tilde{W}t}\right)^{2ikW} \frac{dt}{t} + G_1. \tag{6.107}$$

We have now solved the equation in three asymptotic regions; the remaining task is to match these solutions together to determine ω.

6.8.3 Matching

Inner to middle layer

We match the wall region to the middle layer first. The coordinates of the two regions are x near the wall, and η in the middle region, where $\eta = nx$. We match with an intermediate variable $\nu = n^\beta x = n^{\beta-1}\eta$, where $0 < \beta < 1$.

The two functions to match become:

$$\psi_{\text{inner}} = \frac{A}{W(1+2ikW)}\left(\frac{n^{-2ikW\beta}\nu^{2ikW}-1}{2ikW} + n^\beta \nu^{-1} - 1\right) \tag{6.108}$$

and in the middle:

$$\psi_{\text{middle}} = G_0 \int_n^{n^{1-\beta}\nu} \left(\frac{t}{1+W(-i\omega+ik)t}\right)^{2ikW} \frac{dt}{t} + G_1. \tag{6.109}$$

Expanding, we have:

$$\psi_{\text{inner}} = n^{-2ikW\beta}\nu^{2ikW}\frac{A}{2ikW^2(1+2ikW)} - \frac{A}{2ikW^2} + O(n^\beta) \tag{6.110}$$

and:

$$\psi_{\text{middle}} = n^{-2ikW\beta}\nu^{2ikW}\frac{G_0 n^{2ikW}}{2ikW} + G_1 - \frac{G_0 n^{2ikW}}{2ikW} + O(n^{1-\beta}). \tag{6.111}$$

We deduce that:

$$G_0 = \frac{An^{-2ikW}}{W(1+2ikW)} \tag{6.112}$$

and:

$$G_1 = -\frac{A}{W(1+2ikW)}. \tag{6.113}$$

Outer to middle layer

In order to match the outer layer to the middle, we need a variable which will move between the scales of $n^{1/2}$ and $n \log n$. This is complicated in itself; another complication is the fact that we do not know the full solution in the middle region except as an integral.

If we use instead the naïve method, and take the limit as $\eta \to \infty$ of the middle layer, we obtain:

$$\psi_{\text{middle}} = G_0 \tilde{W}^{-2ikW} \log \eta + G_1 - G_0 \tilde{W}^{-2ikW} \left(\int_n^\infty \left\{ \left(\frac{t}{t + \tilde{W}^{-1}} \right)^{2ikW} - 1 \right\} \frac{dt}{t} + \log n \right) \quad (6.114)$$

which is to match against:

$$\psi_{\text{outer}} = -\frac{\tilde{A} y}{\Theta^2(y)} + \frac{M}{\Theta(y)} \sinh \left(\Theta(y) \frac{y}{n^{1/2}} \right). \quad (6.115)$$

Substituting the definition $1 - y = n \log (\eta / n)$, we obtain:

$$\psi_{\text{middle}} = G_0 \tilde{W}^{-2ikW} \frac{1-y}{n} + G_1 - G_0 \tilde{W}^{-2ikW} \left(\int_n^\infty \left\{ \left(\frac{t}{t + \tilde{W}^{-1}} \right)^{2ikW} - 1 \right\} \frac{dt}{t} \right). \quad (6.116)$$

In theory, we can extend this matching until ω is determined. The difficulty is the appearance of logarithms here: as noted by Van Dyke [205], all the logarithmic terms may have to be included in the matching process, and we have not satisfactorily resolved this difficulty.

Chapter 7

Criterion for Coextrusion Instability

7.1 Introduction

We have indicated (in chapters 4 and 5) that, even for a continuously stratified Oldroyd-B fluid, the Lagrangian convection of material properties (either a time constant or a concentration) is an essential ingredient for the development of the 'coextrusion' instability[1]. In other words, we claim that a different fluid, in which material properties are not convected, may display the same base state velocity profile and stress distribution, and yet the unstable 'coextrusion' mode may be absent.

We establish this possibility by reference to a specific case. In this chapter, we use both the White-Metzner formalism, in which material properties depend on shear-rate, and the Oldroyd-B formalism of chapters 4 and 5, in which they are Lagrangian properties. We define two fluids with almost identical profiles of velocity and stress in a channel flow, and show the effect of the model type on the stability spectrum in section 7.6. Section 7.7 discusses this effect and its implications for constitutive modelling.

7.2 A model problem

We consider the channel flows of two different fluids. The first is a generalisation of the White-Metzner fluid of chapter 6, and the second a combination of the two Oldroyd-B fluids of chapters 4 and 5.

[1] Mathematically, the 'coextrusion' mode comes into existence at a singular point of the governing equations. The existence of this point depends on the presence of a material derivative, which is precisely a derivative with respect to a Lagrangian coordinate. This derivative is only relevant where some material property undergoes Lagrangian convection.

7.2.1 White-Metzner fluid

The White-Metzner fluid, as it is defined in chapter 6, applied to a two-dimensional channel flow, exhibits a first normal stress difference, N_1, which is quadratic in distance across the channel. This property is independent of the relaxation function $\tau(\dot{\gamma})$.

In order to compare with a fluid which shows the 'coextrusion' instability, we need a fluid which will show steep gradients in N_1 across the channel. By adding a solvent viscosity (a physically sensible modification), we can reduce the effect of τ on the shear stress, and thus increase its effect on the normal stress. The case $\tau(\dot{\gamma}) = \text{constant}$ becomes the simple Oldroyd-B fluid, whereas in chapter 6 it gave us the UCM fluid.

In the notation of chapter 2, this generalisation of the White-Metzner fluid is given by[2] $C = C_0$, $W = W_0$, $\mu = 1$; $\tau(\dot{\gamma})$ may be any monotonic function.

7.2.2 Oldroyd-B fluid

We want to define a fluid whose material properties are convected, but whose base state velocity and stress profile are identical to the generalised White-Metzner fluid already specified above. Neither the model of chapter 4, in which the Weissenberg number is convected with the fluid, nor that of chap-

[2]In the perturbation equations of section 7.5.1, we will see that W_0 only ever appears as part of C_0/W_0, and so we may without loss of generality set $W_0 = 1$. Physically, this is simply a matter of taking the elastic timescale into the definition of τ, or equivalently using a different nondimensionalisation for Σ. However, for easy specialisation to other fluids it is more convenient to leave both C_0 and W_0 to vary.

ter 5, in which the convected property is polymer concentration, gives sufficient freedom.

Therefore we define a generalised Oldroyd-B model in which both C and W are permitted to vary with Lagrangian distance across the channel: $C(\eta)$, $W(\eta)$. Both C and W will undergo Lagrangian convection. In the formulation of chapter 2, we set $\mu = 1$ and $\tau = W$.

7.3 Base state

7.3.1 White-Metzner fluid

The base state for channel flow of our generalised White-Metzner fluid is:

$$\dot{\gamma}_0 = |U'| = -U' \tag{7.1}$$

$$\tau_0 = \tau(\dot{\gamma}_0) \tag{7.2}$$

$$\boldsymbol{A} = \begin{pmatrix} 1 + 2(\tau_0 U')^2 & \tau_0 U' \\ \tau_0 U' & 1 \end{pmatrix} \tag{7.3}$$

$$P = P_\infty + C_0/W_0 + P_0 x \tag{7.4}$$

$$\boldsymbol{\Sigma} = \begin{pmatrix} -P_\infty - P_0 x + 2C_0(\tau_0 U')^2/W_0 & P_0 y \\ P_0 y & -P_\infty - P_0 x \end{pmatrix} \tag{7.5}$$

and finally:

$$(1 + C_0\tau_0/W_0)U' = P_0 y. \tag{7.6}$$

Equation (7.6) defines $\dot{\gamma}_0$, which may only be computed numerically for most functions $\tau(\dot{\gamma})$.

7.3.2 Oldroyd-B fluid

The base state for the generalised Oldroyd-B fluid becomes:

$$\boldsymbol{A} = \begin{pmatrix} 1 + 2(WU')^2 & WU' \\ WU' & 1 \end{pmatrix} \tag{7.7}$$

$$P = P_\infty + C/W + P_0 x \tag{7.8}$$

$$\boldsymbol{\Sigma} = \begin{pmatrix} -P_\infty - P_0 x + 2CW(U')^2 & P_0 y \\ P_0 y & -P_\infty - P_0 x \end{pmatrix} \tag{7.9}$$

$$(1 + C)U' = P_0 y. \tag{7.10}$$

7.4 Choice of parameters

7.4.1 White-Metzner fluid

We use an arctan profile for τ:

$$\tau(\dot{\gamma}) = \overline{\tau} + \tfrac{\Delta\tau}{\pi} \arctan((\dot{\gamma} - \overline{\dot{\gamma}})/q). \tag{7.11}$$

This gives us a model with parameters C_0, W_0, $\overline{\tau}$, $\Delta\tau$, q and $\overline{\dot{\gamma}}$. For small values of C_0 and q, it is capable of giving high gradients of N_1:

$$U' \approx P_0 y \tag{7.12}$$

$$\implies N_1 \approx 2C_0 P_0^2 y^2 \tau(|P_0 y|)^2 / W_0. \tag{7.13}$$

We therefore select the specific model parameters (used for demonstration) to be: $C_0 = 0.1$, $q = 0.002$, $W_0 = 1$, $\overline{\tau} = 3.5$, $\Delta\tau = 1$ and $\overline{\dot{\gamma}} = 1$.

7.4.2 Oldroyd-B fluid

We choose the functions $C(\eta)$ and $W(\eta)$ for the Oldroyd type fluid so that its base state velocity profile, pressure and stresses are the same as those of the White-Metzner type fluid.

For the White-Metzner fluid, the relevant quantities are:

$$\Sigma_{12} = (1 + C_0\tau_0/W_0)U' = P_0 y \tag{7.14}$$

$$N_1 = 2C_0(\tau_0 U')^2/W_0 \tag{7.15}$$

$$P = P_\infty + C_0/W_0 + P_0 x \tag{7.16}$$

and for the Oldroyd fluid:

$$\Sigma_{12} = (1 + C(\eta))U' \tag{7.17}$$

$$N_1 = 2CW(U')^2 \tag{7.18}$$

$$P = P_\infty + C/W + P_0 x. \tag{7.19}$$

Therefore, for equivalence between the two fluids in the base state, we need U' and the stresses to be the same in each and so:

$$W(\eta) = \tau_0(\dot\gamma) \tag{7.20}$$

and:

$$C(\eta) = C_0\tau_0(\dot\gamma)/W_0 = 0.1\ W(\eta). \tag{7.21}$$

We integrate the White-Metzner form numerically to find $\dot\gamma$ as a function of y, and hence find $\tilde\tau(y)$ (which should be equal to $\tau_0(\dot\gamma)$). We obtain a good approximate fit (shown in figure 7.1) with:

$$\tilde\tau(y) = 3.5 + 0.5\tanh(60(y - 0.491)). \tag{7.22}$$

7.5 Perturbation equations

7.5.1 White-Metzner fluid

Referring back to equations (2.32) – (2.43) of chapter 2, the perturbation equations for the generalised White-Metzner fluid become:

$$ik\sigma_{11} + \sigma'_{12} = 0 \tag{7.23}$$

$$ik\sigma_{12} + \sigma'_{22} = 0 \tag{7.24}$$

$$\sigma_{11} = -p + 2ik\psi' + \tfrac{C_0}{W_0}a_{11} \tag{7.25}$$

$$\sigma_{12} = \psi'' + k^2\psi + \tfrac{C_0}{W_0}a_{12} \tag{7.26}$$

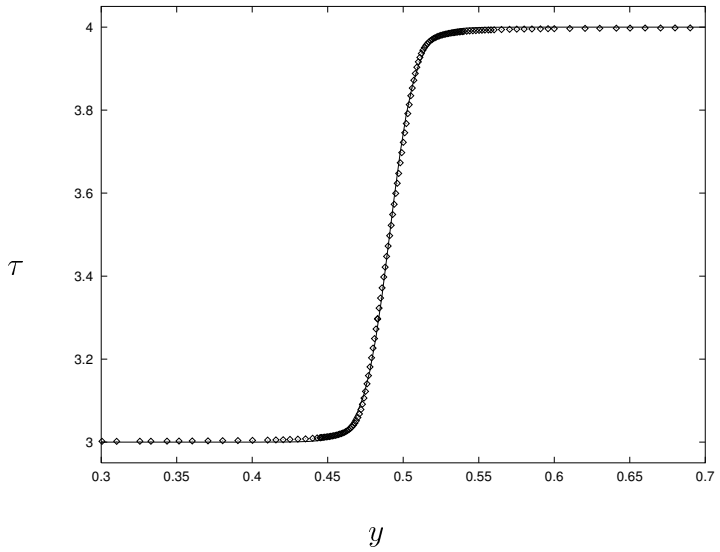

Figure 7.1: Plot of $\tau(\dot{\gamma})$ across the channel (points) with the analytic function $\tilde{\tau}(y)$ (solid line).

$$\sigma_{22} = -p - 2ik\psi' + \tfrac{C_0}{W_0} a_{22} \tag{7.27}$$

$$\left(-i\omega + ikU + \frac{1}{\tau_0}\right) a_{11} = ik\psi A'_{11} + 2A_{12}\psi'' + 2A_{11}ik\psi' + 2U'a_{12} + \frac{\tau_1}{\tau_0^2}(A_{11} - 1) \tag{7.28}$$

$$\left(-i\omega + ikU + \frac{1}{\tau_0}\right) a_{12} = ik\psi A'_{12} + \psi'' + A_{11}k^2\psi + U'a_{22} + \frac{\tau_1}{\tau_0^2} A_{12} \tag{7.29}$$

$$\left(-i\omega + ikU + \frac{1}{\tau_0}\right) a_{22} = -2ik\psi' + 2A_{12}k^2\psi \tag{7.30}$$

$$\tau_1 = \dot{\gamma}_1 \partial\tau_0 / \partial\dot{\gamma}_0 \tag{7.31}$$

$$\dot{\gamma}_1 = -(\psi'' + k^2\psi). \tag{7.32}$$

These may be solved numerically in the same way as those in chapters 4, 5 and 6.

7.5.2 Oldroyd-B fluid

We use the advected form (section 2.7) of the perturbation equations, and note that $C/W = C_0/W_0$ to obtain:

$$ik\sigma_{11} + \sigma'_{12} = 2ik\zeta P_0^2 y^2 \{CW(1+C)^{-2}\}' \tag{7.33}$$

$$ik\sigma_{12} + \sigma'_{22} = 0 \tag{7.34}$$

$$\sigma_{11} = -p + 2ik\psi' + \frac{C_0}{W_0}a_{11} \tag{7.35}$$

$$\sigma_{12} = \{\psi'' + \zeta P_0 y((1+C)^{-1})'\} + k^2\psi + \frac{C_0}{W_0}a_{12} \tag{7.36}$$

$$\sigma_{22} = -p - 2ik\psi' + \frac{C_0}{W_0}a_{22} \tag{7.37}$$

$$\left(-i\omega + ikU + \frac{1}{W}\right) a_{11} = ik\psi\frac{4W^2P_0^2y}{(1+C)^2} + 2A_{12}\{\psi'' + \zeta P_0 y((1+C)^{-1})'\} + 2A_{11}ik\psi' + 2U'a_{12} \tag{7.38}$$

$$\left(-i\omega + ikU + \frac{1}{W}\right) a_{12} = ik\psi\frac{WP_0}{(1+C)} + \{\psi'' + \zeta P_0 y((1+C)^{-1})'\} + A_{11}k^2\psi + U'a_{22} \tag{7.39}$$

$$\left(-i\omega + ikU + \frac{1}{W}\right) a_{22} = -2ik\psi' + 2A_{12}k^2\psi \tag{7.40}$$

$$(-i\omega + ikU)\zeta = -ik\psi. \tag{7.41}$$

7.6 Numerical results

The two fluids we have chosen appear identical in terms of their base-flow stresses. Figures 7.2 and 7.3 show part of their stability spectra for varicose modes. (In each case, the only modes not shown here are more stable than the ones shown, and may safely be ignored.) It may be seen that the Oldroyd fluid has an unstable mode for moderate values of k, as discussed in chapters 4

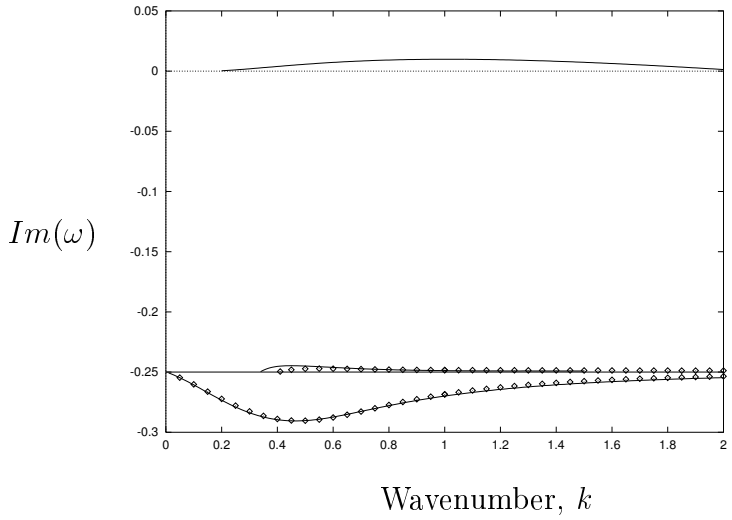

Figure 7.2: The least stable part of the spectra of the generalised fluids. The solid lines are for the Oldroyd type fluid (the horizontal line is part of its continuous spectrum), and the points are for the White-Metzner type fluid. Only the Oldroyd fluid shows the unstable mode.

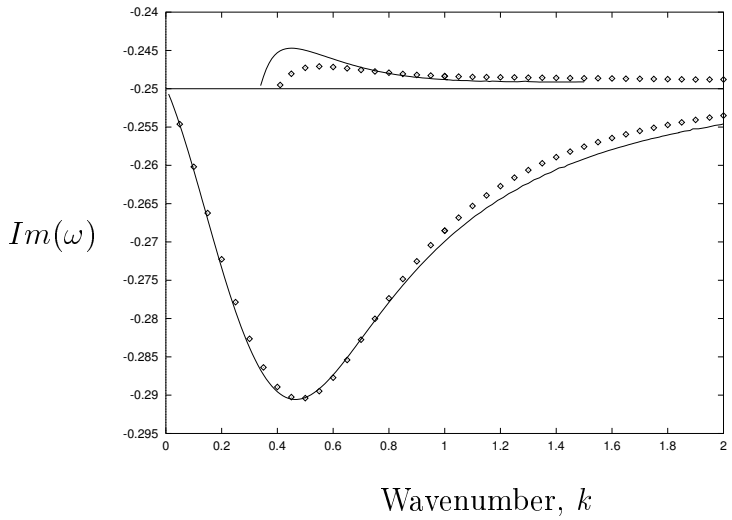

Figure 7.3: A close-up of the lower region of figure 7.2, demonstrating the close correspondence between the two spectra.

and 5. No such mode exists for the White-Metzner fluid, which is stable to perturbations of all wavenumbers.

The stable parts of the spectra are very similar (as shown in the close-up in figure 7.3). This indicates that if a more 'blurred' profile were chosen, for which the Oldroyd 'coextrusion' mode ceases to exist (as shown in chapters 4 and 5), to all extents and purposes the two models would be equivalent.

7.7 Conclusions

The extra eigenvalue in the Oldroyd spectrum (compared with the White-Metzner spectrum) indicates a fundamental difference between the two fluids. In a simple Poiseuille flow, the former is unstable and the latter stable.

The presence of the convective derivative $(-i\omega + ikU)$ in equation (7.41) of the Oldroyd model permits a singularity in the equations, at which a neutral mode may appear. It is this mode (discussed in chapter 4) which becomes unstable. The White-Metzner model has no such term, and hence no such singularity, and no such neutral mode. As a result, it cannot exhibit the 'coextrusion' form of instability.

These two fluids suggest that *two* criteria must be met for this form of instability. First, there must be sufficiently steep gradients in some physical quantity in a thin region of base flow. This region might be a vortex sheet, or a layer of steep gradients of stress. For illustration, we treat it as a region of large stress gradients, as in the fluid of chapter 4.

In general, the states of stress will be different on the two sides of this small region. Let us assume that these two states of stress are such that the

interface between two fluids flowing with these stresses would be unstable. For the flows of chapter 4, this corresponds to choosing W_1 and W_2 so that the corresponding interfacial flow of chapter 3 would be unstable.

Second, we require that the material properties be advected with the flow. It follows that the existence of an instability is not dictated by the base state alone, but depends also on the constitutive behaviour. Suppose for example that the fluid possesses a second timescale, $\mathcal{T}$, over which the fluid 'relaxes' some material property.

The Oldroyd limit

> In this limit, a material parcel retains its value of W throughout its life. Therefore the timescale on which W changes for any fluid parcel is effectively infinite, $\mathcal{T} = \infty$.

The White-Metzner limit

> In this case, on the other hand, $W = W(\dot{\gamma})$, *i.e.* a parcel's Weissenberg number is an instantaneous function of the applied rate of strain. W has no memory of past values, but rather reacts to the flow on a timescale $\mathcal{T} = 0$.

The White-Metzner fluid (for which $\mathcal{T} = 0$) is stable where the Oldroyd fluid (for which $\mathcal{T} = \infty$) is not. This may suggest a critical value of $\mathcal{T}$ below which the 'coextrusion' instability does not exist. This second timescale, $\mathcal{T}$, is an important property for comparison of different constitutive models, and one which has not been considered before.

Chapter 8

Conclusions

The focus of this dissertation is to examine the stability of planar channel flows of viscoelastic liquids.

We have shown theoretically the existence of two purely elastic instabilities whose mechanisms depend neither on the presence of an interface nor on streamline curvature. We do not believe that these instabilities have been identified before.

The first instability depends on advection of material properties, and is an extension of, and shares a mechanism with, the interfacial instability that arises in coextrusion (chapter 3).

The second instability (introduced in chapter 6) is predicted to occur in a highly shear-thinning White-Metzner fluid, and is discussed below, along with suggestions for future work to elucidate the mechanism.

Coextrusion instability

For coextrusion of two fluids, our theoretical understanding of the linear instability problem is now more or less complete. Earlier work [79] had identified a long-wave instability mechanism, which we have now extended to short waves; and, numerically, to waves of all wavelengths.

We have posed the question as to whether the same mechanism can operate when fluid properties are continuously stratified. It can, provided there remain sufficiently sharp gradients in normal stress, and provided material properties are advected by the flow.

The way in which 'blurring' of an interface is able to stabilise a flow has been identified. For a two fluid case, experiments have shown the instability that we have discussed. Further experiments are needed for comparison with

the continuously stratified case that we have identified; for example, with polymer solutions having cross-channel variations in concentration.

Shear-thinning instability

In chapter 6, we considered a highly shear-thinning White-Metzner fluid, and found that, for sufficiently large degree of shear-thinning (power-law coefficient $n < 0.2$), there is an instability provided that the normal stress, N_1, does not shear-thin more strongly than the shear viscosity.

This instability is not driven by steep *gradients* in normal stress, because the profile of N_1 across a slit is quadratic, for such a fluid. However, the presence of normal stress is essential to the instability mechanism.

In the long-wave limit, we have shown that the mode restabilises, even for small values of n comparable with the wavenumber. Thus the mechanism depends on having waves with wavelengths comparable with the channel width and shorter.

Several extensions to this theory would be desirable. First, the White-Metzner model, though commonly used for polymer melt flows (particularly shear flows) has a weak physical foundation, and the extent to which the conclusions are functions of the model chosen needs to be explored. Second, the power law model leads to a spurious non-smoothness in fluid properties, at the channel centre. We have therefore explored only varicose instability modes, for which the singularity disappears. Sinuous modes may well turn out to be less stable. Third, the technical task of extending the analysis to axisymmetric flows of greater practical importance should be undertaken. Channel flows are directly relevant to cylindrical extrusion, which is used

in the creation of polymeric fibres. Fourth, and most important, experiments are needed to examine the stability of channel flows for fluids whose viscometric properties thin, but whose normal stresses remain significant at high shear-rates. Our analysis suggests that the class of extrusion instability called wavy instability may originate dynamically in the extruder, rather than being a consequence of stick-slip as is often supposed.

Nomenclature

Roman characters

$\boldsymbol{A}$, $\boldsymbol{a}$	Polymer stretch
C, c	Polymer concentration
D	Derivative with respect to y
d	Width of thin layer in a blurred profile
$\boldsymbol{E}$	Rate-of-strain tensor
$\mathcal{E}$	Exponential integral
$\boldsymbol{F}$	Spring force in a dumbbell
$\mathcal{F}$	Body force
G	Elastic modulus
H	Heaviside function
$\boldsymbol{I}$	Identity matrix
k_*, k	Dimensional and dimensionless wavenumber
L	Channel half-width
N	Winding number
N_1, N_2	First and second normal stress differences
n	Power-law coefficient

P, p	Pressure
P_0	Dimensionless pressure gradient
Q	Velocity integral
q	Dimensionless width of thin layer in blurred profile
$\tilde{q}$	Rescaling of q by k where k is small
$\boldsymbol{R}$	Vector representation of dumbbell spring
t	Time
$\mathcal{T}$	Secondary timescale
T_*, T	Dimensional and dimensionless surface tension coefficients
$\top$	Transpose of a matrix
U_0	Base x-velocity at channel centreline
U, u, v	Velocities
W, ϖ	Weissenberg number
$\mathcal{W}$	Wall Weissenberg number
x, y	Eulerian coordinates

Greek characters

α	Factor for evolution of $\boldsymbol{a}$: advection and relaxation
$\dot{\gamma}_*$, $\dot{\gamma}$	Dimensional and dimensionless shear-rate
ϵ	Small quantity
ζ	Perturbation to interface or streamline; Stokes drag coefficient
η	Lagrangian coordinate; Shear viscosity
κ	Position of fluid-fluid interface
λ	Fluid relaxation time;

	Parameter $(kW/2n)^{1/2}$ in the small k, small n expansion of chapter 6
μ	Indicator function for presence of solvent viscosity
μ_*	Typical shear viscosity
ρ	Fluid density
$\mathbf{\Sigma}$, $\boldsymbol{\sigma}$	Stress tensor
τ	Dimensionless relaxation time
ψ	Streamfunction
ω	Complex frequency

Bibliography

[1] A C T Aarts and A A F van de Ven. Transient behaviour and stability points of the Poiseuille flow of a KBKZ-fluid. *Journal of Engineering Mathematics*, 29(4):371–392, 1995.

[2] K E P Adewale, O Olabisi, A A Oyediran, and V O S Olunloyo. A stick-slip problem related to melt fracture in polymer processing operations. *International Polymer Processing*, 6(3):195–198, 1991.

[3] H Andrianarahinjaka and P Micheau. Instability phenomena in film blowing process – a linear-stability analysis. *Comptes Rendus de l'Académie des Sciences Série II Fascicule B – Mécanique Physique Chimie Astronomie*, 322(5):363–370, 1996.

[4] M T Arigo, D Rajagopalan, N Shapley, and G H McKinley. The sedimentation of a sphere through an elastic fluid. 1. Steady motion. *Journal of Non-Newtonian Fluid Mechanics*, 60(2–3):225–257, 1995.

[5] B T Atwood. *Wall slip and extrudate distortion of high density polyethylene*. PhD thesis, Department of Chemical Engineering, Princeton University, Princeton, 1983.

[6] E B Bagley and A M Birks. Flow of polyethylene into a capillary. *Journal of Applied Physics*, 31(3):556–561, 1960.

[7] E B Bagley, S H Storey, and D C West. Post extrusion swelling of polyethylene. *Journal of Applied Polymer Science*, 7:1661–1672, 1963.

[8] R Y Bai, K P Chen, and D D Joseph. Lubricated pipelining – stability of core-annular flow. 5. Experiments and comparison with theory. *Journal of Fluid Mechanics*, 240:97–132, 1992.

[9] T F Ballenger, I J Chen, J W Crowder, G E Hagler, D C Bogue, and J L White. Polymer melt flow instabilities in extrusion: investigation of the mechanism and material and geometric variables. *Transactions of the Society of Rheology*, 15(2):195–215, 1971.

[10] T F Ballenger and J L White. The development of the velocity field in polymer melts in a reservoir approaching a capillary die. *Journal of Applied Polymer Science*, 15:1949–1962, 1971.

[11] B M Baumert and S J Muller. Flow visualisation of the elastic Taylor-Couette instability in Boger fluids. *Rheologica Acta*, 34(2):147–159, 1995.

[12] J Becker, P Bengtsson, C Klason, J Kubat, and P Saha. Pressure oscillations during capillary extrusion of high-density polyethylene. *International Polymer Processing*, 6(4):318–325, 1991.

[13] J J Benbow and P Lamb. New aspects of melt fracture. *Society of Petroleum Engineers Transactions*, 3(1):7–17, 1963.

[14] T B Benjamin. Wave formation in laminar flow down an inclined plane. *Journal of Fluid Mechanics*, 2:554–574, 1957.

[15] A N Beris and M Avgousti. Viscoelastic flow instabilities: inception and non-linear evolution. In P Moldenaers and R Keunings, editors, *Theoretical and Applied Rheology, Proceedings of the X International Congress on Rheology*, volume 1, pages 33–38, Belgium, 1992. Elsevier.

[16] B Bernstein, E A Kearsley, and L J Zapas. A study of stress relaxation with finite strain. *Transactions of the Society of Rheology*, 7:391–410, 1963.

[17] R B Bird, R C Armstrong, and O Hassager. *Dynamics of Polymeric Liquids*, volume 1: Fluid Mechanics. John Wiley and Sons, Inc., 1977.

[18] R B Bird, O Hassager, R C Armstrong, and C F Curtiss. *Dynamics of Polymeric Liquids*, volume 2: Kinetic Theory. John Wiley and Sons, Inc., 1977.

[19] R B Bird and J M Wiest. Constitutive equations for polymeric liquids. *Annual Review of Fluid Mechanics*, 27:169–193, 1995.

[20] C Bisgaard. Velocity fields around spheres and bubbles investigated by laser-doppler anemometry. *Journal of Non-Newtonian Fluid Mechanics*, 12(3):283–302, 1983.

[21] D V Boger. A highly elastic constant-viscosity fluid. *Journal of Non-Newtonian Fluid Mechanics*, 3:87–91, 1977/78.

[22] W F Busse. Two decades of high-polymer physics – a survey and forecast. *Physics Today*, 17(9):32–41, September 1964.

[23] J A B Byars, A Öztekin, R A Brown, and G H McKinley. Spiral instabilities in the flow of highly elastic fluids between rotating parallel disks. *Journal of Fluid Mechanics*, 271:173–218, 1994.

[24] P J Cable and D V Boger. A comprehensive experimental investigation of tubular entry flow of viscoelastic fluids. I. Vortex characteristics in stable flow. *American Institute of Chemical Engineering Journal*, 24(5):869–879, 1978.

[25] P J Cable and D V Boger. A comprehensive experimental investigation of tubular entry flow of viscoelastic fluids. II. The velocity field in stable flow. *American Institute of Chemical Engineering Journal*, 24(6):992–999, 1978.

[26] P J Cable and D V Boger. A comprehensive experimental investigation of tubular entry flow of viscoelastic fluids. III. Unstable flow. *American Institute of Chemical Engineering Journal*, 25(1):152–159, 1979.

[27] J J Cain and M M Denn. Multiplicities and instabilities in film blowing. *Polymer Engineering and Science*, 28(23):1527–1540, 1988.

[28] P J Carreau. *Rheological equations from molecular network theories.* PhD thesis, University of Wisconsin, Madison, 1968.

[29] B W Char, K O Geddes, G H Gonnet, B L Leong, M B Monagan, and S M Watt. *Maple V Library/Language Reference Manual.* Springer-Verlag and Waterloo Maple Publishing, 1991.

[30] A Chawda and M Avgousti. Stability of viscoelastic flow between eccentric rotating cylinders. *Journal of Non-Newtonian Fluid Mechanics*, 63(2–3):97–120, 1996.

[31] I J Chen, G E Hagler, L E Abbot, D C Bogue, and J L White. Interpretation of tensile and melt spinning experiments on low density and high density polyethylene. *Transactions of the Society of Rheology*, 16(3):473–494, 1972.

[32] K P Chen. Elastic instability of the interface in Couette-flow of viscoelastic liquids. *Journal of Non-Newtonian Fluid Mechanics*, 40(2):261–267, 1991.

[33] K P Chen. Interfacial instability due to elastic stratification in concentric coextrusion of two viscoelastic fluids. *Journal of Non-Newtonian Fluid Mechanics*, 40(2):155–176, 1991.

[34] K P Chen. Short-wave instability of core-annular flow. *Physics of Fluids A*, 4(1):186–188, 1992.

[35] K P Chen. Hyperbolicity and change of type in steady co-extrusion flow of Upper-Convected Maxwell fluids. *Journal of Non-Newtonian Fluid Mechanics*, 47:157–167, 1993.

[36] K P Chen and D D Joseph. Long-wave and lubrication theories for core-annular flow. *Physics of Fluids A*, 3(11):2672–2679, 1991.

[37] K P Chen and D D Joseph. Elastic short-wave instability in extrusion flows of viscoelastic liquids. *Journal of Non-Newtonian Fluid Mechanics*, 42(1–2):189–211, 1992.

[38] K P Chen and Y Zhang. Stability of the interface in co-extrusion flow of two viscoelastic fluids through a pipe. *Journal of Fluid Mechanics*, 247:489–502, 1993.

[39] M D Chilcott and J M Rallison. Creeping flow of dilute polymer solutions past cylinders and spheres. *Journal of Non-Newtonian Fluid Mechanics*, 29(1–3):381–432, 1988.

[40] C Chmielewski and K Jayamaran. Elastic instability in cross-flow of polymer-solutions through periodic arrays of cylinders. *Journal of Non-Newtonian Fluid Mechanics*, 48(3):285–301, 1993.

[41] R E Christensen. Extrusion coating of polypropylene. *Society of Petroleum Engineers Journal*, 18:751–755, July 1962.

[42] P L Clegg. Elastic effects in the extrusion of polythene. In P Mason and N Wookey, editors, *The Rheology of Elastomers*, pages 174–189. Pergamon Press, New York, 1958.

[43] F N Cogswell, J G H Gray, and D A Hubbard. Rheology of a fluid whose behavior approximates to that of a Maxwell body. *Bulletin of the British Society of Rheology*, 15(2):29–31, 1972.

[44] F N Cogswell and P Lamb. The mechanism of melt distortion. *Plastics and Polymers*, 35(120):809–813, 1967.

[45] B D Coleman and W Noll. An approximation theorem for functionals, with applications to continuum mechanics. *Archive for Rational Mechanics and Analysis*, 6:355–370, 1960.

[46] W O Criminale, Jr., J L Ericksen, and G L Filbey, Jr. Steady shear flow of non-Newtonian fluids. *Archive for Rational Mechanics and Analysis*, 1:410–417, 1958.

[47] P K Currie. Calculations on the Doi-Edwards model for concentrated polymer systems. In G Astarita, G Marrucci, and L Nicolais, editors, *Rheology, Volume 1: Principles*, Proceedings of the Eighth International Congress on Rheology, pages 357–362, Naples, Italy, 1980.

[48] J P Decruppe, R Cressely, R Makhloufi, and E Cappelaere. Flow birefringence experiments showing a shear-banding structure in a CTAB solution. *Colloid and Polymer Science*, 273(4):346–351, 1995.

[49] J L den Otter. Mechanisms of melt fracture. *Plastics and Polymers*, 38(135):155–168, 1970.

[50] J L den Otter. Some investigations of melt fracture. *Rheologica Acta*, 10(2):200–207, 1971.

[51] M Doi and S F Edwards. Dynamics of concentrated polymer systems. 1. Brownian motion in equilibrium state. *Journal of the Chemical Society, Faraday Transactions II*, 74(P10):1789–1801, 1978.

[52] M Doi and S F Edwards. Dynamics of concentrated polymer systems. 2. Molecular-motion under flow. *Journal of the Chemical Society, Faraday Transactions II*, 74(P10):1802–1817, 1978.

[53] M Doi and S F Edwards. Dynamics of concentrated polymer systems. 3. Constitutive equation. *Journal of the Chemical Society, Faraday Transactions II*, 74(P10):1818–1832, 1978.

[54] M Doi and S F Edwards. Dynamics of concentrated polymer systems. 4. Rheological properties. *Journal of the Chemical Society, Faraday Transactions II*, 75(P1):38–54, 1979.

[55] G J Donnelly and C B Weinberger. Stability of isothermal fiber spinning of a Newtonian fluid. *Industrial and Engineering Chemistry. Fundamentals*, 14(4):334–337, 1975.

[56] I M Dris and E S G Shaqfeh. On purely elastic instabilities in eccentric cylinder flows. *Journal of Non-Newtonian Fluid Mechanics*, 56(3):349–360, 1995.

[57] J Dunwoody and D D Joseph. Systematic linearisation for stability of shear flows of viscoelastic fluids. *Archive for Rational Mechanics and Analysis*, 86(1):65–84, 1984.

[58] N El Kissi and J M Piau. The different capillary-flow régimes of entangled polydimethylsiloxane polymers – macroscopic slip at the wall, hysteresis and cork flow. *Journal of Non-Newtonian Fluid Mechanics*, 37(1):55–94, 1990.

[59] N El Kissi and J M Piau. Adhesion of linear low-density polyethylene for flow regimes with sharkskin. *Journal of Rheology*, 38(5):1447–1463, 1994.

[60] N El Kissi, J M Piau, and F Toussaint. Sharkskin and cracking of polymer melt extrudates. *Journal of Non-Newtonian Fluid Mechanics*, 68(2–3):271–290, 1997.

[61] P Español, X F Yuan, and R C Ball. Shear banding flow in the Johnson-Segalman fluid. *Journal of Non-Newtonian Fluid Mechanics*, 65(1):93–109, 1996.

[62] R E Evans and K Walters. Flow characteristics associated with abrupt changes in geometry in the case of highly elastic liquids. *Journal of Non-Newtonian Fluid Mechanics*, 20:11–29, 1986.

[63] R E Evans and K Walters. Further remarks on the lip-vortex mechanism of vortex enhancement in planar-contraction flows. *Journal of Non-Newtonian Fluid Mechanics*, 32(1):95–105, 1989.

[64] J D Ferry. *Viscoelastic properties of polymers*. John Wiley & Sons, Inc., second edition, 1970.

[65] R J Fisher and M M Denn. Draw resonance in melt spinning. *Applied Polymer Symposium*, 27:103–109, 1975.

[66] G C Georgiou and M J Crochet. Time-dependent compressible extrudate swell problem with slip at the wall. *Journal of Rheology*, 38(6):1745–1755, 1994.

[67] R Ghisellini. Elastic free-energy of an Upper-Convected Maxwell fluid undergoing a fully-developed planar Poiseuille flow – a variational result. *Journal of Non-Newtonian Fluid Mechanics*, 46(2–3):229–241, 1993.

[68] H Giesekus. Die Elastizität von Flüssigkeiten. *Rheologica Acta*, 5(1):29–35, 1966.

[69] H Giesekus. On the stability of flow of viscoelastic fluids. *Rheologica Acta*, 5(3):239–252, 1966.

[70] H Giesekus. Nonlinear effects in the flow of viscoelastic fluids in slits and holes. *Rheologica Acta*, 7(2):127–138, 1968.

[71] V A Gorodtsov and A I Leonov. On a linear instability of a plane parallel Couette flow of viscoelastic fluid. *Journal of Applied Mathematics and Mechanics*, 31:310, 1967.

[72] A Groisman and V Steinberg. Solitary vortex pairs in viscoelastic Couette flow. *Physical Review Letters*, 78(8):1460–1463, 1997.

[73] A S Gupta. Stability of a visco-elastic liquid film flowing down an inclined plane. *Journal of Fluid Mechanics*, 28(1):17–28, 1967.

[74] C D Han and J Y Park. Studies on blown film extrusion. 3. Bubble instability. *Journal of Applied Polymer Science*, 19:3291–3297, 1975.

[75] O G Harlen, E J Hinch, and J M Rallison. Birefringent pipes – the steady flow of a dilute polymer-solution near a stagnation point. *Journal of Non-Newtonian Fluid Mechanics*, 44:229–265, 1992.

[76] O J Harris and J M Rallison. Instabilities of stagnation point flow of a dilute polymer solution. *Journal of Non-Newtonian Fluid Mechanics*, 55(1):59–90, 1994.

[77] S G Hatzikiriakos. The onset of wall slip and sharkskin melt fracture in capillary flow. *Polymer Engineering and Science*, 34(19):1441–1449, 1994.

[78] S G Hatzikiriakos and J M Dealy. Wall slip of molten high-density polyethylene. 1. Sliding plate rheometer studies. *Journal of Rheology*, 35(4):497–523, 1991.

[79] E J Hinch, O J Harris, and J M Rallison. The instability mechanism for two elastic liquids being coextruded. *Journal of Non-Newtonian Fluid Mechanics*, 43(2–3):311–324, 1992.

[80] T C Ho and M M Denn. Stability of plane Poiseuille flow of a highly elastic liquid. *Journal of Non-Newtonian Fluid Mechanics*, 3(2):179–195, 1977/78.

[81] A P Hooper. Long-wave instability at the interface between two viscous fluids – thin-layer effects. *Physics of Fluids*, 28(6):1613–1618, 1985.

[82] D Y Hsieh. Mechanism for instability of fluid-flow down an inclined plane. *Physics of Fluids A - Fluid Dynamics*, 2(7):1145–1148, 1990.

[83] M A Hulsen and J P P M van der Zanden. Numerical simulation of contraction flows using a multimode Giesekus model. *Journal of Non-Newtonian Fluid Mechanics*, 38(2–3):183–221, 1991.

[84] T W Huseby. Hypothesis on a certain flow instability in polymer melts. *Transactions of the Society of Rheology*, 10(1):181–190, 1966.

[85] J F Hutton. Fracture and secondary flow of elastic liquids. *Rheologica Acta*, 8(1):54–59, 1969.

[86] H Ishihara and S Kase. Studies on melt spinning. 6. Simulation of draw resonance using Newtonian and power-law viscosities. *Journal of Applied Polymer Science*, 20:169–191, 1976.

[87] K P Jackson, K Walters, and R W Williams. Rheometrical study of Boger fluids. *Journal of Non-Newtonian Fluid Mechanics*, 14:173–188, 1984.

[88] C C Ji, J C Yang, and W S Lee. Stability of Newtonian-PTT coextrusion fiber spinning. *Polymer Engineering and Science*, 36(22):2685–2693, 1996.

[89] M W Johnson, Jr. and D Segalman. Model for viscoelastic fluid behavior which allows non-affine deformation. *Journal of Non-Newtonian Fluid Mechanics*, 2(3):225–270, 1977.

[90] Y L Joo and E S G Shaqfeh. Viscoelastic Poiseuille flow through a curved channel – a new elastic instability. *Physics of Fluids A – Fluid Dynamics*, 3(9):2043–2046, 1991.

[91] Y L Joo and E S G Shaqfeh. The effects of inertia on the viscoelastic Dean and Taylor-Couette flow instabilities with application to coating flows. *Physics of Fluids A – Fluid Dynamics*, 4(11):2415–2431, 1992.

[92] Y L Joo and E S G Shaqfeh. A purely elastic instability in Dean and Taylor-Dean flow. *Physics of Fluids A – Fluid Dynamics*, 4(3):524–543, 1992.

[93] Y L Joo and E S G Shaqfeh. Observations of purely elastic instabilities in the Taylor-Dean flow of a Boger fluid. *Journal of Fluid Mechanics*, 262:27–73, 1994.

[94] D D Joseph. Steep wave fronts on extrudates of polymer melts and solutions: Lubrication layers and boundary lubrication. *Journal of Non-Newtonian Fluid Mechanics*, 70(3):187–203, 1997.

[95] F Kang and K P Chen. Nonlinear elastic instability of gravity-driven flow of a thin viscoelastic film down an inclined plane. *Journal of Non-Newtonian Fluid Mechanics*, 57(2–3):243–252, 1995.

[96] S Kase, T Matsuo, and Y Yoshimoto. Theoretical analysis of melt spinning. Part 2. Surging phenomena in extrusion casting of plastic films. *Seni Kikai Gakkai Shi (Japanese Journal of Textile Machinery)*, 19(3):62, 1966.

[97] A Kaye. Non-Newtonian flow in incompressible fluids – Part 1: A general rheological equation of state. Note 134, College of Aeronautics, Cranfield, UK, 1962.

[98] T A Kazachenko. Instability of the interface between two highly elastic liquids in a vertical cylindrical channel. *Zhurnal Fizicheskoi Khimii*, 69(10):1910–1915, 1995.

[99] M Keentok, A G Georgescu, A A Sherwood, and R I Tanner. The measurement of the second normal stress difference for some polymer solutions. *Journal of Non-Newtonian Fluid Mechanics*, 6(3–4):303–324, 1980.

[100] B Khomami. Interfacial stability and deformation of two stratified power law fluids in plane Poiseuille flow. 1. Stability analysis. *Journal of Non-Newtonian Fluid Mechanics*, 36:289–303, 1990.

[101] B Khomami. Interfacial stability and deformation of two stratified power law fluids in plane Poiseuille flow. 2. Interface deformation. *Journal of Non-Newtonian Fluid Mechanics*, 37(1):19–36, 1990.

[102] B Khomami and L D Moreno. Stability of viscoelastic flow around periodic arrays of cylinders. *Rheologica Acta*, 36(4):367–383, 1997.

[103] B Khomami and M M Ranjbaran. Experimental studies of interfacial instabilities in multilayer pressure-driven flow of polymeric melts. *Rheologica Acta*, 36(4):345–366, 1997.

[104] K W Koelling and R K Prud'homme. Instabilities in multi-hole converging flow of viscoelastic fluids. *Rheologica Acta*, 30(6):511–522, 1991.

[105] J W H Kolnaar and A Keller. A temperature window of reduced flow resistance in polyethylene with implications for melt flow rheology. 3. Implications for flow instabilities and extrudate distortion. *Polymer*, 38(8):1817–1833, 1997.

[106] R J Koopmans and J Molenaar. The "sharkskin effect" in polymer extrusion. *Polymer Engineering and Science*, 38(1):101–107, 1998.

[107] W-M Kulicke, H-E Jeberien, H Kiss, and R S Porter. Visual observation of flow irregularities in polymer solutions at theta-conditions. *Rheologica Acta*, 18:711–716, 1979.

[108] W-M Kulicke and R S Porter. Irregularities in steady flow for non-Newtonian fluids between cone and plate. *Journal of Applied Polymer Science*, 23(4):953–966, 1979.

[109] S J Kurtz. Die geometry solutions to sharkskin melt fracture. In B Mena, A Garcia-Rejon, and C Rangel-Nafaile, editors, *Advances in Rheology*, volume 3, *Polymers*, pages 399–407. Universidad Nacional Autónoma de México, Mexico City, 1984.

[110] W Lai. Stability of an elastico-viscous liquid film flowing down an inclined plane. *Physics of Fluids*, 10(4):844–847, 1967.

[111] P Lamb. Analysis of fabrication processes. In *Advances in Polymer Science and Technology*, number 26 in Society of Chemical Industry monograph series, pages 296–312. Society of Chemical Industry, London, England, 1967.

[112] R G Larson. *Constitutive equations for polymer melts and solutions*. Butterworths, Boston, Massachusetts, 1988.

[113] R G Larson. Instabilities in viscoelastic flows. *Rheologica Acta*, 31(3):213–263, 1992.

[114] R G Larson, S J Muller, and E S G Shaqfeh. The effect of fluid rheology on the elastic Taylor-Couette instability. *Journal of Non-Newtonian Fluid Mechanics*, 51(2):195–225, 1994.

[115] R G Larson, E S G Shaqfeh, and S J Muller. A purely elastic instability in Taylor-Couette flow. *Journal of Fluid Mechanics*, 218:573–600, 1990.

[116] H M Laun. Description of the nonlinear shear behavior of low density polyethylene melt by means of an experimentally determined strain dependent memory function. *Rheologica Acta*, 17(1):1–15, 1978.

[117] P Laure, H Le Meur, Y Demay, J C Saut, and S Scotto. Linear stability of multilayer plane Poiseuille flows of Oldroyd-B fluids. *Journal of Non-Newtonian Fluid Mechanics*, 71(1–2):1–23, 1997.

[118] H Le Meur. Non-uniqueness and linear stability of the one-dimensional flow of multiple viscoelastic fluids. *RAIRO – Mathematical Modelling and Numerical Analysis – Modelisation Mathématique et Analyse Numérique*, 31(2):185–211, 1997.

[119] B Lee and J L White. An experimental study of rheological properties of polymer melts in laminar shear flow and of interface deformation and its mechanisms in two-phase stratified flow. *Transactions of the Society of Rheology*, 18(3):467–492, 1974.

[120] C S Lee, B C Tripp, and J J Magda. Does N_1 or N_2 control the onset of edge fracture? *Rheologica Acta*, 31(3):306–308, 1992.

[121] K C Lee and B A Finlayson. Stability of plane Poiseuille and Couette flow of a Maxwell fluid. *Journal of Non-Newtonian Fluid Mechanics*, 21(1):65–78, 1986.

[122] W S Lee. Linear stability of a concentric two-phase fiber spinning. *Journal of the Chinese Institute of Chemical Engineers*, 25(3):173–182, 1994.

[123] W S Lee and C W Park. An experimental study of a bicomponent fiber spinning. *International Polymer Processing*, 9(4):359–364, 1994.

[124] C-H Li. Stability of two superposed elasticoviscous liquids in plane Couette flow. *Physics of Fluids*, 12(3):531–538, 1969.

[125] F J Lim and W R Schowalter. Pseudo-spectral analysis of the stability of pressure-driven flow of a Giesekus fluid between parallel planes. *Journal of Non-Newtonian Fluid Mechanics*, 26(1):135–142, 1987.

[126] F J Lockett. On Squire's theorem for viscoelastic fluids. *International Journal of Engineering Science*, 7:337–349, 1969.

[127] J M Lupton and R W Regester. Melt flow of polyethylene at high rates. *Polymer Engineering and Science*, 5:235–245, 1965.

[128] M J MacDonald and S J Muller. Shear rheology of polymer solutions near the critical condition for elastic instability. *Rheologica Acta*, 36(2):97–109, 1997.

[129] J J Magda and S G Baek. Concentrated entangled and semidilute entangled polystyrene solutions and the second normal stress difference. *Polymer*, 35(6):1187–1194, 1994.

[130] J J Magda and R G Larson. A transition occurring in ideal elastic liquids during shear flow. *Journal of Non-Newtonian Fluid Mechanics*, 30(1):1–19, 1988.

[131] J J Magda, J Lou, S G Baek, and K L de Vries. Second normal stress difference of a Boger fluid. *Polymer*, 32(11):2000–2009, 1991.

[132] R Makhloufi, J P Decruppe, A Aitali, and R Cressely. Rheo-optical study of worm-like micelles undergoing a shear-banding flow. *Europhysics Letters*, 32(3):253–258, 1995.

[133] M A Matovich and J R A Pearson. Spinning a molten threadline: steady-state isothermal viscous flows. *Industrial and Engineering Chemistry. Fundamentals*, 8(3):512–520, 1969.

[134] H Mavridis and R N Shroff. Multilayer extrusion – experiments and computer-simulation. *Polymer Engineering and Science*, 34(7):559–569, 1994.

[135] G H McKinley, R C Armstrong, and R A Brown. The wake instability in viscoelastic flow past confined circular cylinders. *Philosophical Transactions of the Royal Society of London Series A – Physical Sciences and Engineering*, 344(1671):265–304, 1993.

[136] G H McKinley, J A Byars, R A Brown, and R C Armstrong. Observations on the elastic instability in cone-and-plate and parallel-plate flows of a polyisobutylene Boger fluid. *Journal of Non-Newtonian Fluid Mechanics*, 40(2):201–229, 1991.

[137] G H McKinley, A Öztekin, J A Byars, and R A Brown. Self-similar spiral instabilities in elastic flows between a cone and a plate. *Journal of Fluid Mechanics*, 285:123–164, 1995.

[138] G H McKinley, P Pakdel, and A Öztekin. Rheological and geometric scaling of purely elastic flow instabilities. *Journal of Non-Newtonian Fluid Mechanics*, 67:19–47, 1996.

[139] G H McKinley, W P Raiford, R A Brown, and R C Armstrong. Nonlinear dynamics of viscoelastic flow in axisymmetrical abrupt contractions. *Journal of Fluid Mechanics*, 223:411–456, 1991.

[140] T C B McLeish and R C Ball. A molecular approach to the spurt effect in polymer melt flow. *Journal of Polymer Science part B – Polymer Physics*, 24(8):1735–1745, 1986.

[141] J C Miller. Swelling behaviour in extrusion. *Society of Petroleum Engineers Transactions*, 3(2):134–137, 1963.

[142] W Minoshima and J L White. Instability phenomena in tubular film and melt spinning of rheologically characterized high-density, low-density and linear low-density polyethylenes. *Journal of Non-Newtonian Fluid Mechanics*, 19(3):275–302, 1986.

[143] H K Moffatt. Viscous and resistive eddies near a sharp corner. *Journal of Fluid Mechanics*, 18:1–18, 1964.

[144] R H Moynihan, D G Baird, and R Ramanathan. Additional observations on the surface melt-fracture behavior of linear low-density polyethylene. *Journal of Non-Newtonian Fluid Mechanics*, 36:255–263, 1990.

[145] S J Muller, R G Larson, and E S G Shaqfeh. A purely elastic transition in Taylor-Couette flow. *Rheologica Acta*, 28(6):499–503, 1989.

[146] H K Nason. A high temperature, high pressure rheometer for plastics. *Journal of Applied Physics*, 16:338–343, 1945.

[147] J A Odell, A J Müller, and A Keller. Non-Newtonian behaviour of hydrolysed polyacrylamide in strong elongational flows – a transient network approach. *Polymer*, 29(7):1179–1190, 1988.

[148] D O Olagunju. Elastic instabilities in cone-and-plate flow – small-gap theory. *Zeitschrift für Angewandte Mathematik und Physik*, 46(6):946–959, 1995.

[149] J G Oldroyd. On the formulation of rheological equations of state. *Proceedings of the Royal Society*, A200:523–541, 1950.

[150] Y Oyanagi. A study of irregular flow behaviour of high density polyethylene. *Applied Polymer Symposium*, 20:123–136, 1973.

[151] A Öztekin, B Alakus, and G H McKinley. Stability of planar stagnation flow of a highly viscoelastic fluid. *Journal of Non-Newtonian Fluid Mechanics*, 72(1):1–29, 1997.

[152] A Öztekin and R A Brown. Instability of a viscoelastic fluid between rotating parallel disks – analysis for the Oldroyd-B fluid. *Journal of Fluid Mechanics*, 255:473–502, 1993.

[153] A Öztekin, R A Brown, and G H McKinley. Quantitative prediction of the viscoelastic instability in cone-and-plate flow of a Boger fluid using a multimode Giesekus model. *Journal of Non-Newtonian Fluid Mechanics*, 54:351–377, 1994.

[154] P Pakdel and G H McKinley. Elastic instability and curved streamlines. *Physical Review Letters*, 77(12):2459–2462, 1996.

[155] J R A Pearson and M A Matovich. Spinning a molten threadline: stability. *Industrial and Engineering Chemistry. Fundamentals*, 8(4):605–609, 1969.

[156] J R A Pearson and C J S Petrie. On melt flow instability of extruded polymers. In R E Wetton and R W Whorlow, editors, *Polymer Systems: Deformation and Flow*, pages 163–187. Macmillan, London, England, 1968.

[157] A Peterlin. Einfluß der endlichen Moleküllänge auf die Gradientenabhängigkeit des Staudinger-Index. *Makromolekulare Chimie*, 44(6):338–346, 1961.

[158] C J S Petrie and M M Denn. Instabilities in polymer processing. *American Institute of Chemical Engineering Journal*, 22(2):209–236, 1976.

[159] N Phan-Thien. Coaxial disk flow of an Oldroyd-B fluid – exact solution and stability. *Journal of Non-Newtonian Fluid Mechanics*, 13(3):325–340, 1983.

[160] N Phan-Thien and R I Tanner. A new constitutive equation derived from network theory. *Journal of Non-Newtonian Fluid Mechanics*, 2:353–365, 1977.

[161] J M Piau, N El Kissi, and A Mezghani. Slip-flow of polybutadiene through fluorinated dies. *Journal of Non-Newtonian Fluid Mechanics*, 59(1):11–30, 1995.

[162] J M Piau, N El Kissi, F Toussaint, and A Mezghani. Distortions of polymer melt extrudates and their elimination using slippery surfaces. *Rheologica Acta*, 34(1):40–57, 1995.

[163] J M Piau, N El Kissi, and B Tremblay. Influence of upstream instabilities and wall slip on melt fracture and sharkskin phenomena during silicones extrusion through orifice dies. *Journal of Non-Newtonian Fluid Mechanics*, 34(2):145–180, 1990.

[164] A Pinarbasi and A Liakopoulos. The effect of variable viscosity on the interfacial stability of two-layer Poiseuille flow. *Physics of Fluids*, 7(6):1318–1324, 1995.

[165] A Pinarbasi and A Liakopoulos. Stability of two-layer Poiseuille flow of Carreau-Yasuda and Bingham-like fluids. *Journal of Non-Newtonian Fluid Mechanics*, 57(2–3):227–241, 1995.

[166] G Pomar, S J Muller, and M M Denn. Extrudate distortions in linear low-density polyethylene solutions and melt. *Journal of Non-Newtonian Fluid Mechanics*, 54:143–151, 1994.

[167] L Preziosi, K P Chen, and D D Joseph. Lubricated pipelining – stability of core-annular flow. *Journal of Fluid Mechanics*, 201:323–356, 1989.

[168] L Preziosi and S Rionero. Energy stability of steady shear flows of a viscoelastic fluid. *International Journal of Engineering Science*, 27(10):1167–1181, 1989.

[169] A V Ramamurthy. Wall slip in viscous fluids and influence of materials of construction. *Journal of Rheology*, 30(2):337–357, 1986.

[170] M Reiner. A mathematical theory of dilatancy. *American Journal of Mathematics*, 67(3):350–362, 1945.

[171] M Renardy and Y Y Renardy. Linear stability of plane Couette flow of an Upper-Convected Maxwell fluid. *Journal of Non-Newtonian Fluid Mechanics*, 22(1):23–33, 1986.

[172] Y Y Renardy. Instability at the interface between two shearing fluids in a channel. *Physics of Fluids*, 28(12):3441–3443, 1985.

[173] Y Y Renardy. The thin-layer effect and interfacial stability in a two-layer Couette-flow with similar liquids. *Physics of Fluids*, 30(6):1627–1637, 1987.

[174] Y Y Renardy. Stability of the interface in two-layer Couette flow of Upper-Convected Maxwell liquids. *Journal of Non-Newtonian Fluid Mechanics*, 28(1):99–115, 1988.

[175] Y Y Renardy. Spurt and instability in a two-layer Johnson-Segalman liquid. *Theoretical and Computational Fluid Dynamics*, 7(6):463–475, 1995.

[176] Y Y Renardy. Weakly nonlinear behaviour of periodic disturbances in two-layer plane channel flow of Upper-Convected Maxwell liquids. *Journal of Non-Newtonian Fluid Mechanics*, 56(2):101–126, 1995.

[177] R S Rivlin. The hydrodynamics of non-Newtonian fluids. *Proceedings of the Royal Society*, A193:260–281, 1949.

[178] R S Rivlin and J L Ericksen. Stress-deformation relations for isotropic materials. *Journal of Rational Mechanics and Analysis*, 4:323–425, 1955.

[179] W J Sang. Interfacial instabilities in plane Poiseuille flow of two stratified viscoelastic fluids with heat-transfer. 1. Evolution equation and stability analysis. *Journal of Fluid Mechanics*, 299:241–265, 1995.

[180] G Schleiniger and R J Weinacht. Steady Poiseuille flows for a Giesekus fluid. *Journal of Non-Newtonian Fluid Mechanics*, 40(1):79–102, 1991.

[181] W R Schowalter. The behaviour of complex fluids at solid boundaries. *Journal of Non-Newtonian Fluid Mechanics*, 29(1–3):25–36, 1988.

[182] E S G Shaqfeh. Purely elastic instabilities in viscometric flows. *Annual Review of Fluid Mechanics*, 28:129–186, 1996.

[183] E S G Shaqfeh, R G Larson, and G H Fredrickson. The stability of gravity-driven viscoelastic film-flow at low to moderate Reynolds-number. *Journal of Non-Newtonian Fluid Mechanics*, 31(1):87–113, 1989.

[184] E S G Shaqfeh, S J Muller, and R G Larson. The effects of gap width and dilute-solution properties on the viscoelastic Taylor-Couette instability. *Journal of Fluid Mechanics*, 235:285–317, 1992.

[185] J D Shore, D Ronis, L Piche, and M Grant. Sharkskin texturing instabilities in the flow of polymer melts. *Physica A*, 239(1–3):350–357, 1997.

[186] J D Shore, D Ronis, L Piche, and M Grant. Theory of melt fracture instabilities in the capillary flow of polymer melts. *Physical Review E*, 55(3B):2976–2992, 1997.

[187] N Sombatsompop and A K Wood. Flow analysis of natural rubber in a capillary rheometer. 2. Flow patterns and entrance velocity profiles in the die. *Polymer Engineering and Science*, 37(2):281–290, 1997.

[188] N A Spenley, M E Cates, and T C B McLeish. Nonlinear rheology of wormlike micelles. *Physical Review Letters*, 71(6):939–942, 1993.

[189] H B Squire. On the stability for three-dimensional disturbances of viscous fluid flow between parallel walls. *Proceedings of the Royal Society A*, 142:621–628, 1933.

[190] C W Stewart. Wall slip in the extrusion of linear polyolefins. *Journal of Rheology*, 37(3):499–513, 1993.

[191] C W Stewart, R S McMinn, and K M Stika. A model for predicting slip velocity during extrusion with fluoropolymer processing additives. *Journal of Reinforced Plastics and Composites*, 12(6):633–641, 1993.

[192] Y-Y Su and B Khomami. Stability of multilayer power-law and second-order fluids in plane Poiseuille flow. *Chemical Engineering Communications*, 109:209–223, 1991.

[193] Y-Y Su and B Khomami. Interfacial stability of multilayer viscoelastic fluids in slit and converging channel die geometries. *Journal of Rheology*, 36(2):357–387, 1992.

[194] Y-Y Su and B Khomami. Purely elastic interfacial instabilities in superposed flow of polymeric fluids. *Rheologica Acta*, 31:413–420, 1992.

[195] T Takaki and D C Bogue. The extensional and failure properties of polymer melts. *Journal of Applied Polymer Science*, 19:419–433, 1975.

[196] K C Tam, C Tiu, and T N Fang. Remarks on the shear-thickening behaviour of dilute polymer solutions. *Polymer – Plastics Technology and Engineering*, 30(2–3):145–162, 1991.

[197] R I Tanner. *Engineering Rheology*. Oxford Press, New York, 1985.

[198] R I Tanner and M Keentok. Shear fracture in cone plate rheometry. *Journal of Rheology*, 27(1):47–57, 1983.

[199] G I Taylor. Stability of a viscous liquid contained between rotating cylinders. *Philosophical Transactions of the Royal Society of London Series A*, 223:289–343, 1923.

[200] V Tirtaatmadja and T Sridhar. A filament stretching device for measurement of extensional viscosity. *Journal of Rheology*, 37(6):1081–1102, 1993.

[201] G Tlapa and B Bernstein. Stability of a relaxation-type viscoelastic fluid with slight elasticity. *Physics of Fluids*, 11(1):565–568, 1976.

[202] J P Tordella. An instability in the flow of molten polymers. *Rheologica Acta*, 1(2–3):216–221, 1958.

[203] B Tremblay. Sharkskin defects of polymer melts – the rôle of cohesion and adhesion. *Journal of Rheology*, 35(6):985–998, 1991.

[204] C Tzoganakis, B C Price, and S G Hatzikiriakos. Fractal analysis of the sharkskin phenomenon in polymer melt extrusion. *Journal of Rheology*, 37(2):355–366, 1993.

[205] Milton Van Dyke. *Perturbation Methods in Fluid Mechanics*. Academic Press, New York and London, 1964.

[206] C Venet and B Vergnes. Experimental characterization of sharkskin in polyethylenes. *Journal of Rheology*, 41(4):873–892, 1997.

[207] G V Vinogradov. Viscoelasticity and fracture phenomenon in uniaxial extension of high-molecular linear polymers. *Rheologica Acta*, 14(10):942–954, 1975.

[208] G V Vinogradov and L I Ivanova. Wall slippage and elastic turbulence of polymers in the rubbery state. *Rheologica Acta*, 7(3):243–254, 1968.

[209] G V Vinogradov, A Y Malkin, Y G Yanovskii, E K Borisenkova, B V Yarlykov, and G V Berezhnaya. Viscoelastic properties and flow of narrow distribution polybutadienes and polyisoprenes. *Journal of Polymer Science*, A2(10):1061–1084, 1972.

[210] S Q Wang, P A Drda, and Y W Inn. Exploring molecular origins of sharkskin, partial slip, and slope change in flow curves of linear low-density polyethylene. *Journal of Rheology*, 40(5):875–898, 1996.

[211] N D Waters. The stability of two stratified power-law fluids in Couette flow. *Journal of Non-Newtonian Fluid Mechanics*, 12(1):85–94, 1983.

[212] N D Waters and A M Keeley. The stability of two stratified non-Newtonian liquids in Couette-flow. *Journal of Non-Newtonian Fluid Mechanics*, 24(2):161–181, 1987.

[213] C B Weinberger, G F Cruz-Saenz, and G J Donnelly. Onset of draw resonance during isothermal melt spinning: A comparison between measurements and predictions. *American Institute of Chemical Engineering Journal*, 22(3):441–448, 1976.

[214] J L White and A B Metzner. Development of constitutive equations for polymeric melts and solutions. *Journal of Applied Polymer Science*, 7:1867–1889, 1963.

[215] G M Wilson and B Khomami. An experimental investigation of interfacial instabilities in multilayer flow of viscoelastic fluids. 1. Incompatible polymer systems. *Journal of Non-Newtonian Fluid Mechanics*, 45(3):355–384, 1992.

[216] G M Wilson and B Khomami. An experimental investigation of interfacial instabilities in multilayer flow of viscoelastic fluids. 2. Elastic and nonlinear effects in incompatible polymer systems. *Journal of Rheology*, 37(2):315–339, 1993.

[217] G M Wilson and B Khomami. An experimental investigation of interfacial instabilities in multilayer flow of viscoelastic fluids. 3. Compatible polymer systems. *Journal of Rheology*, 37(2):341–354, 1993.

[218] H J Wilson and J M Rallison. Short wave instability of co-extruded elastic liquids with matched viscosities. *Journal of Non-Newtonian Fluid Mechanics*, 72(2–3):237–251, 1997.

[219] W T Wong and C C Jeng. The stability of two concentric non-Newtonian fluids in circular pipe-flow. *Journal of Non-Newtonian Fluid Mechanics*, 22(3):359–380, 1987.

[220] C-S Yih. Stability of liquid flow down an inclined plane. *Physics of Fluids*, 6(3):321–334, 1963.

[221] C-S Yih. Instability due to viscosity stratification. *Journal of Fluid Mechanics*, 27(2):337–352, 1967.

[222] J Y Yoo and Y Na. A numerical study on the planar contraction flow of a viscoelastic fluid using the SIMPLER algorithm. *Journal of Non-Newtonian Fluid Mechanics*, 39(1):89–106, 1991.

[223] H S Yu and E M Sparrow. Experiments on two-component stratified flow in a horizontal duct. *Journal of Heat Transfer*, 91(1):51–58, 1969.

[224] G Zeichner. Spinnability of viscoelastic fluids. Master's thesis, University of Delaware, Newark, 1973.

[225] A Ziabicki and R Takserman-Krozer. Formation and breakage of liquid threads. I. Mechanism. *Roczniki Chemii*, 37(11):1503–1509, 1963.

[226] A Ziabicki and R Takserman-Krozer. Formation and breakage of liquid threads. II. Cohesive break of a steady liquid jet. *Roczniki Chemii*, 37(11):1511–1518, 1963.

[227] A Ziabicki and R Takserman-Krozer. Formation and breakage of liquid threads. III. Capillary break-up of a steady viscous jet. *Roczniki Chemii*, 37(12):1607–1616, 1963.

[228] A Ziabicki and R Takserman-Krozer. Formation and breakage of liquid threads. IV. Effect of rheological behaviour on the length of liquid threads. *Roczniki Chemii*, 38(3):465–482, 1964.

[229] A Ziabicki and R Takserman-Krozer. Formation and breakage of liquid threads. V. Range of occurrence of the individual break processes. General conclusions. *Roczniki Chemii*, 38(4):653–661, 1964.

[230] A Ziabicki and R Takserman-Krozer. Formation and breakage of liquid threads. VI. Following the break process with high-speed photography. *Roczniki Chemii*, 38(7–8):1221–1234, 1964.

[231] A Ziabicki and R Takserman-Krozer. Mechanism and breakage of liquid threads: to the problem of "spinnability" of liquids. *Kolloid-Zeitschrift und Zeitschrift für Polymere*, 198(1–2):60–65, 1964.

[232] A Ziabicki and R Takserman-Krozer. Effect of rheological factors on the length of liquid threads. *Kolloid-Zeitschrift und Zeitschrift für Polymere*, 199(1):9–13, 1965.

Index